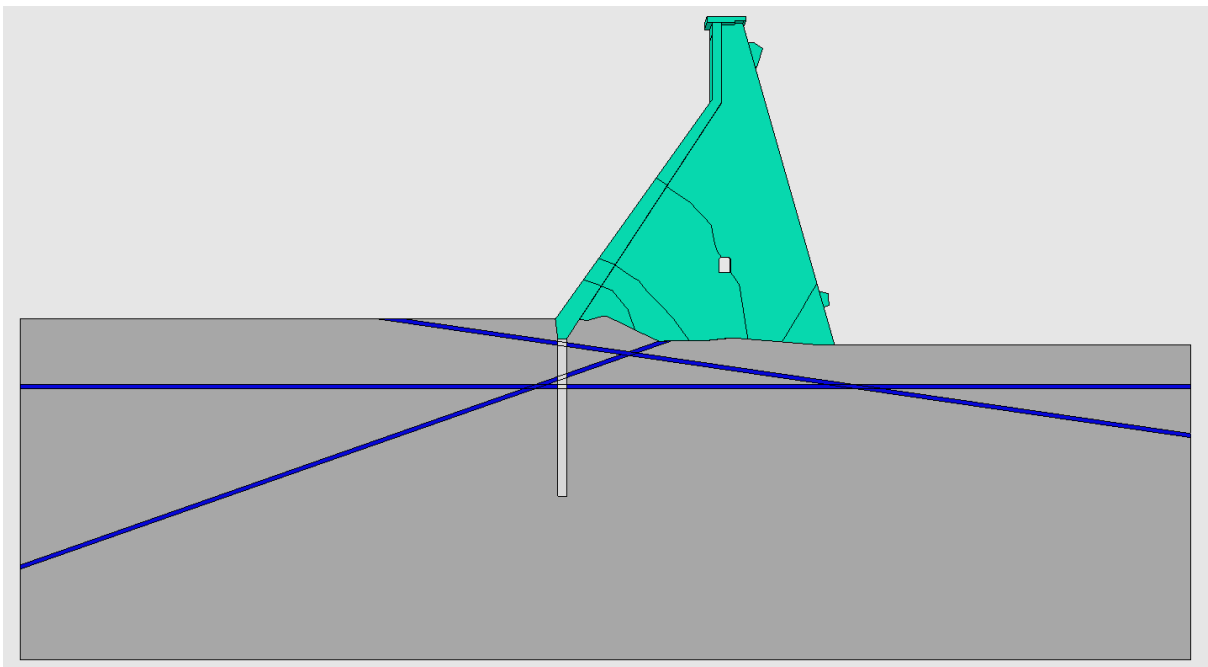


Degree project in Concrete Structures

SECOND CYCLE, 30 CREDITS

# Numerical simulations of pore pressure on concrete buttress dams

MOHAMMED ABDI  
DIMITIRIOS NTZIMANIS







# Numerical simulations of pore pressure on concrete buttress dams

Mohammed Abdi  
Dimitrios Ntzimanis

June 2022  
TRITA-ABE-MBT-22404  
ISBN: 978-91-8040-306-1



# Abstract

Uplift pressure is one of the most dominant forces on a dam structure. Difference in headwater and tailwater creates a hydraulic gradient resulting an upward oriented pressure called uplift pressure, which reduces the dam safety against sliding. However, there are great uncertainties determining the actual magnitude and distribution of the uplift pressure. Therefore, finite element methods were used in order to study the pore pressure in greater extent to increase the knowledge about the field measurements.

In this MSc report, the pore pressure in the rock foundation at monolith M42 in Storfinnforsen hydropower dam has been investigated. The aim of the project is to study the realistic pore pressure distributions and its magnitude underneath the dam. The aim is also to compare and find correlation between the numerical results and field measurements as well as the analytical results based on guidelines for dam safety.

Pore pressure in rock foundation can be influenced by many factors such as, the presence of drainage, grout curtain and rock fractures. Therefore, several numerical models have been developed containing different combinations based on these factors. Numerical results were then compared to both field measurements and analytical results. Furthermore, the uplift pressure from the best calibrated model and models representing critical states of the dam are used to calculate stability safety factor against sliding.

The finite element program Abaqus is used to perform all the numerical pore pressure analyses. Field measurements is obtained from two pore pressure sensors installed underneath the dam and analytical results are calculated based on guidelines for dam safety.

Based on the results from the case study, comparison of the numerical pore pressure with the field measurements showed that the drains have the largest impact on the pore pressure compared to other parameters. Models without drains have showed significantly larger pore pressure than the field measurements. When drains are in operation, considering empty drains underestimate the pore pressure while water filled drains slightly overestimated the pore pressure.

The influence of grout curtain varies if the effect of drains are included or not. Considering fractured rock foundation, the grout curtain showed large reduction of the pore pressure in the analyses without drains. If drains are in operation, this reduction becomes quite small. Moreover, all the numerical analyses showed that the uplift pressure in the rock fracture are lower than what is defined in the design guideline (RIDAS, 2020).

**Keywords:** Pore pressure analysis, uplift pressure, buttress dams, drainage, grout curtain, rock fractures, dam safety, RIDAS.



# Sammanfattning

Upptrycket är en av de mest dominerande krafterna som verkar på en dammkonstruktion. Skillnaden i vattennivå mellan uppström och nedström skapar en hydraulisk gradient som resulterar i ett uppåtriktat tryck som kallas upptryck, vilket minskar dammsäkerheten mot glidning. Det finns dock stora osäkerheter för att bestämma den faktiska intensiteten, riktningen och placeringen av upplyfttrycket. Därför användes finita elementmetoder för att i större utsträckning studera portrycket och öka kunskapen om de uppmättade portrycket.

I detta examensarbete har portrycket i berggrunden vid monolit M42 i Storfinnforsens vattenkraftsdam undersökts. Syftet med projektet är att studera realistiska portrycksfördelningar och dess storlek. Syftet är också att jämföra och hitta samband mellan de numeriska resultaten och uppmätta värden samt de analytiska resultaten som baseras på riktlinjer för dammsäkerhet.

Portrycket i berggrunden kan påverkas av många faktorer såsom förekomsten av dränering, injekteringsskärm och bergsprickor. Därför har flera numeriska modeller utvecklats som innehåller olika kombinationer utifrån dessa faktorer. Resultat från de numeriska modellerna jämfördes med både fältmätningarna från de installerade portryckssensorerna och de analytiska resultaten. Vidare används upptrycket från den bäst kalibrerade modellen och några andra modeller som representerar kritiska tillstånd i dammen för att utföra säkerhetsfaktorberäkningar. Det finita elementprogrammet Abaqus användes för att utföra alla numeriska portrycksanalyser. Fältmätningar erhålls från två portryckssensorer under dammen och analytiska resultat har beräknats baserade på riktlinjer för dammsäkerhet.

Baserat på resultatet från fallstudien så visade vid en jämförelse av det numeriska portrycket med fältmätningarna att dräneringen har en stor inverkan på portrycket. Modeller utan dränering har visat ha betydligt större portryck än uppmättade värdena. När dränering är i drift, underskattas portrycket ifall dränagerören antas vara tomma medan en viss överskattning fås om de antas vara vattenfyllda.

Inverkan av injekteringsskärmen varierar om effekten av dränage ingår eller inte. Vid analyser som beaktar bergsprickor så bidrog injekteringsskärmen i en stor reduktion av portrycket om modellen saknar dränage. I fall med fungerande dränage så fås en liten effekt av injekteringsskärm. Slutligen, alla numeriska modeller har visat ett lägre portryck än de analytiska resultaten.

**Nyckelord:** Portrycksanalys, upplyftstryck, lammelldammar, dränering, injekteringsskärm, bergsprickor, dammsäkerhet, RIDAS.





# Preface

This MSc report was carried out in collaboration between Sweco AB and the division of concrete structures, department of Civil and Architectural Engineering at the KTH Royal Institute of Technology. The work was supervised by Docent, Richard Malm at KTH together with Agnetha Bergström and Alexandra Ålenius at Sweco.

We would like to express our deepest gratitude to our supervisor at KTH, Docent. Richard Malm for his constant support and supervision during the period of this thesis. We are truly grateful for your guidance and constructive feedback during the course of this project. Without your experience and expertise this project would not be possible.

We would also like to express our gratitude to Alexandra Ålenius for setting the course of the project in the beginning and to Agnetha Bergström for seeing through the project at the end.

Finally, we would like to say big thanks to all the people at Sweco Energy AB for giving us the opportunity to carry out our thesis at their office and helping us with various problems during the course the project.

Stockholm, June 2022

*Mohammed Abdi*

*Dimitrios Ntzimanis*



# Contents

<b>Abstract</b>	<b>iii</b>
<b>Sammanfattning</b>	<b>v</b>
<b>Preface</b>	<b>vii</b>
<b>1 Introduction</b>	<b>1</b>
1.1 Background . . . . .	1
1.2 Aim and scope . . . . .	3
1.3 Limitations . . . . .	3
1.4 Disposition . . . . .	4
<b>2 Uplift pressure on concrete dams</b>	<b>5</b>
2.1 Buttress dam structural system . . . . .	5
2.2 Uplift pressure general theory . . . . .	6
2.2.1 Considerations according to RIDAS guideline . . . . .	10
2.2.2 Considerations according to USACE guideline . . . . .	13
2.3 Effect of grout curtain . . . . .	17
2.4 Influence of the bedrock foundation . . . . .	18
2.4.1 Rock mass . . . . .	18
2.4.2 Intact rock . . . . .	19
2.4.3 Rock Discontinuities . . . . .	19
2.4.4 Wedge support implementation . . . . .	27

2.4.5	Sliding safety factor . . . . .	29
2.4.6	Pore pressure analysis in Abaqus software . . . . .	30
<b>3</b>	<b>Storfinnforsen Monolith</b>	<b>42</b>
3.1	Geometry of the monolith . . . . .	37
3.2	Drainage holes and piezometers . . . . .	38
3.3	Measured pore pressure . . . . .	40
3.4	Rock fractures . . . . .	41
3.5	Sliding failure cases . . . . .	42
3.5.1	Case A: crushed inclined fracture $\phi_{frac} = 8.97^\circ$ . . . . .	42
3.5.2	Case B: horizontal fracture $\phi_{frac} = 180^\circ$ . . . . .	43
3.5.3	Uplift distributions according to the guidelines . . . . .	43
3.6	Influence of deep fractures . . . . .	44
3.7	Influence of the fracture friction angle . . . . .	44
<b>4</b>	<b>Numerical model</b>	<b>45</b>
4.1	Geometry . . . . .	45
4.2	Rock fractures . . . . .	46
4.3	Grout curtain . . . . .	46
4.4	Drainage system . . . . .	46
4.5	Material properties . . . . .	47
4.6	Mesh discretization . . . . .	48
4.7	Initial conditions . . . . .	49
4.8	Boundary conditions . . . . .	49
4.9	Applied loads . . . . .	50
4.10	Analysis procedure . . . . .	51
4.11	Evaluation of the pore pressure at the position of the sensors . . . . .	51
4.12	Investigated models . . . . .	52

4.12.1	Models without drainage system . . . . .	52
4.12.2	Influence of the drains . . . . .	52
4.12.3	Variation of the hydraulic conductivity . . . . .	53
4.12.4	Alternative models for the hydraulic conductivity . . . . .	53
4.12.5	Alternative models for the grout curtain . . . . .	55
<b>5</b>	<b>Pore pressure analyses</b>	<b>57</b>
5.1	Models without drainage . . . . .	57
5.1.1	Model 1 - Homogeneous rock foundation . . . . .	57
5.1.2	Model 2 - Influence of rock fractures . . . . .	58
5.1.3	Model 3 - Influence of grout curtain . . . . .	58
5.1.4	Model 4 - Combination of grout curtain and rock fractures . . . . .	59
5.2	Influence of the drains . . . . .	60
5.2.1	Drainage system fully filled with air . . . . .	60
5.2.2	Drainage fully filled with water . . . . .	62
5.2.3	Additional filling conditions . . . . .	64
5.3	Result summary of the investigated cases . . . . .	65
5.3.1	Comparison of pore pressure results . . . . .	65
5.3.2	Uplift pressure distribution . . . . .	68
5.3.3	Comparison of analytical and numerical results . . . . .	73
5.3.4	Model choice for further research . . . . .	76
5.4	Variation of the hydraulic conductivity . . . . .	77
5.5	Alternative models for the hydraulic conductivity . . . . .	79
5.5.1	Fractures with tapered aperture . . . . .	79
5.5.2	Constant hydraulic conductivity in each fracture . . . . .	81
5.6	Alternative models for the grout curtain . . . . .	84
<b>6</b>	<b>Sliding stability analysis</b>	<b>87</b>

6.1	Wedge passive forces . . . . .	88
6.2	Safety factors . . . . .	89
6.3	Effect of deep fractures . . . . .	92
6.4	Friction angle effect . . . . .	93
<b>7</b>	<b>Discussion</b>	<b>95</b>
7.1	Numerical models . . . . .	95
7.1.1	Influence of drains . . . . .	95
7.1.2	Influence of rock fractures . . . . .	96
7.1.3	Influence of grout curtain . . . . .	96
7.2	Safety factors . . . . .	97
7.3	Deep fractures . . . . .	98
7.4	Friction angle . . . . .	98
<b>8</b>	<b>Conclusions and further research</b>	<b>101</b>
8.1	Conclusions . . . . .	101
8.2	Further research . . . . .	102
	<b>Bibliography</b>	<b>103</b>
<b>A</b>	<b>Contour plots</b>	<b>107</b>
A.1	Models c - Half water filled drains . . . . .	107
A.2	Models d - 2/3 water filled drains . . . . .	109
A.3	Alternative models for the grout curtain . . . . .	111

# Chapter 1

## Introduction

### 1.1 Background

Dams fill an important role in our society. They enable hydroelectric power production, provide protection from both river and marine floods, supply drinking water and for irrigation to grow food and much more. A dam failure could cause extreme floods, which may have a significant effect on both human and animal lives and destroy valuable properties. Therefore, the dam safety must be ensured in order to avoid these extraordinary consequences. Dams should be also monitored and maintained to know at any time how it is performing and to prevent problems with stability and structural integrity that may lead to the collapse of the dam.

The majority of the Swedish dams were constructed between the period 1950-1960 in order to produce hydropower energy and manage the water sources (Svensen, 2016). Some of these dams are now near at the end of their expected life cycle and have ageing related problems such as material deterioration and foundational problems, which could impact of the dam safety assessment. Moreover, new loading conditions caused by the climate change and increased knowledge may also have a considerable effect of the dam safety.

The Swedish power companies' guidelines for dam safety, RIDAS (2020), requires that dams should be designed, constructed, operated, maintained, and monitored through different surveillance and emergency systems. In order to fulfill these requirements, many dam constructions are undergoing re-examination to ensure that the structural stability requirements are not exceeded.

Dam safety is assuring that the structural integrity and the viability of the dam do not pose an unacceptable risk of failure. Risk is defined as the product of consequences and probability of failure. When reassessing structural stability of concrete dams, it is currently assumed that the dam is a rigid body, and the static equilibrium is evaluated by comparing the stabilizing and destabilizing forces acting on the dam (Ruggeri, 2004). Unfortunately, it is not possible to determine the exact magnitude of some of these forces and thus, require approximation of the intensity, direction, and location these forces. As described in (FERC, 1997), the most uncertain loads on a dam are the pore pressure and

uplift pressure, which have a great impact on the dam safety assessments (Spross et al., 2014).

The uplift pressure is one of the most dominant forces subjected on a dam structure. Water level difference between upstream and downstream sides of a dam structure creates a hydraulic gradient resulting an upward oriented pressure called uplift pressure, which acts on the interface between the dam and rock foundation or inside potential fracture planes within the rock foundation or in the dam body. Uplift pressure influences the stability assessment by reducing the stabilizing forces. Nevertheless, there are many uncertainties determining the actual magnitude and distribution of the uplift pressure.

Factors that may affect the distribution of the water flow which further influence the magnitude and distribution of the uplift pressure include the presence and effectiveness of a drainage system and existence of a functional grout curtain as well as parameters related to the rock fracture such as the permeability along the fracture, the fracture orientation, spacing, persistence, interconnection and aperture size (USACE, 1995). Thus, quantifying the uplift pressure is not a simple task. Therefore, many guidelines for dam safety including the Swedish guideline for dam safety (RIDAS), assume that the uplift pressure varies linearly from headwater to tailwater. In the presence of drainage, the guidelines usually reduce the uplift pressure at the position of the drainage holes with a predefined factor.

In recent years, many dams have been equipped with pore pressure sensors as a monitoring system. Even so, the number of pore pressure sensors installed along the base for many dams are rather limited and thus, makes it difficult to capture the real size and distribution of the uplift pressure. Uplift pressure can oscillate alongside the base substantially due to combination of both loads and variation in temperature, especially in the Nordic countries, which makes even more difficult to quantify the uplift pressure (Bernstone et al., 2009).

The energy company Uniper have installed new monitoring system at two of its largest hydropower dams back in 2016. One of these dams are called Storfinnforsen and is located in the northern part of Sweden at Faxälven River. Storfinnforsen is over 1200 m long and 41 m high at its highest point. Uniper have installed 180 piezometer sensors in the dam with the intention of always monitoring the dam's behavior and to also, create warnings and alarm system if the structural integrity and safety of the dam is below the required level.

In the last decade, a number of investigations have been performed on the Storfinnforsen buttress dam regarding the real conditions and material properties of the dam. For instance, an in-situ investigation of the material properties of the dam and rock foundation, a BIPS loggins investigation that showed the existence of rock fractures in the foundation are some of the many studies performed on the dam, see Johansson and Broberg (2017), Broberg et al. (2020) and Malm (2021).

This creates a unique opportunity to be able to study the pore pressure to a greater extent by using finite element methods which will increase the knowledge about the pore pressure measurements in these dams.



## 1.2 Aim and scope

In this thesis, the main objective is to study the real pore pressure distribution and its magnitude underneath the dam structure in order to better understand and increase knowledge about the uplift pressure and to further increase the certainty of the dam safety against sliding.

The pore pressure in the rock foundation can be influenced by many factors therefore, the aim is to first develop multiple finite element models with different conditions, assumptions and modeling techniques in order to capture the real distribution and magnitude of the uplift pressure. Secondly, these models are used to calibrate against available field measurements. Additionally, the model with the best agreement with the real conditions of the dam and measured pore pressure is further used to perform more comprehensive sensitivity analyses.

Moreover, the most calibrated model and other models which represent critical states of the dam are used to perform safety factor calculations. Result from these models are then compared with the analytically calculated results based on the guidelines.

Finally, the effect of deep fractures respectively the effect of the fracture friction angle on the sliding safety factor have been studied.

The following research questions should be answered during the course of this thesis:

1. How does rock fractures, grout curtain and drains affect the uplift pressure underneath the dam?
2. How does the numerical uplift pressure influence the safety factor against sliding compared to the guideline suggestions?
3. After which depth the rock foundation fractures should not be considered as a threat for the stability of the dam?
4. How does the fracture friction angle affect the sliding stability of the dam?

## 1.3 Limitations

The case study analyses are limited to Storfinnforsen buttress dam and specifically to monolith M42 which is the tallest monolith with the highest water reservoir. This monolith is expected to carry the highest uplift pressure and thus, considered as the worst-case scenario and therefore chosen to represent the case study. However, the methodology, the analyses and the conclusions of this research are to a large extent also expected to be applicable to other dams.

In addition, the analytical hand calculations regarding the distribution of the uplift pressure are limited to RIDAS and USACE guidelines, while the numerical analyses regarding the values of the applied loads and the safety factors are limited to only RIDAS guidelines.

Finally, all the calculations are limited to statical analyses, and the safety factor is only considered in terms of sliding failure.

## 1.4 Disposition

This thesis consist of eight chapters and a short general description of each chapter is listed below.

1. **Introduction:** The background history and the description of the problem is introduced. The objective of the thesis and the limitations are also defined in this chapter.
2. **Uplift pressure on concrete dams:** This chapter describes the existing theoretical background and proposed guidelines related to the uplift distribution and the ways that the bedrock parameters can influence it. The chapter begins with a general description of the uplift pressure followed by a summary of the effects of uplift pressure on buttress dams. Furthermore, considerations and assumptions made by different guidelines are described regarding the drainage system influence on the uplift. Moreover, the chapter continues by describing the bedrock parameters focusing on the discontinuities and their variables, that can influence the flow of water through them which can ultimately affect the uplift pressure distribution at the dam-rock interface. Finally, the chapter describes the conditions related to the safety factors according to RIDAS guideline.
3. **Storfinnforsen Monolith 42** This chapter describes information about Storfinnforsen concrete buttress dam which have been studied in this report. The current status of the dam related to its geometry and material properties, the sensor device positions, the rock fracture measurements and the measured pore pressure are presented.
4. **Numerical model** All the input data and other conditions that were used in order create the numerical model are described in this chapter. In other words, all the assumptions and interpretations of real structure have been described here.
5. **Pore pressure analysis:** This chapter summarize all the pore pressure results from the numerical simulations. Comparison between the field measurements and numerical result are also presented in this chapter.
6. **Sliding stability analysis:** This chapter summarizes and compares the resulting safety factors of the numerical models and the analytically calculated ones according to the guidelines for each sliding failure plane. Lastly, the results of the deep fractures and friction angle effect on the safety factors are presented.
7. **Discussion:** The meaning and the validity of the results obtained with the different methods are discussed and evaluated.
8. **Conclusion and further research:** This chapter presents short objective summary of the thesis and the author's insights, comments and conclusions. This chapter gives also recommendations for further research.

# Chapter 2

## Uplift pressure on concrete dams

### 2.1 Buttress dam structural system

Buttress dams are characterized by having an inclined front plate on the upstream side facing the reservoir and equally spaced supporting buttress in the downstream side. Buttress dams are the evolution of the older massive dams and they are typically modular structures where each module is called a monolith and each monolith is structurally independent and transfers the forces from the water in the reservoir through individual buttresses to the foundation (FERC, 1997). The joints between the monoliths must be hermetically sealed to prevent water leakage. Unlike massive dams, the buttress dam are normally reinforced due to its slender geometries. In Figure 2.1 a typical layout of a buttress dam and some of its main components are presented.

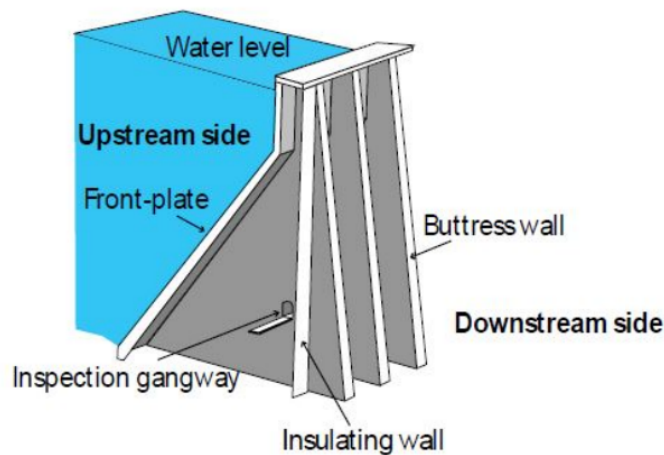


Figure 2.1: A schematic drawing of a typical buttress dam with definition of the main components (Isander et al., 2013)

There are slight variations of buttress structural systems, but a common factor for all buttress dams is that they all have an inclined front plate. The inclined front plate allows to take advantage of the stabilizing vertical force component from the upstream water on the dam (FERC, 1997). This additional stabilizing force allows to build buttress dams

with much slender geometries than massive dam and substantially decrease the amount of concrete used and consequently decrease the material costs. Due to buttress dams' small surface area in contact with the rock surface, the magnitude of uplift pressure is reduced substantially which can be seen as a great advantage.

Although the buttress dam design seems efficient in many ways, it has an important disadvantage. In the case of existing joints or fractures at the rock foundation, the uplift pressure can be much larger than expected (FERC, 1997). This combined with the small weight of the dam, can greatly decrease the resulting stabilizing forces and hence decrease its resistance to sliding and may result in stability issues.

## 2.2 Uplift pressure general theory

The uplift pressure is one of the major force affecting the sliding safety assessment in concrete dams founded on rock foundation (Ruggeri, 2004). The uplift pressure is pore water pressure, acting in the foundation underneath the dam structure and is defined as the unit weight of water times the depth beneath the piezometric surface.

It is considered to be one of the most influencing factors in dam safety analysis in many handbooks and guidelines. The uplift pressure pushes the dam structure upwards which consequently reduces the stabilizing force normal to the sliding plane. This pressure can occur between the structure and bedrock or inside the joints in the bedrock. Many failures of concrete dam structures are associated with lack of knowledge regarding this force. It was not even considered until late 19<sup>th</sup> century and early of the 20<sup>th</sup> (Westberg, 2007).

Specifically, the uplift pressure is the product of the seepage effect where the water moves through the voids of the soil or through the fractures of the rock foundation due to imbalance of waterhead on the different sides of the dam, hence water will try to flow from the high water level to the lower water level. The seepage effect can be described by the flow nets theory.

The principles of flow nets according to Nelson (1973) are:

- The material should be homogeneous and isotropic, thus the hydraulic conductivity is equal in all the directions  $K_j = K_x = K_y$ .
- The voids of the material should be filled with water hence saturated (constant flow).
- Darcy's law,  $Q = K_j \cdot i$  regarding flow in porous material and steady-flow condition (does not change in time) should be both applicable.

where,

$K_j$  is the hydraulic conductivity, [ m/s]  
 $i$  is the hydraulic or pressure gradient, [m/m]

As long as the mentioned principles apply, the flow nets can be described mathematically by using the Laplace equation for two dimension flow analysis according to Equation 2.1.

$$\frac{\theta_h^2}{\theta_x^2} + \frac{\theta_h^2}{\theta_y^2} = 0 \quad (2.1)$$

Equation 2.1 characterizes two orthogonal sets of curves which simulate the flow of water through material and these are:

- The equipotential lines
- The flow lines

The equipotential lines describe the way that the potential energy of the flow is distributed and the flow lines indicate the direction of the groundwater flow. At the points that the equipotential lines intersect the flow lines, these points have equal headwater thus equal energy. The headwater along any equipotential line can be calculated according to the Bernoulli Equation, as follows:

$$h = \frac{P_w}{\rho g} + \frac{v^2}{2g} + z \quad (2.2)$$

where,

$h$	is the hydraulic head (headwater), [m]
$P_w$	is the resulting water pressure, [kPa]
$\rho_w$	is the density of water, [kg/m <sup>3</sup> ]
$v$	is the water velocity, [m/s]
$g$	is the gravity acceleration, [m/s <sup>2</sup> ]
$h$	is the headwater or water energy measured at the equipotential line, [m]
$z$	is the headwater elevation, [m]

The first parameter of Equation 2.2 represents the flow work or the pressure head, the second part represents the kinetic energy and the last parameter indicates the potential energy of the streamline. By assuming that the kinetic energy along a joint is small thus  $v = 0$  m/s then Equation 2.2 can be simplified as follows to calculate the water pressure.

$$P_w = \rho_w \cdot g \cdot (h - z) \quad (2.3)$$

By considering an embankment dam as presented in Figure 2.2, due to piezometric head-loss from the upstream to downstream, the water will try to flow to the downstream side. Accordingly, the resulting flow net is shown in Figure 2.3.

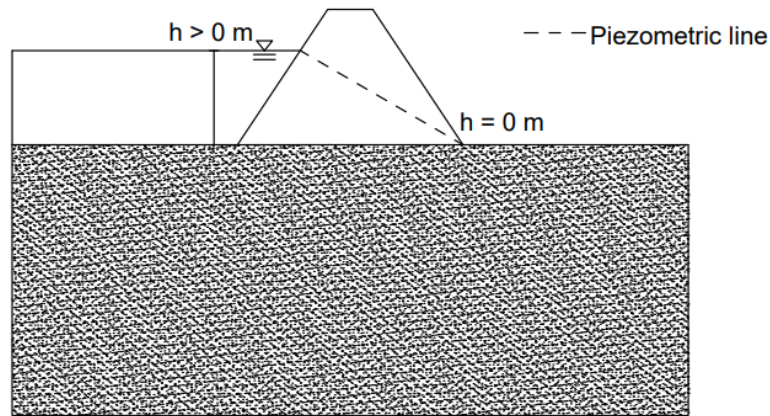


Figure 2.2: Embankment dam with full reservoir (reproduced from Nelson (1973))

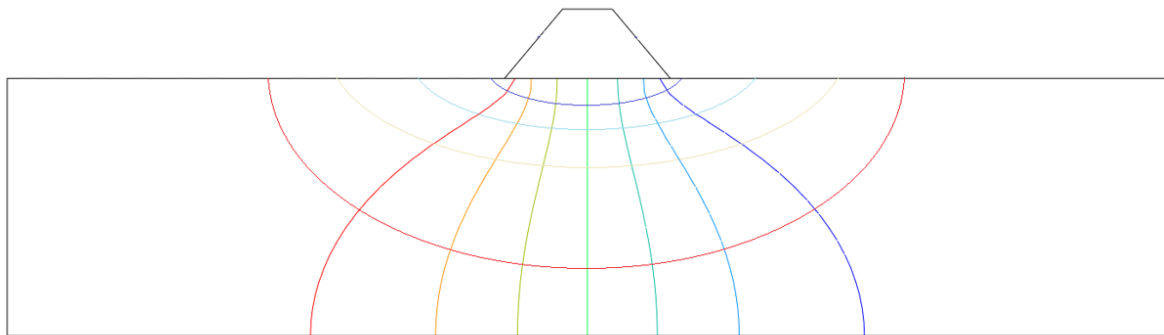


Figure 2.3: Resulting flow net of an embankment dam (reproduced from Nelson (1973))

The flow net graphical method can estimate the rate at which the flow discharges, the seepage pressure, the gradient, the uplift pressure and its distribution. The seepage transmits through the resulting flow channels of the flow net according to the following Figure 2.4. The notations ( $N_d$ ,  $N_d$ ,  $Q$ ,  $h$ ) in Figure 2.4 are explained in Equation 2.4.

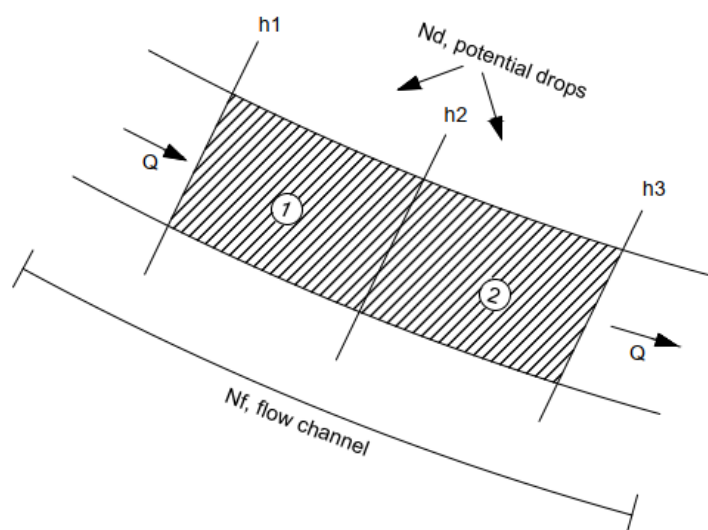


Figure 2.4: Seepage through a flow channel with square elements (Nelson, 1973)

The resulting flow (rate of seepage) per unit length is calculated according to the Equation 2.4.

$$Q = K_j \cdot \Delta h \cdot \frac{N_f}{N_d} \quad (2.4)$$

where,

$Q$	is the flow per unit length, [m <sup>3</sup> /s·m]
$K_j$	is the hydraulic conductivity (coefficient of permeability), [m/s]
$\Delta h$	is the headwater difference between each element, [m]
$N_d$	is number of potential drops (number of the square elements)
$N_f$	is number of flow channels in the flow net

All the current equilibrium methods of analysis regarding the stability of the dam structures include assumptions of loading and resisting loads. Based on the flow net theory, field measurements and laboratory experiments, the guidelines propose that the uplift pressure is linearly distributed and acts normal to the dam foundation as presented in Figure 2.5. However, problem emerges when determining the uplift pressure in heterogeneous foundations which have discrete rock discontinuities e.g. joints in the bedrock because the joints can result to nonlinear distribution of the uplift pressure, according also to Figure 2.5. The rest of this chapter is an attempt to describe the most important parameters and phenomenon effecting the uplift pressure underneath the dam structure or the potential failure plane.

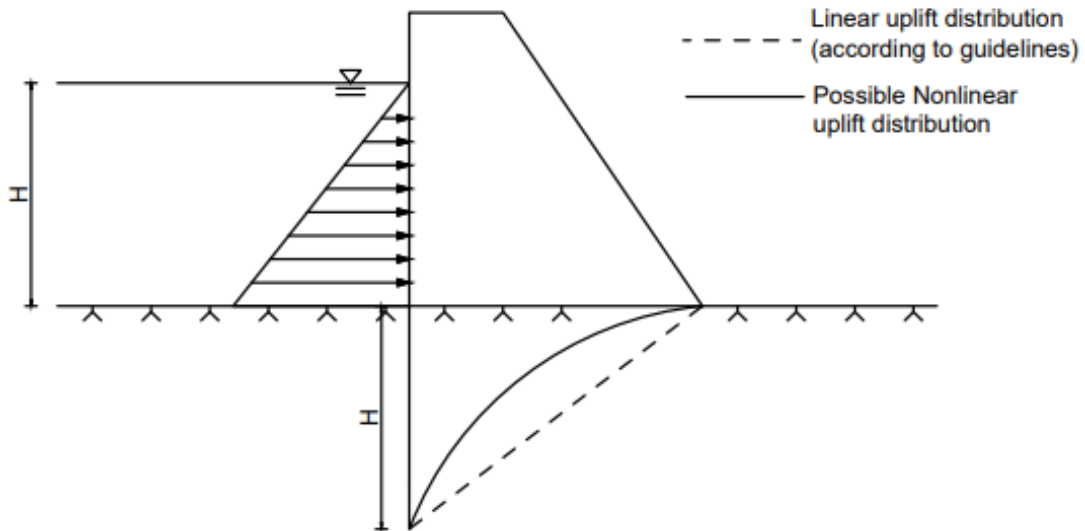


Figure 2.5: Possible uplift distribution assumptions (Ebeling and Pace, 1996a)

### 2.2.1 Considerations according to RIDAS guideline

RIDAS is the Swedish power companies' guidelines for dam safety. The guideline considers the overall assessment of the dam stability analysis and presents simplified cases on how to consider the uplift pressure. All the major guidelines for dam safety, consider the uplift pressure to act in a linear distribution below the dam, with the pressure varying linearly from upstream to the downstream in the absence of a drainage system. In the design process, the uplift pressure between the foundation and gravity dam structure is presented in Figure 2.6 according to RIDAS.

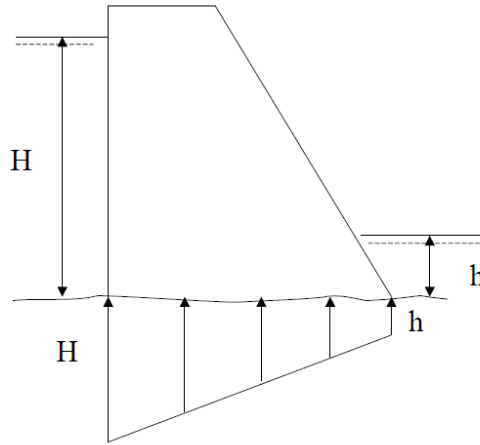


Figure 2.6: Uplift pressure distribution for massive gravity dams without drainage (RIDAS, 2020)

The uplift pressure at a buttress dam is distributed differently compared to a gravity dam. It is reduced in comparison to gravity dam structure since there are no influence of upstream water level on the buttresses and the width of the buttress slabs are relatively small compared to gravity dams. Thus, only the buttress frontplate due to its large width sustains high uplift pressure and not the whole dam body. A schematic visualization of uplift distribution on buttress dams is seen in Figure 2.7.

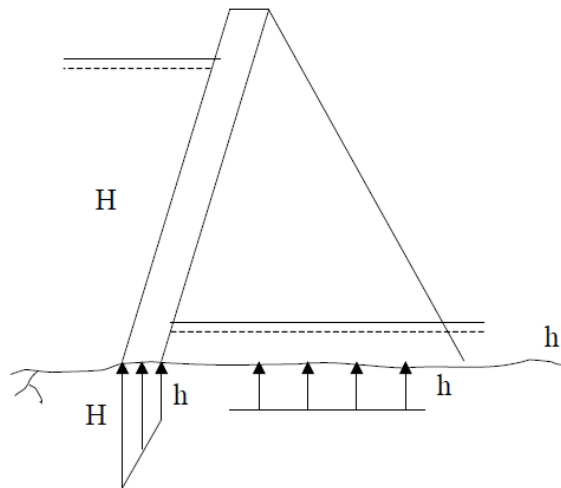


Figure 2.7: Uplift pressure distribution for buttress dams (RIDAS, 2020)



There are multiple factors influencing the real distribution of the uplift pressure such as the geometry of the dam, presence of drainage and the effect of the grout curtain. The effect of grout curtains is usually not included in the stability analysis rather, because it is considered as an extra safety factor (RIDAS, 2020). According to RIDAS, one factor that has the large influence on the uplift pressure is the presence of installed drainage system. In the case of uplift pressure in existing rock joints, there are two scenarios that are considered in RIDAS. In the first scenario, the cross-section is treated as a massive gravity dam where the drainage system is represented by a gallery above the ground surface. The reduction and the distribution of the uplift pressure in this scenario is presented in Figure 2.8. This is suitable when the rock foundation is defined as impermeable. The second scenario also considers massive gravity dams with the distinctive difference of the drainage system installed on the ground level. The reduction and distribution of the uplift pressure can be seen in Figure 2.9. This reduction of uplift pressure is assumed when the rock is defined as impermeable and the drainage gallery is installed inside the rock foundation. This reduction is higher since the drains are closer to the surface.

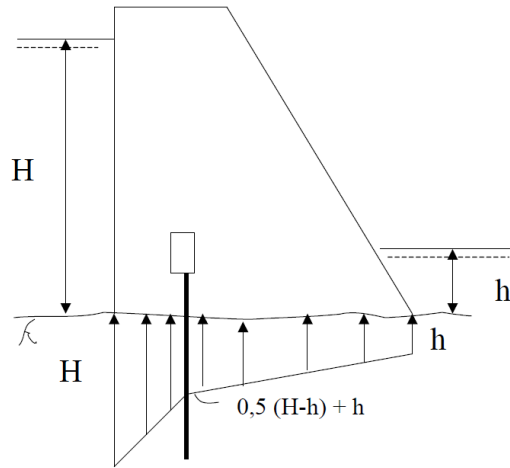


Figure 2.8: Uplift pressure in rock joints with drainage gallery installed on the ground surface (RIDAS, 2020)

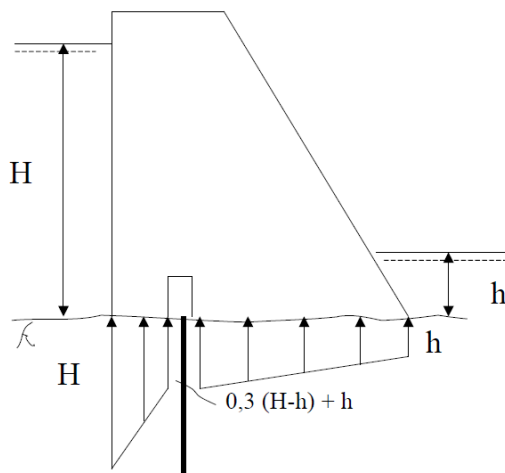


Figure 2.9: Uplift pressure in rock joints with drainage gallery installed inside the foundation (RIDAS, 2020)

According to RIDAS guidelines, another scenario emerges when tensile stresses are present at the upstream heel of the dam. Consequently, it is of great importance to perform full stress analyses at the dam foundation in order to detect any tensile stresses (RIDAS, 2020). Possible tensile stresses at the upstream heel of the dam could lead to cracks at that position which results in higher uplift pressures in the region compared to an uncracked condition. Consequently, full constant uplift pressure along the whole region is assumed. If the cracked region expands to the zone of influence of the drainage system, then the effect of the drainage system can not be utilized and therefore the drainage system is classified as non-functional. The proposed distribution of the uplift pressure in RIDAS, is presented in Figure 2.10.

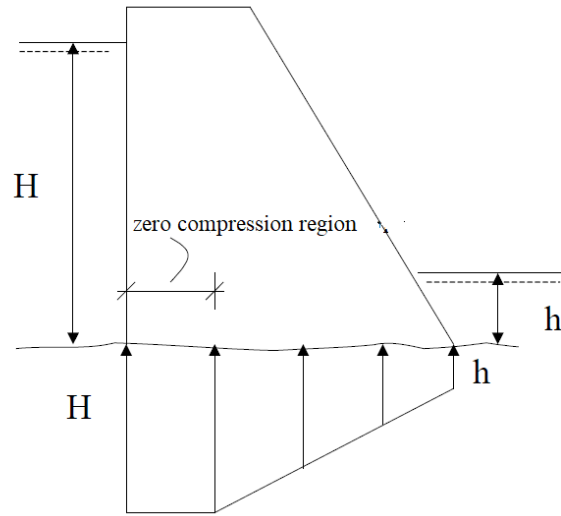


Figure 2.10: Distribution uplift pressure when tensile stresses are present at the heel of the dam (RIDAS, 2020)

In order to take advantage of the pressure-reducing effect of the drainage system, the function of the drainage holes must be monitored (RIDAS, 2020). One way to monitor the function of the drainage holes is to measure the pore pressure downstream to their location. Monitoring should be described in a measurement program and should be checked frequently enough to detect clogging or malfunction. The results of the measured pore pressure should not be used as input data for calculations or stability analysis, for the reason of possible clogging and the fact that uplift pressure distribution is dependent on specific load situations. Therefore, uplift measurements should be only used to verify the function of the drainage system and grout curtain according to RIDAS (2020).

Other parameters that the guideline considers in order to utilize the pressure reduction effect of the drainage system includes:

- The drainage holes should reach a depth of at least half of the water head level of the reservoir
- The distance between the holes should be between 1.5 - 3 m
- The diameter of the drainage holes should be around 75 - 100 mm

### 2.2.2 Considerations according to USACE guideline

According to the USACE guidelines, the uplift pressure is dependent on the effectiveness of the drainage system, the grout curtain and the geological characteristics such as the rock permeability, the existence of joints, etc (USACE, 1995). In the same way as RIDAS guidelines, it defines the uplift pressure distribution to vary linearly from the head water at the heel of the dam to zero or in some case to the tail water in the downstream toe of the dam. This is applicable when a new dam structure is designed, for example a new gravity dam. Also it could vary linearly when joint planes in rock foundation are calculated and no provisions are provided for uplift reductions. The distribution of the uplift pressure in such case can be seen in Figure 2.6.

Installing a drainage system on the dam will reduce uplift pressures at the base or below the foundation. The USACE guideline considers that the effectiveness of the drainage system depends on its depth, size, and spacing of the drainage holes, the characteristics of the foundation below the dam and availability of maintaining system as well as the frequency of the intervals. The effectiveness of the drainage system is assumed vary between 25% to 50% and sometimes can go up to 67% if supporting justification is provided by pore pressure measurements (USACE, 1995). The uplift distribution when the drainage system is active can be seen in Figure 2.11 and the uplift reduction at the drainage hole is expressed in Equation 2.5.

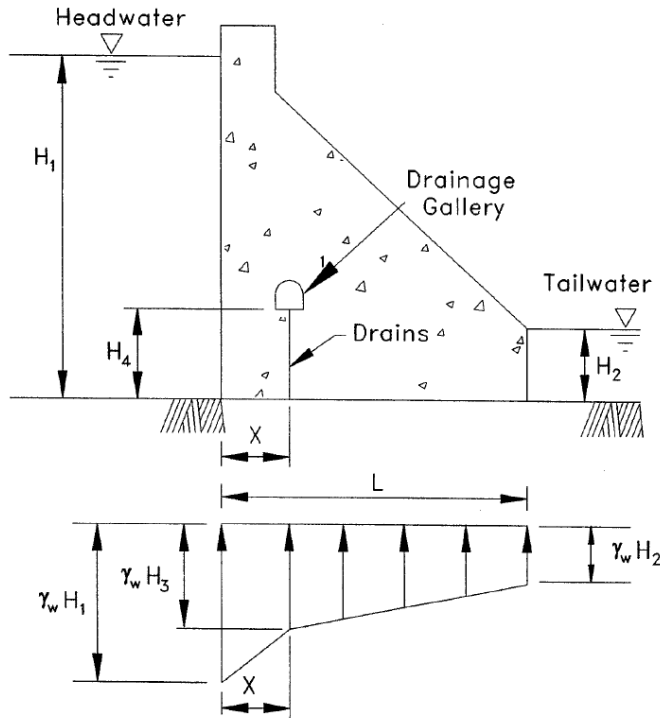


Figure 2.11: Uplift pressure distribution with drainage gallery (Ebeling et al., 2000)

$$H_3 = K \cdot (H_1 - H_4) \cdot \frac{(L - X)}{L} + H_4 \quad (2.5)$$

where,

$H_3$  is the reduced waterhead at the drainage system location, [m]

$E$  is drainage effectiveness, [-]

$K = 1 - E$ , [-]

If  $H_4 < H_2$ , then Equation 2.5 is rewritten as:

$$H_3 = K \cdot (H_1 - H_2) \cdot \frac{(L - X)}{L} + H_2 \quad (2.6)$$

where,

$H_4$  is the distance of the drainage system from the ground surface, [m]

$H_2$  is the height of the water level at the toe of the dam, [m]

Figure 2.12 illustrates the scenario that the foundation drains are close to the upstream side of the dam. This case is considered when the line of drains intersects the foundation at a distance less than 5% of the reservoir depth from the upstream side.

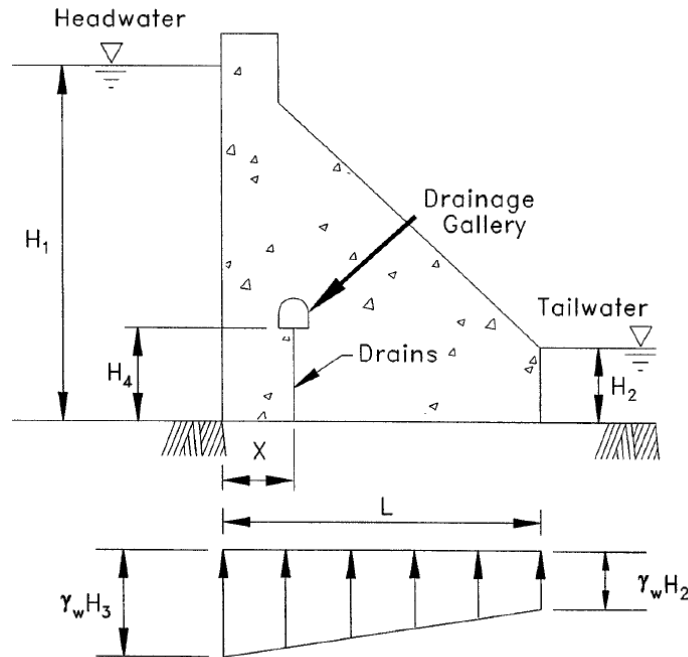


Figure 2.12: Uplift distribution with drains close to upstream side (Ebeling et al., 2000)

The distribution and depth of of the uplift pressure in this case is expressed in Equation 2.7 and 2.8 and is only used if  $x < 0.05H_1$ .

When:  $H_4 > H_2$ ,

$$H_3 = K \cdot (H_1 - H_4) + H_4 \quad (2.7)$$

When:  $H_4 < H_2$ ,

$$H_3 = K \cdot (H_1 - H_2) + H_2 \quad (2.8)$$

USACE guidelines also consider zero compression zones. All the parts of the foundation plane which are not in compression are considered to be loaded by full capacity uplift pressure, except when the tension is caused by instantaneous dynamic loading (USACE, 1995). The USACE guideline describes two scenarios regarding the zero compression zones condition in the foundation. First scenario is illustrated in Figure 2.13 and describes the state that the base is cracked but the compression zones do not extend beyond the drains.

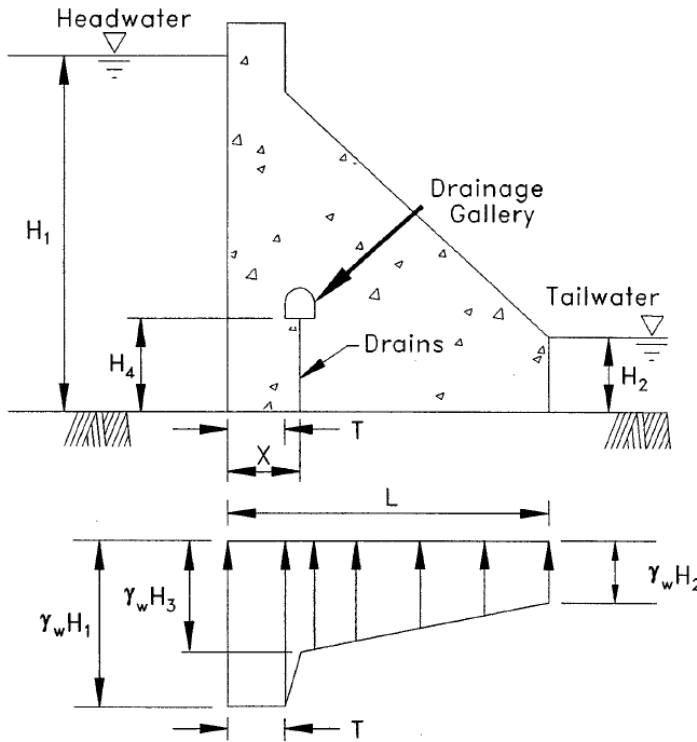


Figure 2.13: Uplift distribution cracked base with drainage, zero compression zone not extending beyond drains (Ebeling et al., 2000)

The distribution of the uplift pressure is expressed in Equations 2.9 and 2.10.

When:  $H_4 > H_2$ ,

$$H_3 = K \cdot \left[ (H_1 - H_2) \cdot \frac{L - X}{L - T} \right] + H_4 \quad (2.9)$$

When:  $H_4 < H_2$ ,

$$H_3 = K \cdot \left[ (H_1 - H_2) \cdot \frac{L - X}{L - T} \right] + H_2 \quad (2.10)$$

where,

T is the length of zero compression region, [m].

The case where the zero compression zone is extended beyond the drains, results to disregarding of the drainage effect. This situation is illustrated in the Figure 2.14.

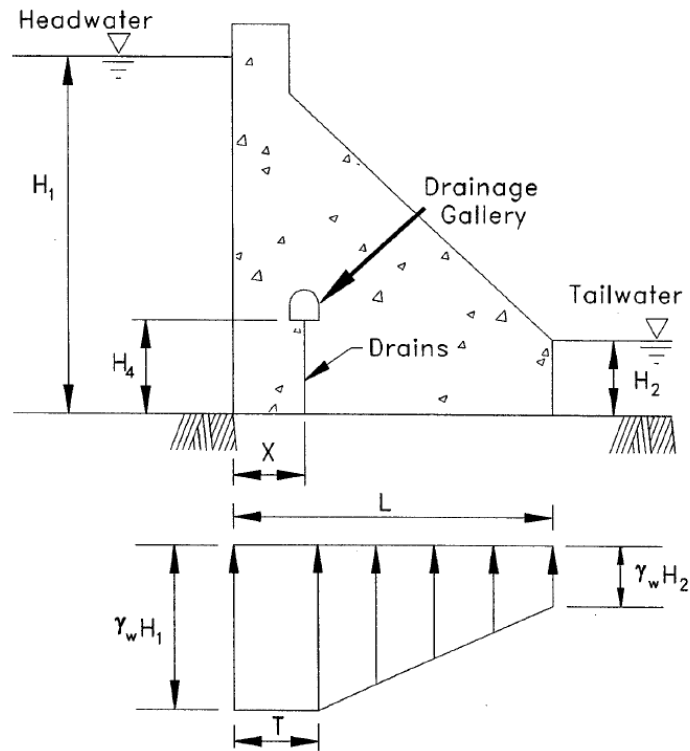


Figure 2.14: Uplift distribution cracked base with drainage and zero compression zone extending beyond drains (Ebeling et al., 2000)

## 2.3 Effect of grout curtain

The grout curtain is normally installed in the bedrock foundation below the upstream part of the dam and its main purpose is to reduce the water leakage through the bedrock (RIDAS, 2020). It can reduce the uplift pressure up to 50%, see Figure 2.15.

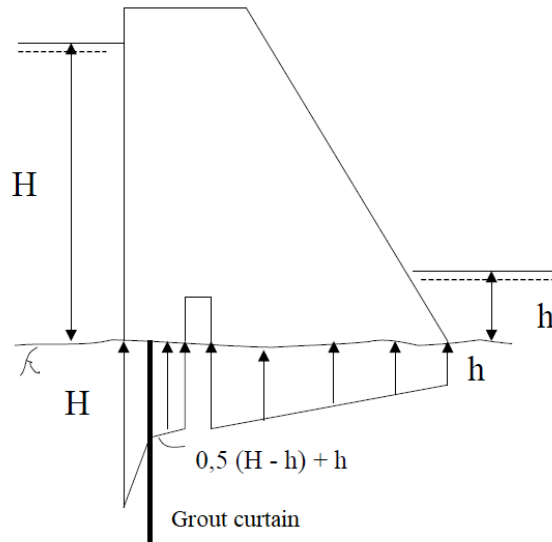


Figure 2.15: Uplift distribution with drainage and grout curtain (RIDAS, 2020)

However, the effect may diminish over time as the grout curtain can eventually be leached by water flowing through. Consequently, the grout curtain can only be considered as an extra safety factor, unless uplift measurements and re-injection of the grout curtain is performed, if necessary. If the reduction of the grout curtain is utilized in the stability assessment of the dam, then it is required to include re-injection of the grout curtain in the maintenance plan (RIDAS, 2020).

## 2.4 Influence of the bedrock foundation

The buttress dam is less resistant to uplift forces due to the fact that it is a light weight structure compared to a massive gravity dam and therefore it is very important to investigate and determine the bedrock properties because they are responsible for the distribution of the uplift forces (Royet and Peyras, 2013). In order to do that, a geological and a mechanical model of the rock foundation has to be created (Royet and Peyras, 2013).

The geological model provides information regarding the:

- stratigraphy of the terrain
- type of the rock and its physical characteristic values
- formation of the discontinuities
- hydraulic conditions of the foundation material (permeability, porosity)

The mechanical model consists of the dam structure and its material properties combined with the indications and the data that are provided from the geological model in order to define a rock foundation model (Royet and Peyras, 2013). Moreover, by analyzing different load case scenarios, it is determined the behaviour of the structure correlated to the rock mass interaction (Royet and Peyras, 2013).

For existing structures such as the Storfinnforsen dam, the geotechnical model is constantly getting updated according to field measurements in-situ tests such as borehole samples and piezometers that measure the pore pressure at the bedrock joints (Johansson, 2005).

### 2.4.1 Rock mass

The rock mass consists of intact rock and discontinuities, thus it is a heterogeneous,porous discontinuous material with anisotropic behaviour (Zang, 2006; Johansson, 2005). The combination of both will determine the global behaviour of the rock mass but it will be mostly affected by the type, the formation and the characteristics of the discontinuities. The quality of the rock mass can be determined by RQD (Rock Quality Designation) tests which are core samples extracted by the bedrock layer (Zang, 2006; Johansson, 2005). The following figure is presenting the configuration of a typical rock mass.



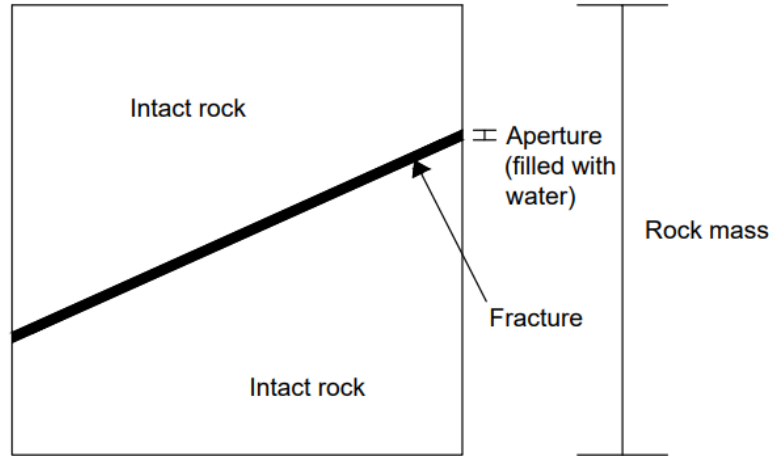


Figure 2.16: Intact rock and joint components within rock mass (Zang, 2006)

### 2.4.2 Intact rock

Intact rock is considered the rock block that is not fractured between the discontinuities of the total rock mass and it has a different mechanical behavior hence it is stiffer and stronger compared to the total rock mass that was obtained (Lindfors, 1996; Zang, 2006).

The intact rock can essentially help the dam to resist the uplift forces because it acts at the same direction as the self-weight of the dam. In this sense it can be assumed that the intact rock block is also part of the monolith (Lindfors, 1996; Zang, 2006). Consequently, the deeper a joint develops, the less the uplift forces affect the dam plus different fracture patterns should be considered during the analysis (Johansson, 2005).

### 2.4.3 Rock Discontinuities

The discontinuities could be any defect that separates the rock mass and is characterized by zero or very small tensile strength which that they can deform easily and displace (Lindfors, 1996; Johansson, 2005). Discontinuity is a general term and can refer to joints, bedding planes, faults, planes of schistosity, shear zones etc (Lindfors, 1996; Zang, 2006).

Joints represent a geological origin break where no relative movement is noticed parallel to its plane. They are responsible for the flow of the water through the rock mass and therefore the main variable that defines the way that the uplift forces are distributed at the dam-rock foundation interface. The water flow is mainly affected by the orientation, the spacing, the aperture, the roughness, the filling, the persistence and the resulting hydraulic conductivity of the joint system (Murphy et al., 2002; Grenoble and Amadei, 1990). All of these characteristics can vary along the joint in all directions (length, width, depth) and also through the passage of time which result to many uncertainties especially for existing dams that the accessibility to the dam foundation rock mass is limited (Johansson, 2005).

Therefore, even by extracting many borehole samples it is unclear if they produce the real conditions because they represent just few points of the bedrock mass and there is a low

degree of confidence in extrapolating these measurement data for the whole foundation mass (Grenoble and Amadei, 1990).

The joint parameters that are going to be examined and that affect greatly the uplift distribution and the development of the uplift pressure are:

- orientation
- roughness
- aperture
- interconnectivity
- hydraulic conductivity

**Orientation** is the attitude of a joint in space (Zang, 2006). Specifically, it is characterized by its strike and dip direction. The strike is the direction of a horizontal line within the plane and it is measured with degrees relative to the true north or degrees of azimuth measured clockwise (Zang, 2006). The dip is measured perpendicular to the strike (dip direction) and is ranging between  $0^\circ$  and  $90^\circ$  that the plane makes with the horizontal line (line of maximum dip) according to Figure 2.17.

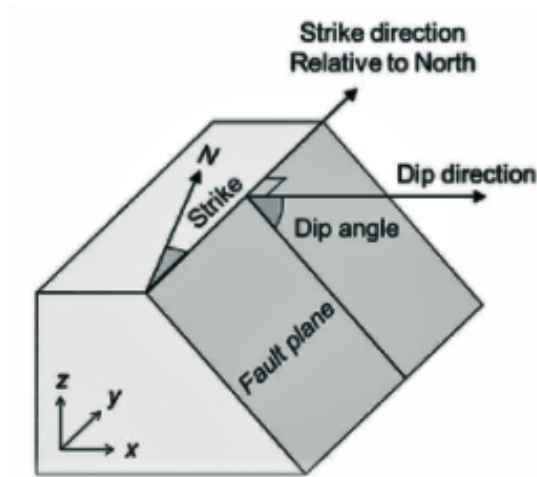


Figure 2.17: Strike and dip direction of a joint (Markou and Papanastasiou, 2018)

The joint orientation is mostly related to cause stability issues and each joint plane should be checked individually for sliding failure especially the sub-horizontal ones located close to surface (Johansson, 2005).

Moreover, the orientation does not significantly affect the flow conditions in the joint but it defines the block size of the intact rock that will decrease the resulting uplift forces which start from the bottom level of the dam to the depth of the examined joint (Grenoble and Amadei, 1990). Consequently, it can be assumed that the joints closer to surface will be more critical for the stability of the dam (Grenoble and Amadei, 1990).

**Roughness** of the joint walls is an important parameter that governs the flow of the water through the joint (Murphy et al., 2002; Grenoble and Amadei, 1990). In order to describe the water flow (Murphy et al., 2002), the Darcy's law is applied where the prerequisites of the Darcy's law are:

- laminar conditions through the pipe should be applied
- the height of the asperities (JRC) that describe the roughness of the joint walls should be translated into an equivalent smooth wall plate aperture

Therefore, the physical aperture of the joint is simulated to a theoretical one according to Figure 2.18:

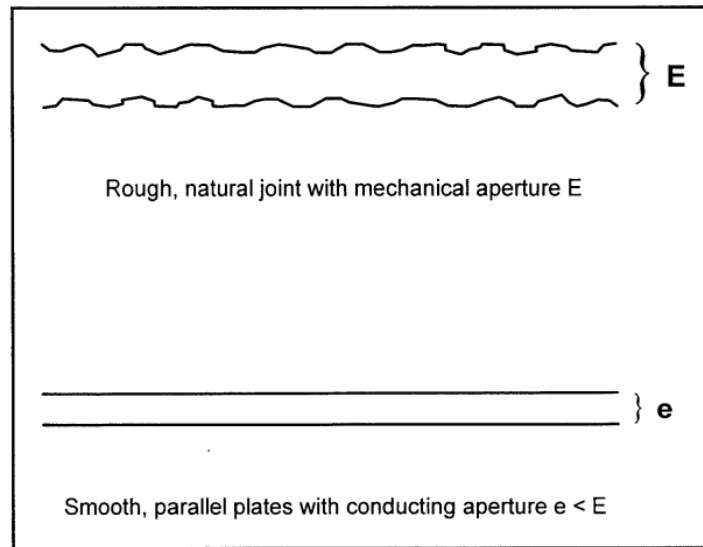


Figure 2.18: Translation of the physical aperture to a theoretical aperture (Murphy et al., 2002)

The roughness is also responsible for the shear strength of the joint that define the possible shear plane failures (slip condition) (Murphy et al., 2002; Grenoble and Amadei, 1990).

**Aperture** can be defined as the size of the joint opening which is the perpendicular separating distance between two rock walls (Zang, 2006). The interceding space could be filled with different kinds of soil, water, or could even be empty (air filled) (ISRM, 1978). The size of the aperture affects the hydraulic conductivity, the degree of porosity, the shear strength and the deformability of the rock mass. The joints are characterized as tight with an aperture varying between 0.10-0.25 mm and open with an aperture ranging between 0.50-10 mm (ISRM, 1978). Lastly, the aperture can be measured in-situ by using borehole survey cameras or physically from extracted borehole samples (Johansson and Broberg, 2017).

In order to define mathematical expressions and calculate the water flow through the joints, they can be idealized as a closed tube with continuous flat walls which allow for laminar conditions (Murphy et al., 2002; Grenoble and Amadei, 1990).

The most common assumption is that the aperture size remains constant along the joint which results in a linear distributed uplift pressure beneath the dam according to Figure 2.19 (Murphy et al., 2002).

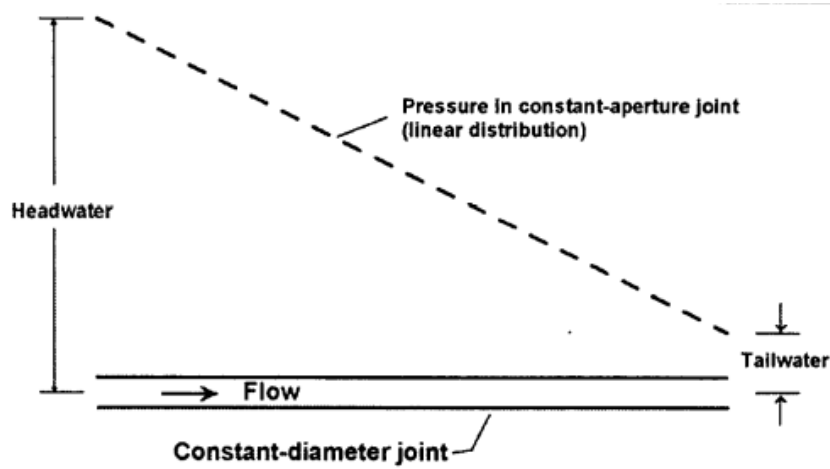


Figure 2.19: Linearly distributed pressure from the heel to the toe of a dam (Murphy et al., 2002)

In contrary, a joint with varying aperture results in a nonlinear uplift distribution (Murphy et al., 2002). Consequently, according to Figure 2.20 the joint can be modeled with a large aperture starting from the heel and a smaller aperture in the toe of the dam. It can be assumed larger aperture at the start of the joint because higher pressures are acting at this location due to the reservoir induced water pressure which is producing larger aperture deformations and also higher hydraulic conductivity (Murphy et al., 2002).

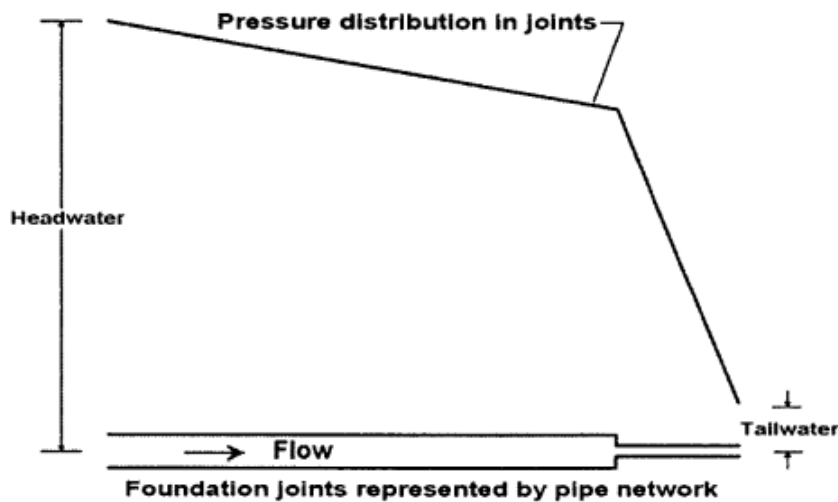


Figure 2.20: Nonlinear distributed pressure by a two-pipe network (Murphy et al., 2002)

It is noticed that the intensity of the pressure decreases abruptly when the aperture change occurs due to high friction losses (Murphy et al., 2002).

Furthermore, a more realistic approach is to simulate the joint as a tapered pipe where the aperture at the heel gradually decrease until the toe of the dam (Murphy et al., 2002). As mentioned previously, this is a good approach because higher pressures are acting at the start of the joint and they decline slowly along the joint while in the same way are acting the formed deformations that affect the diameter (aperture size) of the fracture as presented in Figure 2.21 (Murphy et al., 2002). In this sense, more variation in aperture will lead to a more curved uplift pressure (Murphy et al., 2002).

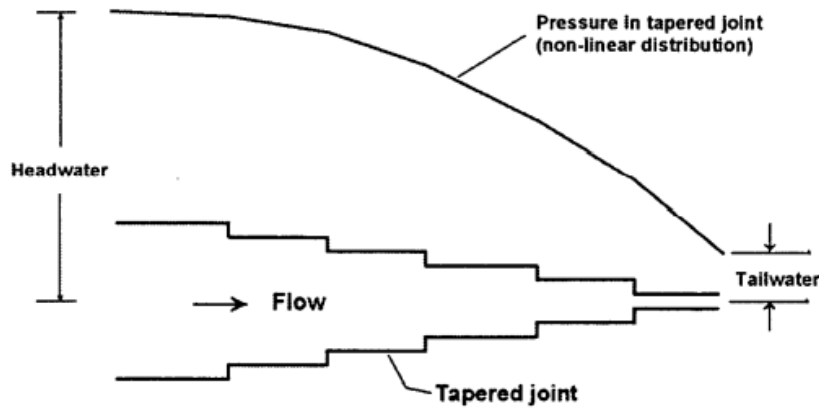


Figure 2.21: Nonlinear distributed pressure by a tapered joint (Murphy et al., 2002)

**Interconnectivity** is the condition that different joints can connect to each other in some points and allow water flow (EPRI, 1992). The degree of interconnection between the joints and their length can change the distribution of the uplift pressure (EPRI, 1992). The influence of the joint length at the uplift pressure is presented in Figures 2.22 and 2.23 where both of the pipes are described by same parameters except their length  $L$ . It is shown that the longer pipe with  $L + \Delta L$  at the Figure 2.23 results to a higher pressure compared to the shorter pipe at the Figure 2.22. This happens because the pressure in the short pipe decreases at a higher rate compared to the long one (EPRI, 1992). Therefore, a more persistent joint would result to a higher uplift pressure and higher potential failure (EPRI, 1992).

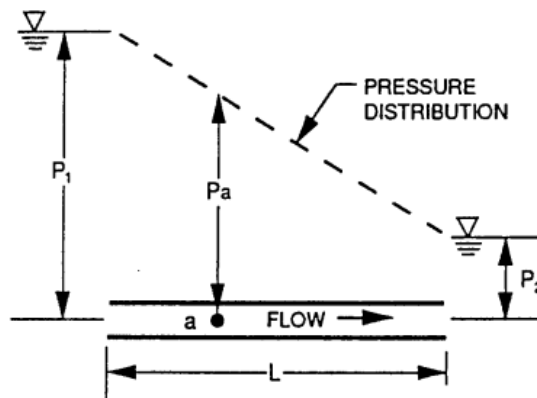


Figure 2.22: Uplift distribution in a short joint (pipe) (EPRI, 1992)

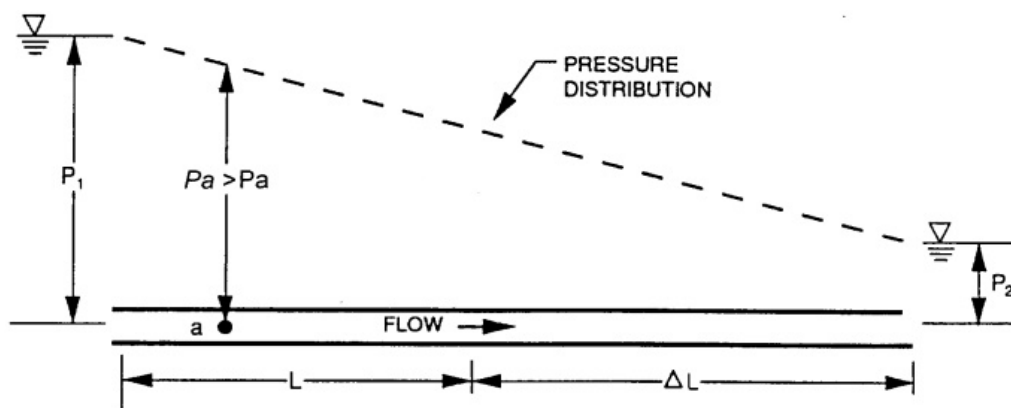


Figure 2.23: Uplift distribution in a long joint (pipe) (higher pressure compared to Figure 2.22) (EPRI, 1992)

The interconnection of joints can greatly affect the permeability of the rock mass and essentially define its hydraulic conductivity (EPRI, 1992). The joint can only act as flow path as long as it connects with other discrete joints or if it is expanded throughout the area of interest (EPRI, 1992). According to Figure 2.24, the uplift pressure is decreasing much faster at the joint characterized by a small aperture compared to the joint with the large one. This occurs due to the high frictional losses that take place in the first one (EPRI, 1992).

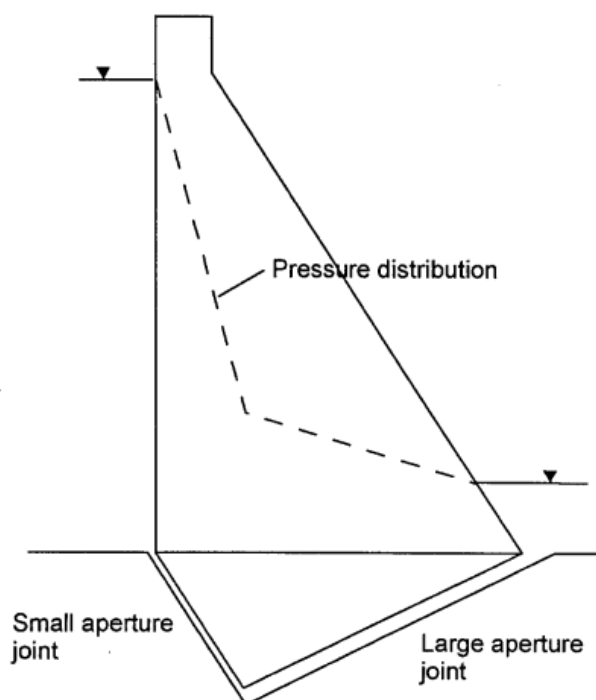


Figure 2.24: Uplift distribution related to joint interconnectivity and aperture size (EPRI, 1992)

Moreover, according to Figure 2.25, in case of unconnected joints, the water stays trapped in the joint and therefore the pressure at the joint is the same with the headwater pressure of the reservoir (EPRI, 1992).

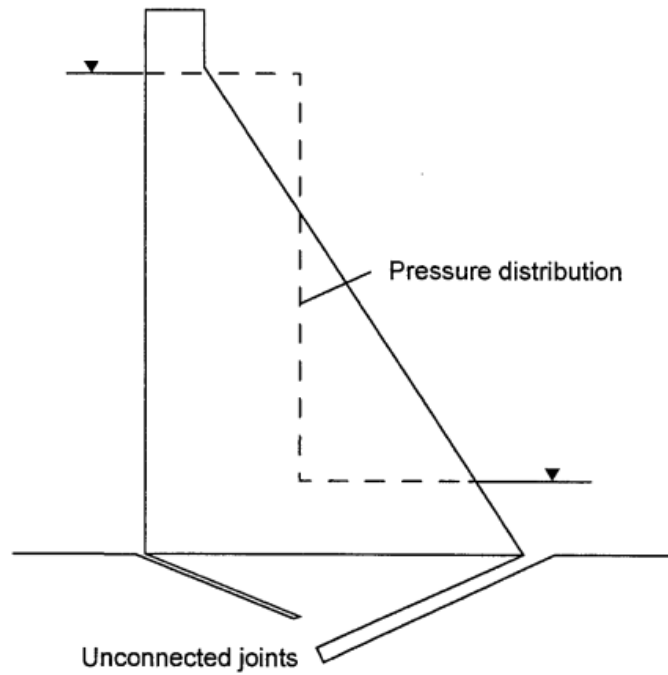


Figure 2.25: Uplift distribution related to unconnected joints (EPRI, 1992)

Lastly, in case of a highly interconnected system of joints, the rock mass behaves can be modeled as porous continuum material and the pressure distributes linearly from upstream to the downstream level (Johansson, 2005).

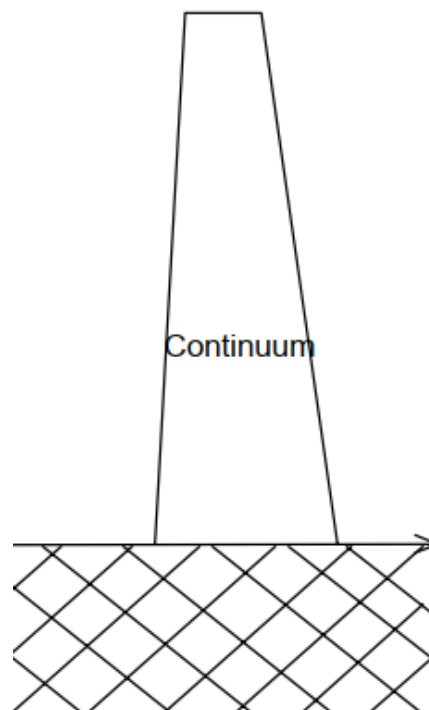


Figure 2.26: Constant discontinuities and continuum approach (Johansson, 2005)

**Hydraulic conductivity** can be generally described as the ease that the fluid can move through the rock fractures (Ebeling and Pace, 1996b). It depends on the permeability of the medium plus the viscosity and the density of the fluid. More specifically, it is determined as the discharge velocity through a section area under a pressure gradient (Ebeling and Pace, 1996b). Consequently, it is expressed by Equation 2.11.

$$K_j = k \cdot \frac{\gamma_w}{\mu_w} \longrightarrow K_j = \frac{\gamma_w}{12\mu_w} \cdot e^2 \quad (2.11)$$

where,

$\gamma_w$  is the specific weight of the water, [N/m<sup>3</sup>]  
 $\mu_w$  is the dynamic viscosity of the water, [N · s/m<sup>2</sup>]  
 $e$  is the aperture size of the fracture, [m]

It should be mentioned that according to Snow's equation, the permeability  $k$  is calculated as presented in Equation 2.12.

$$k = \frac{e^2}{12} \quad (2.12)$$

where,

$k$  is the intrinsic permeability, [m<sup>2</sup>]

Furthermore, the hydraulic or pressure gradient  $i$  is described as the difference in the hydraulic head over a distance along the flow path (Woessner and Poeter, 2020). It is a gradient of mechanical energy which is the driving force of groundwater flow (Woessner and Poeter, 2020). For example, if the water is not moving, the gradient is zero and therefore the value of headwater is the same everywhere (Woessner and Poeter, 2020). It can also be described as the head loss of the along an one-dimensional water flow (Zang, 2006). Therefore, it is defined by Equation 2.13.

$$i = \frac{\Delta h}{\Delta L} \quad (2.13)$$

where,

$i$  is the hydraulic or pressure gradient, [m/m]  
 $\Delta_h$  is the headwater difference along the flow line, [m]  
 $\Delta_L$  is the length difference, [m]

Moreover, the water flow is described mathematically by Darcy's law where the flow of the fluid related to the hydraulic conductivity and is equal to Equation 2.14 (Ebeling and Pace, 1996a).

$$Q = K_j \cdot i \cdot A_{flow} \quad (2.14)$$



where,

$A_{flow}$  is the cross-section area of the aperture, [m]

Finally, according to the Cubic law which relates the theoretical aperture  $e$  to the  $Q$  flow rate per width, by combining the Equations 2.11 and 2.14, the flow  $Q$  can be defined as follows:

$$Q = \frac{\gamma_w}{12\mu_w} \cdot i \cdot e^3 \quad (2.15)$$

#### 2.4.4 Wedge support implementation

Due to the existence of joints in the rock mass, additional failure planes can be created which individually or combined should be checked for sliding failure (USACE, 1995). The rock block that is increasing the lateral stability of the dam due to its ability to resist the movement of a formed sliding plane, is defined as resisting or passive wedge while the intact rock that is formed according to the joint orientation and resists the uplift forces is defined as a structural wedge because it increases the downforce of the dam, thus it can be assumed that is part of the monolith (USACE, 1995).

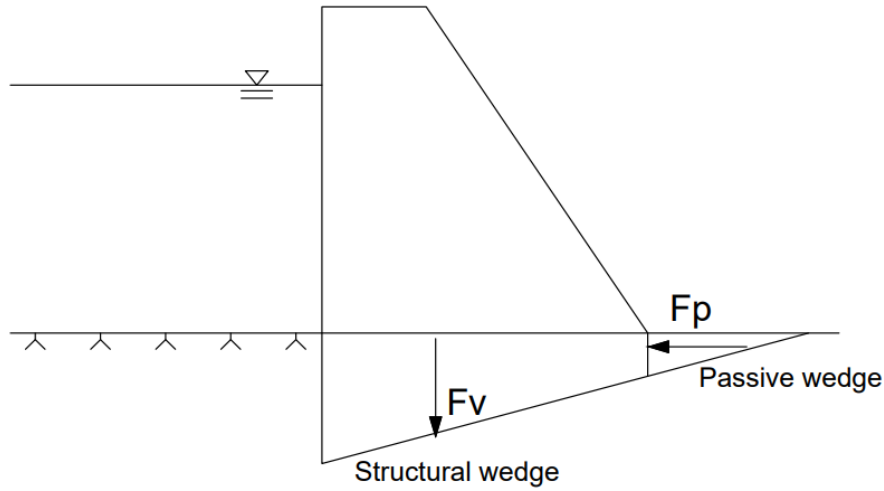


Figure 2.27: Wedge formation (Johansson, 2005)

The area of the structural wedge due to uncertainties could be adjusted in order to define the worst case scenario, hence the smallest sliding safety factor (Spross et al., 2014). The developing uplift forces are assumed to act along the length of the fracture as presented in Figure 2.28.

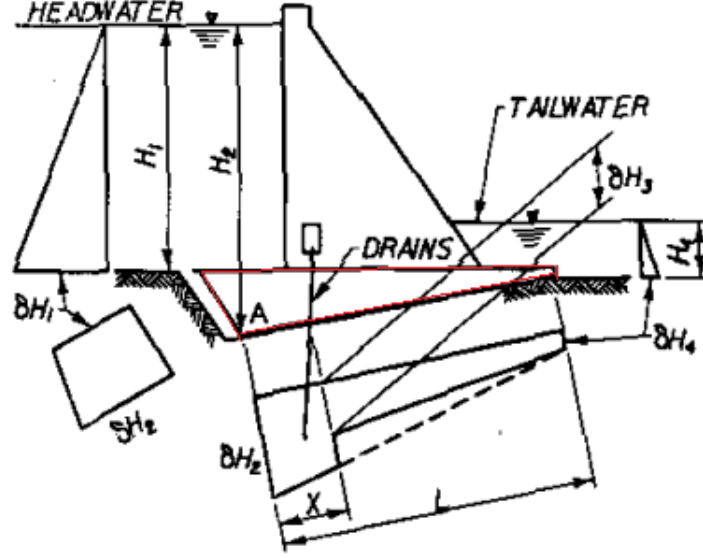


Figure 2.28: Developing uplift pressure and wedge formation (USACE, 1995)

According to Figure 2.28, the horizontal water pressure of the reservoir is extended linearly along the wedge and the uplift pressure has the same initial value as the maximum horizontal at point A. The drains can operate effectively only if they penetrate the fracture, hence if there are uncertainties or insufficient data regarding the functionality of the drains (clogged, unclogged) then it can be assumed that the uplift will vary linearly as represented by the dashed line (USACE, 1995).

In order to calculate the resisting force of the passive wedge the following Equation 2.16 can be used (Spross et al., 2014).

$$F_p = (V_p \cdot \gamma_r - U_p) \tan(\phi + \theta) \quad (2.16)$$

where,

- $F_p$  is the resisting force of the passive rock wedge, [kN]
- $V_p$  is the volume of the passive rock wedge, [m<sup>3</sup>]
- $\gamma_r$  is the density of the passive rock wedge, [kN/m<sup>3</sup>]
- $U_p$  is the resulting uplift force affecting the passive rock wedge, [kN]
- $\phi$  is the friction angle of the rock fracture, [°]
- $\theta$  is the inclination of the wedge, [°]

The inclination of the wedge is calculated according to Equation 2.17 (Spross et al., 2014).

$$\theta = 45 - \frac{\phi}{2} \quad (2.17)$$

### 2.4.5 Sliding safety factor

The safety factor regarding sliding according to RIDAS guideline is assessed by calculating a coefficient of friction  $\mu$  which represents the sum of the horizontal forces  $\Sigma_H$  that invoke sliding (instability) divided by the sum of the vertical forces  $\Sigma_V$  that increase the stability of the dam (RIDAS, 2020). The coefficient of friction  $\mu$  is compared with the available coefficient of friction  $\mu_{till}$  which is divided by the suggested (RIDAS) safety factor  $S_f$  (RIDAS, 2020). The sliding failure criteria is presented in Equation 2.18.

$$\mu = \frac{\Sigma_H}{\Sigma_V} \leq \mu_{till} = \frac{\tan(\delta_g)}{S_f} \quad (2.18)$$

Thus, the safety factor  $S_f$  is calculated according to the Equation 2.19.

$$S_f = \frac{\tan(\delta_g)}{\mu} \quad (2.19)$$

where,

- $\mu$  is the resulting coefficient of friction, [-]
- $\Sigma_H$  is the sum of the horizontal forces, [kN]
- $\Sigma_V$  is the sum of the vertical forces, [kN]
- $\mu_{till}$  is the required coefficient of friction, [-]
- $\tan\delta_g$  is the limit value of the friction coefficient in the sliding surface, [-]
- $S_f$  is the suggested safety factor, [-]

The suggested RIDAS safety factors in sliding are determined by the the material property of the rock foundation and the category of the load case and they are equal to:

- $S_f = 1.35$  for normal load case
- $S_f = 1.15$  for exceptional load case
- $S_f = 1.05$  for accidental load case

Finally, the sliding failure criteria should be fulfilled for all existing joints in the bedrock foundation that could invoke sliding instability and definitely at the dam-rock foundation interface (USACE, 1995; RIDAS, 2020).

### 2.4.6 Pore pressure analysis in Abaqus software

A porous medium is considered as a multiphase material in Abaqus and an effective stress principle is adopted for its behaviour (ABAQUS, 2014). Accordingly, it is considered that it consists of two fluids where the one is the “wetting liquid,” which is assumed to be nearly incompressible and the other which is relatively compressible (ABAQUS, 2014). For example, it could be a partially saturated soil where both fluids exist at a point. When the soil is fully saturated by the wetting fluid the voids are completely filled.

The porous medium is simulated by fixing the finite element mesh to the solid phase, thus the fluid can flow through this mesh (ABAQUS, 2014). Overall, the mechanical part of the model is based on the effective stress principle while the model also uses a continuity equation for the mass of wetting fluid in a unit volume of the medium (ABAQUS, 2014).

**Effective Stress Principle for porous media** where the total stress acting on a point is assumed to consist of an average pressure stress in the wetting fluid, named as “Pore pressure” times the degree of saturation, therefore the resulting “effective stress” that is applied in the material skeleton is defined in the Equation 2.20 (ABAQUS, 2014).

$$\bar{\sigma} = \sigma + (\chi u_w + (1 - \chi) u_a) I \quad (2.20)$$

where,

- $\bar{\sigma}$  is the effective stress, [Pa]
- $\sigma$  is the total stress, [Pa]
- $\chi$  is the degree of saturation, [-]
- $u_w$  is the average pressure stress in the wetting fluid, [Pa]
- $u_a$  is the average pressure stress in the non-wetting fluid, [Pa]

By considering fully saturation conditions parameter  $\chi$  becomes equal to 1 ( $\chi=1.00$ ) and that  $u_a$  is negligible Equation 2.20 is simplified to the following Equation 2.21.

$$\bar{\sigma} = \sigma + u_w I \quad (2.21)$$

Furthermore, it is assumed that the constitutive response of the porous medium consists of simple bulk elasticity relationships for the liquid and for the soil grains, together with a constitutive theory for the soil skeleton whereby  $\bar{\sigma}$  is defined as a function of the strain history and temperature of the soil by Equation 2.22 (ABAQUS, 2014).

$$\bar{\sigma} = (\text{strainhistory}, \text{temperature}, \text{statevariables}). \quad (2.22)$$

Accordingly, the strain rate decomposition is accordingly defined by the Equation 2.23.

$$d\epsilon = (d\epsilon_g^{vol} + d\epsilon_w^{vol}) I + d\epsilon^{el} + d\epsilon^{pl} \quad (2.23)$$

where,

- $d\epsilon_g^{vol}$  is the volume strain rate of the solid grains, [-]
- $d\epsilon_w^{vol}$  is the volume strain rate of the fluid, [-]
- $d\epsilon^{el}$  is the elastic strain rate in the material skeleton, [-]
- $d\epsilon^{pl}$  is the s the volume strain rate of the fluid, [-]

Finally, the discretized equilibrium state for a porous medium is defined by applying stress equilibrium for the solid phase of the material and is expressed by writing the principle of the virtual work for the volume under consideration in its current configuration at time  $t$  according to the Equation 2.24 (ABAQUS, 2014).

$$\int_V (\bar{\sigma} + u_w I) : \delta \epsilon \, dV = \int_S t \cdot \delta_\nu \, dS + \int_V f \cdot \delta_\nu \, dV + \int_V (s n + n_t) \rho_w g \cdot \delta_\nu \, dV \quad (2.24)$$

where,

- $\delta_\epsilon$  is the virtual rate of deformation, [-]
- $\bar{\sigma}$  is the effective stress, [Pa]
- $\delta_\nu$  is the virtual velocity field, [m/s]
- $t$  is surface tractions per unit area
- $f$  are the body forces (excluding fluid weight per unit volume), [N]
- $\rho_w$  is the density of the fluid, [kg/m<sup>3</sup>]
- $g$  is the gravity acceleration, [m/s<sup>2</sup>]

Finally, the virtual rate of velocity  $\delta_\nu$  and the virtual rate of deformation  $\delta_\epsilon$  are expressed in Equations 2.25 and 2.26.

$$\delta_\nu = N^N \delta_\nu^N \quad (2.25)$$

$$\delta_\epsilon = \beta^N \delta_\nu^N = sym \left( \frac{\partial \delta N^N}{\partial x} \right) \quad (2.26)$$

Equation 2.24 is then discretized using a Lagrangian formulation for the solid phase, with displacements as the nodal variable. The porous medium is thus modeled by attaching the finite element mesh to the solid phase and fluid may flow through this mesh (ABAQUS, 2014).

**Permeability** which according to Forchheimer's law, high flow velocities have the effect of reducing the effective permeability and, therefore, "choking" pore fluid flow. As the fluid flow velocity reduces, Forchheimer's law approximates the well-known Darcy's law (ABAQUS, 2014). Darcy's law can, therefore, be used directly in Abaqus by omitting the velocity-dependent term in Forchheimer's law (ABAQUS, 2014).

Accordingly, Forchheimer's law is written as:

$$f(1 + \beta\sqrt{\nu_w \cdot \nu_w}) = -\frac{k_s}{\gamma_w}k \cdot \left( \frac{\partial u_w}{\partial x} - \rho_w g \right) \quad (2.27)$$

where,

- $f$  is the effective velocity of the wetting liquid, [m<sup>3</sup>/s]
- $\beta$  is a velocity coefficient, [-]
- $\nu_w$  is the fluid velocity, [m/s]
- $k_s$  is the dependence of permeability on saturation of the wetting liquid, [-]
- $k$  is the permeability of the fully saturated medium, [m<sup>2</sup>]
- $\gamma_w$  is the specific weight of the water, [N/m<sup>3</sup>]
- $u_w$  is the wetting liquid pore pressure, [Pa]
- $x$  is the position (spatial coordinate), [m]

The effective velocity of the wetting liquid  $f$  is equal to:

$$f = sn\nu_w \quad (2.28)$$

where,

- $s$  is the fluid saturation ( $s=1.00$ , fully saturated condition)
- $n$  is the porosity of the porous medium

Moreover, the fluid saturation  $s$  is equal to:

$$s = \frac{dV_w}{dV_v} \quad (2.29)$$

where,

- $dV_w$  is the wetting fluid volume in the medium
- $dV_v$  is the void volume in the medium

Lastly, the porosity of the porous medium is equal to:

$$n = \frac{dV_v}{dV} \quad (2.30)$$

where,

- $dV$  is the total volume of the medium

**Continuity statement for the wetting liquid phase in a porous medium** where it should be considered a volume containing a fixed amount of solid matter while the volume occupies space  $V$  with surface  $S$  (ABAQUS, 2014). In this configuration it occupied space  $V^0$  and the wetting liquid can flow through this volume where its volume is denoted as  $V_w$ . The wetting liquid can also become trapped in the volume, by absorption into the gel and its volume is written as  $V_t$  (ABAQUS, 2014).

The total mass of wetting liquid in the control volume in a point is:

$$\int_V \rho_w [dV_w + dV_t] = \int_V \rho_w (n_w + n_t) dV \quad (2.31)$$

where,

$n_w$  is volume ratio of the free wetting liquid  
 $n_t$  is volume ratio of the trapped wetting liquid

By including the time rate of change of wetting liquid mass in Abaqus, the wetting liquid mass crossing the surface and entering the volume per unit time and the addition of liquid mass across the surface  $S$  to the rate of change of liquid mass within the volume  $V$  gives the wetting liquid mass continuity equation which is equal to:

$$\int_V \frac{1}{J} \frac{d}{dt} (J \rho_w (n_w + n_t)) dV = - \int_S \rho_w n_w \mathbf{n} \cdot \nu_w dS \quad (2.32)$$

where,

$-\int_S \rho_w n_w \mathbf{n} \cdot \nu_w dS$  is the mass of the wetting liquid accross the surface  $S$   
 $\nu_w$  is the average velocity of the wetting liquid in the solid phase (seepage velocity)  
 $n$  is the outward normal to the surface  $S$

By using the divergence theorem and because the volume is arbitrary, this provides the pointwise equation:

$$\frac{1}{J} \frac{d}{dt} (J \rho_w (n_w + n_t)) + \frac{\partial}{\partial x} \cdot (\rho_w n_w \nu_w) = 0 \quad (2.33)$$

Finally, in Abaqus this continuity statement is integrated approximately in time by the backward Euler formula and over the current volume  $V$ . By dropping the subscript  $t+\Delta_t$  and by adopting the convention that any quantity not explicitly associated with a point in time is taken at  $t+\Delta_t$  and by normalizing the previous equation by the density of the liquid in the reference configuration,  $\rho_w^0$  while  $n_w = sn$  then previous equation becomes:

$$\begin{aligned} \int_V \left[ \delta u_w \left( \frac{\rho_w}{\rho_w^0} (sn + n_t) - \frac{1}{J} \left( \frac{\rho_w}{\rho_w^0} J (sn + n_t) \right)_t - \Delta t \frac{\rho_w}{\rho_w^0} sn \frac{\partial \delta u_w}{\partial x} \cdot \nu_w \right) dV \right. \\ \left. + \Delta t \int_S \delta u_w \frac{\rho_w}{\rho_w^0} sn \mathbf{n} \cdot \nu_w dS \right] = 0 \end{aligned} \quad (2.34)$$

where,

$\delta u_w$  is an arbitrary, continuous, variational field.

The discretized equilibrium equations together with the continuity formulation for a wetting fluid in a porous media described above both define the state of the porous medium (ABAQUS, 2014).





## Chapter 3

### Storfinnforsen Monolith 42

Storfinnforsen is a hydropower dam located on Faxälven in the northern part of Sweden and was constructed between the years 1948 to 1954 (Alcalá Perales, 2016). Due to recent borehole surveys, it was noticed the presence of joints in the rock foundation that could increase the intensity of the uplift forces and initiate stability issues. Therefore, drains were installed to decrease the uplift pressure and piezometers to monitor the level of the groundwater pore pressure.

To the present, the main goal of this case study is to predict the real uplift pressure distribution underneath the dam structure and define the dam safety in terms of sliding failure at the existing fractures in the rock foundation.

Storfinnforsen is one of the largest hydropower dams in Sweden and is approximately 1200 m in length, where a part of 800 m is constructed as a concrete buttress dam, with 81 monoliths and the remaining part of 400 m is constructed as an embankment dam (Svensen, 2016). The connection of the two dams occurs at monolith 1, see Figure 3.1. The height of the monoliths at the buttress dam structure varies from 6 m up to 41 m and each monolith acts independently where the structural elements transfer the forces through friction to each other (Nilsson and Sandström, 2020). In order to specify the study and decrease the analysis time, the case study is performed for only one particular monolith, in this case monolith 42.

The chosen monolith is the tallest monolith and due to its height, higher water pressures develop, thus it represents the worst case scenario. The position of the monolith 42 relative to the dam is illustrated in Figures 3.1 and 3.2.

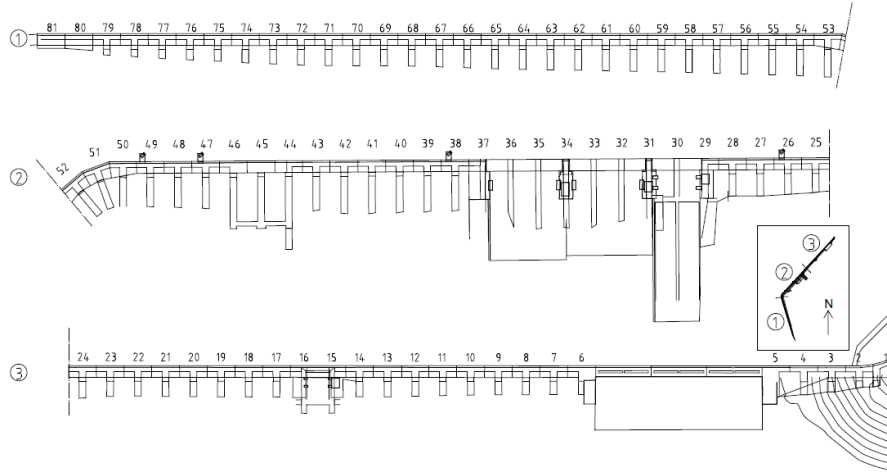


Figure 3.1: Situation plan of Storfinnforsen dam, Figure from Sweco Energuide AB (2013b).

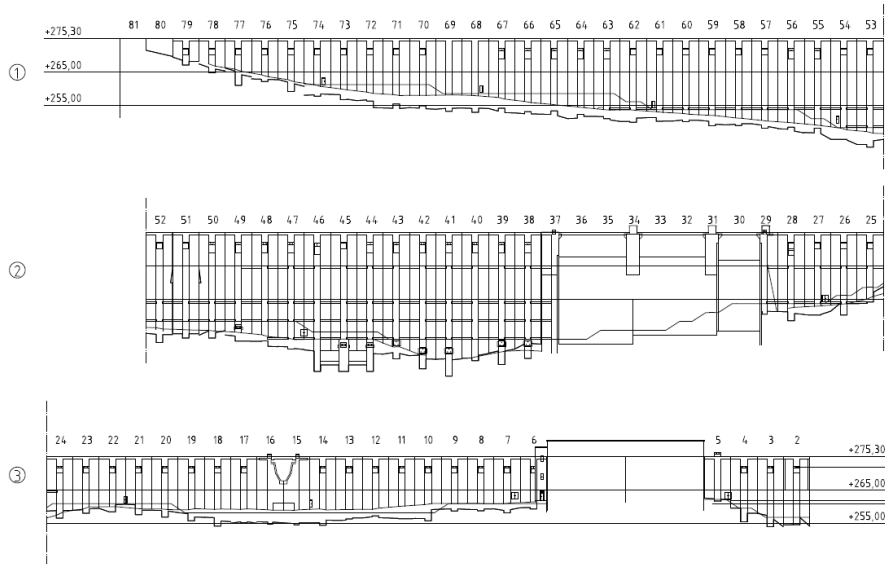


Figure 3.2: Situation plan of Storfinnforsen dam, Figure from Sweco Energuide AB (2013a).

Moreover, the monolith 42 possible water reservoir levels are the following (Malm, 2021):

- Retention water level: +273.0 m
- Minimum water level: +272.5 m
- The crest of the dam: +275.25 m

Furthermore, a detailed side drawing of the buttress dam with all the technical specifications is represented in the Figure 3.3.

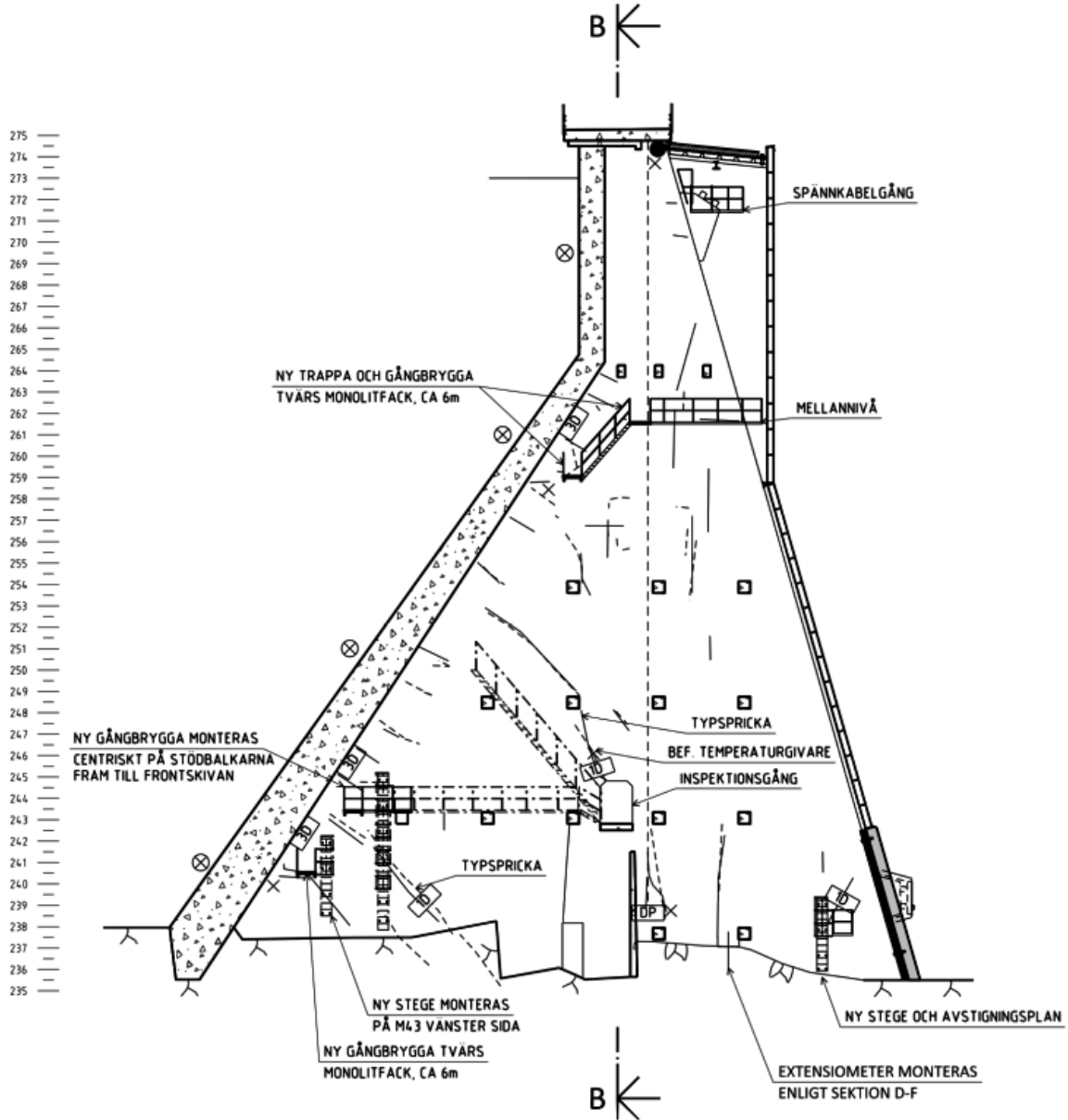


Figure 3.3: Detailed drawing of the right side of Monolith 42 (Malm, 2021)

### 3.1 Geometry of the monolith

Monolith 42 consists of an inclined front plate at upstream side and slender buttress at downstream of the dam and the height of the monolith is 41.40 m. The length of the buttress is 35.70 m with a thickness of 2.00 m. The front plate is 8.00 m wide and the top vertical part is 1.20 m thick, while the inclined part of the front plate varies between 1.20 m at the top to 2.60 at the base.

There is an existing crest deck which works as a road with a thickness of 0.80 m and a width of 5.00 m. There is also an inspection gangway at the monolith placed at a depth of 8.70 m above the foundation. The front plate is inclined  $126^\circ$  in relation to the ground level and also the support slab has a smaller inclination of  $106^\circ$  according to the technical drawing in Figure 3.4.

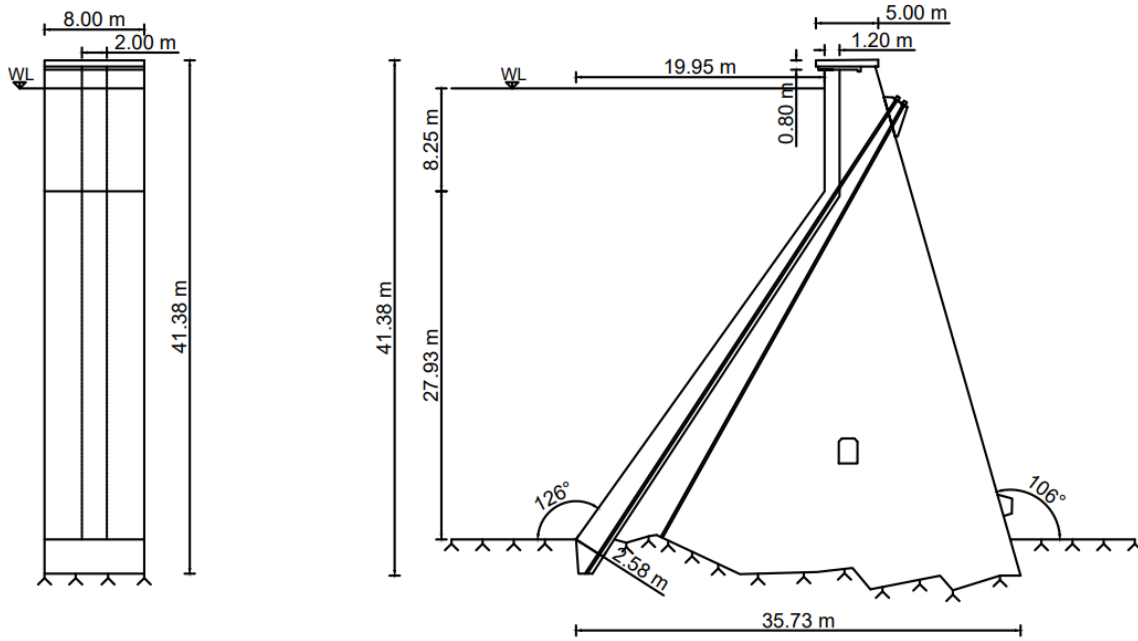


Figure 3.4: Calculation drawing of the front side and the right side of Monolith 42

## 3.2 Drainage holes and piezometers

There are three drainage holes between the monoliths and there is also two holes for the installation of the pore-pressure sensors between each monolith. Figure 3.5 illustrates the placement of the drainage holes and positioning of the holes for installation of piezometer sensors.

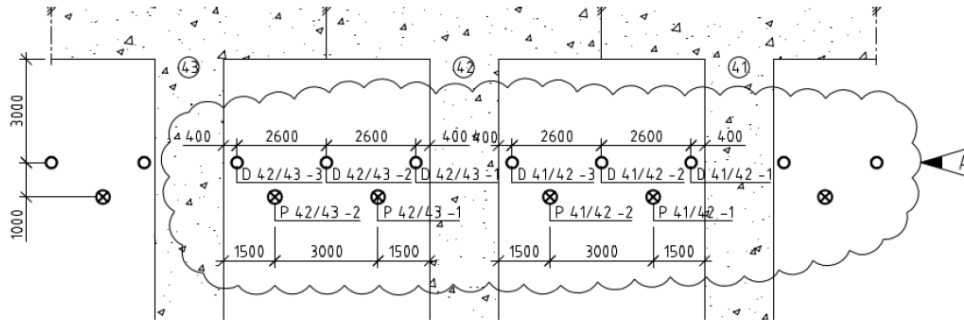


Figure 3.5: The location of the drainage holes (circles) and the piezometer sensors (circles with cross), based on drawing 7722-012-0011. (Malm, 2021)

The diameter of the drilled drainage holes is 80 mm and the depth of the drainage holes closest to monolith 42 varies between 18 to 19.2 m. The depth of these drainage holes is summarized in Table 3.1.

Table 3.1: Depth of the drainage holes, from drawing 7700-040

Monoliths	Name	Depth [m]
41/42	D1	18
	D2	19.2
	D3	18.6
42/43	D1	18
	D2	18.2
	D3	18.1

The pore water pressure is measured with two piezometers installed between the monoliths. The depth of the drainage holes for the installation of the pore-pressure sensors is close to 6.00 m. According to the Figure 3.6, the tip of the BAT-sensor is placed 200 mm from the bottom of the drilled holes and therefore, the measurements are conducted in a depth of around 5.80 m according to (Malm, 2021).

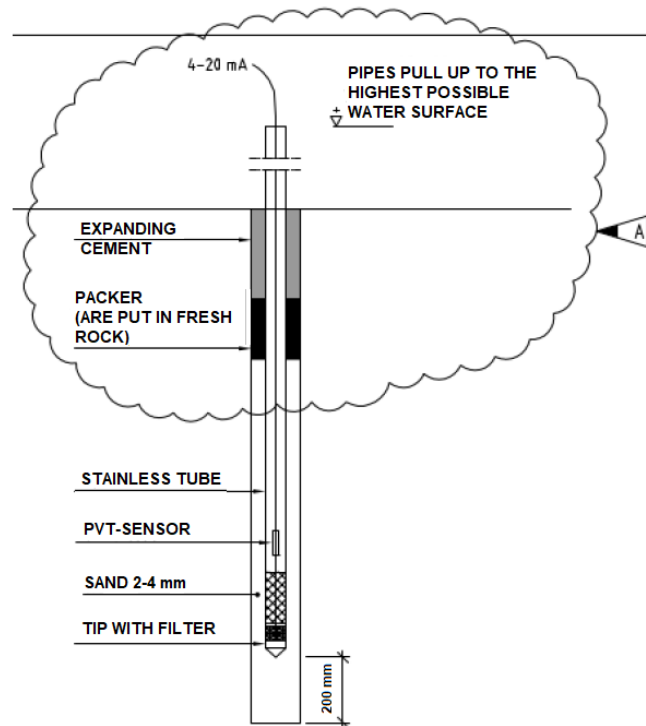


Figure 3.6: Illustration of installed piezometer sensor (Malm, 2021)

### 3.3 Measured pore pressure

The measured pore pressure is taken by sensors that are located as close as possible to the examined monolith. The piezometer holes that are located closer to the monolith 42 are P42/43-1 and P41/42-1 according to Figure 3.5 and there are installed the sensors denoted as M42-B02H and M42-B01V respectively. The resulting pore pressure measurements of each sensor are presented in Figures 3.7 and 3.8.

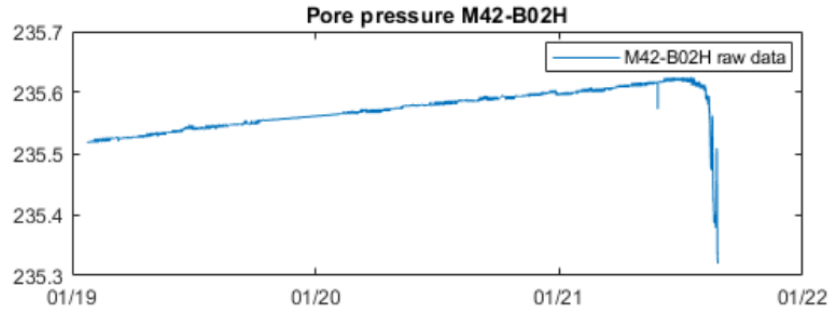


Figure 3.7: M42-B02H measured pore pressure values where in the x-axis indicates month/year and the y-axis the hydraulic head (m.a.s.l.)

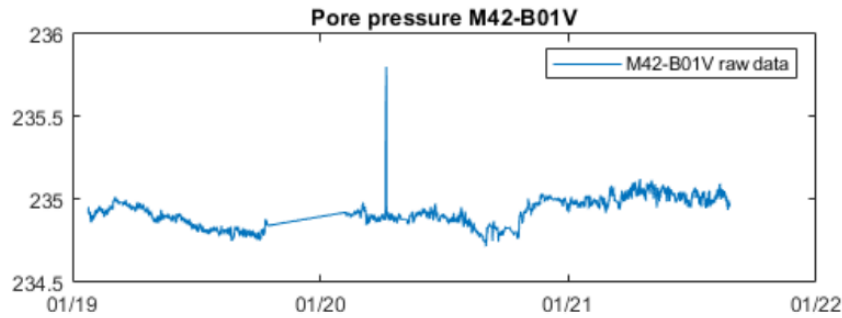


Figure 3.8: M42-B01V measured pore pressure values where in the x-axis indicates month/year and the y-axis the hydraulic head (m.a.s.l.)

Figure 3.7 shows that the pore pressure has a linear development from 01/19 until the mid of 2021 where the values are ranging from +235.5 m to +235.6 m. This linear increase could be due to clogging. On the contrary, a constant decline is observed after 06/2021 where the pressure dropped at +235.3 m which could be possibly be related to cleaning the drainage holes (Malm, 2021).

The signal in Figure 3.8 has several small variations which are probably caused due to seasonal weather conditions that are affecting the reservoir level of the dam which increases during winter and decreases during summer. The values are varying between +234.9 m to +235.1m where a spike is observed with a value equal to +235.8 m but this is an unrealistic behaviour because it happened for very small time duration and it is not noticed again throughout the duration of the measurements. This is probably caused by a faulty registration of the sensor.

Overall, a good approximation of the hydraulic head according to both of the piezometers and by considering their distance from the dam body would be +235.1 m.

### 3.4 Rock fractures

The existence of potential sliding planes in the rock foundation at monolith 42 (M42) was observed from the drainage hole D42/43-1 which is located between the monoliths 42-43 and specifically adjacent to the monolith 42. The exact position is depicted in Figure 3.5 and the investigation was performed by using optical tele-viewer (BIPS-logging)(Johansson and Broberg, 2017). The study concluded that there are persistent joints that could lead to potential failure planes and the obtained results are summarized in Table 3.2.

Table 3.2: Discontinuities within the rock mass under monolith 42 and 43 in Storfinnforsen concrete buttress dam, based on BIPS-logging field measurements (Johansson and Broberg, 2017).

Borehole	Depth [m]	Dip direction [°]	Dip [°]	Aperture [mm]
D42/43-1	0.89	363	-30	4
	0.95	10	28	4
	2.44	180	26	7
	3.65	164	9	9
	5.39	284	22	5
	8.32	240	23	2

The joints closer to the surface, with the largest aperture and with the less inclination (dip) could be the most critical to produce failure planes. Accordingly, the fractures closer to the surface that are more susceptible to sliding are presented at the following Figure 3.9 and they are depicted with red colour.

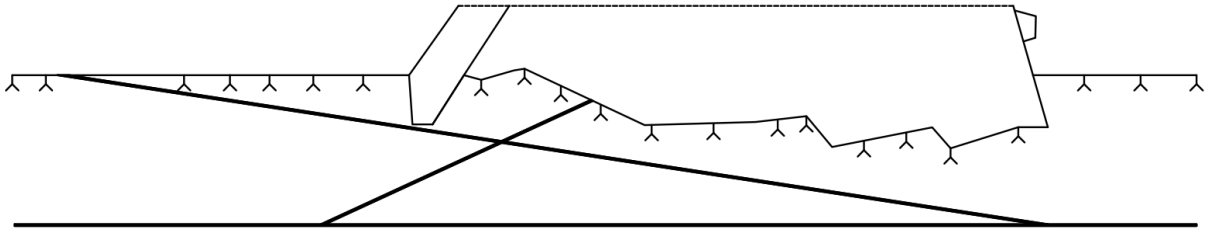


Figure 3.9: Illustration of the fracture pattern at the rock foundation

Finally, it was determined that fractures in the rock foundation did not have many filling areas and their surface was relative hard throughout their length, consequently the fracture friction angle was determined equal to  $\phi = 36^\circ$  (Johansson and Broberg, 2017; Falcão de Queiroz, 2018).

### 3.5 Sliding failure cases

The sliding failure criteria should be fulfilled for all existing rock fractures according to USACE and RIDAS guidelines, therefore different cases were assumed due to the existence of several fractures and different ways that the uplift and horizontal water pressure could act on the dam monolith. In this sense, the Cases A and B were defined which are discussed in the following subsections.

#### 3.5.1 Case A: crushed inclined fracture $\phi_{frac} = 8.97^\circ$

In Case A, it is assumed that the part of the fracture that extends below the bottom of the reservoir will be crushed due to high uplift forces, thus the horizontal water pressure is extended below the ground level until the initial point of the fracture and only the part of the inclined fracture that extends along the dam body is considered. The developed hydrostatic loads and the uplift forces are presented in Figure 3.10.

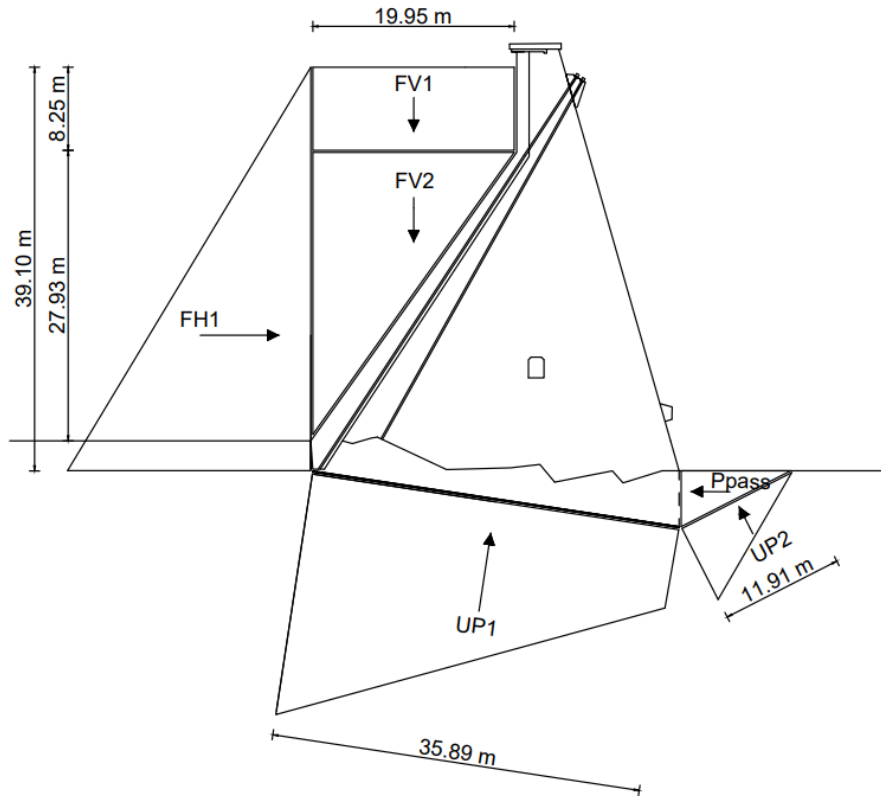


Figure 3.10: Considered horizontal and uplift water pressure according to Case A





Finally, safety factors were calculated for each state and were compared with the safety factors that were calculated with the numerical extracted uplift forces.

### 3.6 Influence of deep fractures

The intention of this investigation was to see how the depth of the fractures influence the safety of the dam. This was accomplished by using the most calibrated model and the failure scenario that gave the lowest safety factors and that was defined as the most prone to happen. The investigated sliding plane was positioned with the same geometry in different depths where an illustration of the different locations that the fracture plane was positioned is presented in Figure 3.12.

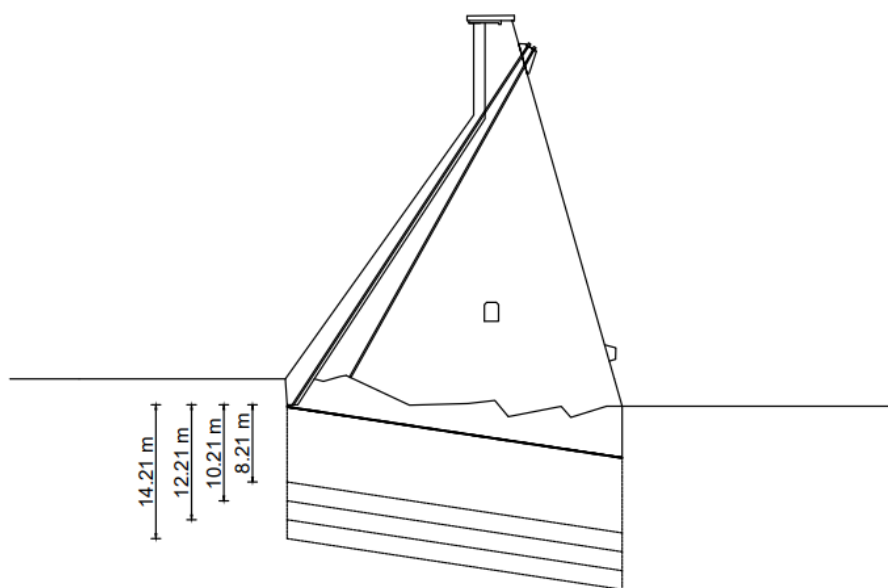


Figure 3.12: Deeper depth positions of the examined fracture sliding plane

The uplift distributions were extracted by using paths in the numerical model while safety factors were calculated for all the fracture depths.

### 3.7 Influence of the fracture friction angle

Different values of the friction angle of the fracture were used, in order to determine the behaviour and the effect of this parameter in the calculated safety factor. Accordingly it was used the most calibrated model and the examined failure scenario that produced the lowest safety factors in the standard sliding analysis mentioned in Section 3.5.

# Chapter 4

## Numerical model

### 4.1 Geometry

The geometry of the model that is used in this project was initially created by a previous study (Broberg et al., 2020). This model was developed to perform thermo- and mechanical analyses including displacements and different types of stress analyses. The monolith was designed in MicroStation as a 3D object and later imported to the finite element program Brigade Plus (Broberg et al., 2020). The model was later modified and further imported to the finite element program Abaqus in order to perform pore pressure analyses by Malm (2021).

The final model has a total length of 150 m in the upstream-downstream direction and the depth of the foundation have been chosen to 40 m with a thickness of 8 m according to Malm (2021). The dam model with the grout curtain and the rock fractures, is presented in Figure 4.1.

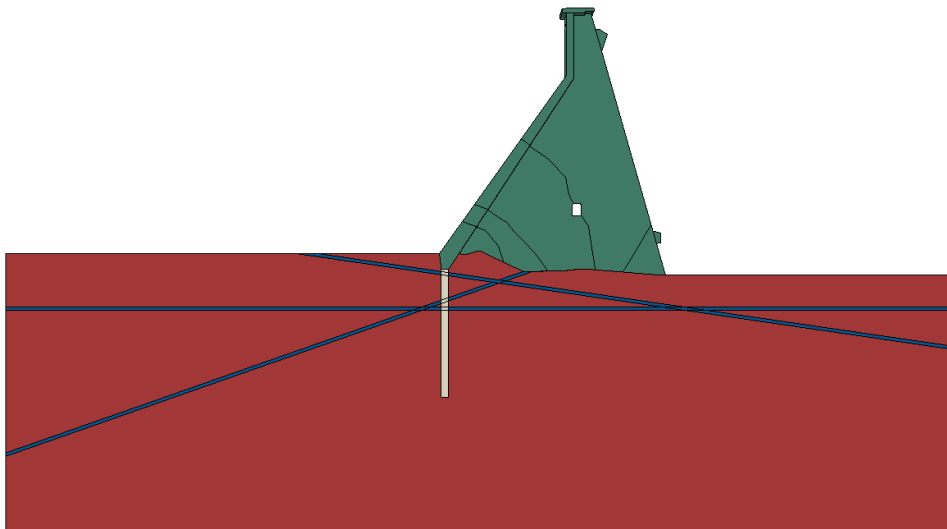


Figure 4.1: Model illustration with the grout curtain (gray) and the rock fractures (blue)

## 4.2 Rock fractures

The rock fractures properties that are included in the FE models are described in Section 3.3. The fracture areas have been defined as weak zones throughout the whole rock foundation. They are considered as homogeneous continuum zones with higher hydraulic conductivity than the surrounding rock.

Finally, the three most unfavorable rock fractures which could cause potential failure have been included in this project according to section 3.4. The fractures have been smeared in the numerical model, where each fracture zone has a height of 0.5 m which corresponds to one element length.

## 4.3 Grout curtain

Information regarding the actual depth and placement of the grout curtain is missing. The available construction drawings only indicate the minimum depth and thus, some assumptions about the depth and placement of the grout curtain had to be made in order to include the effect of the grout curtain in the analyses.

The grout curtain has been assumed to have a depth of 20 m (Broberg et al., 2020), which is equivalent to half the height of the monolith. The width of the grout curtain is assumed to be 1.12 m which is the same size as the horizontal width of the front plate embedded in the rock foundation and its length is equal to 8 m. The grout curtain is defined as a homogeneous continuum zone with lower permeability than the surrounding rock foundation.

## 4.4 Drainage system

The drainage holes are included in the model as a physical hole with a diameter of 80 mm and their depth is equal to 20 m. As mentioned in Section 3.2, three drainage holes have been installed in between each monolith. In this project, only one monolith is analyzed, thus the drainage holes that are closer to the examined monolith 42 are included. Therefore, only two drainage holes have been included in each side of the monolith. Illustration of the drainage holes relative the rest of the model can be seen in the following Figure 4.2.

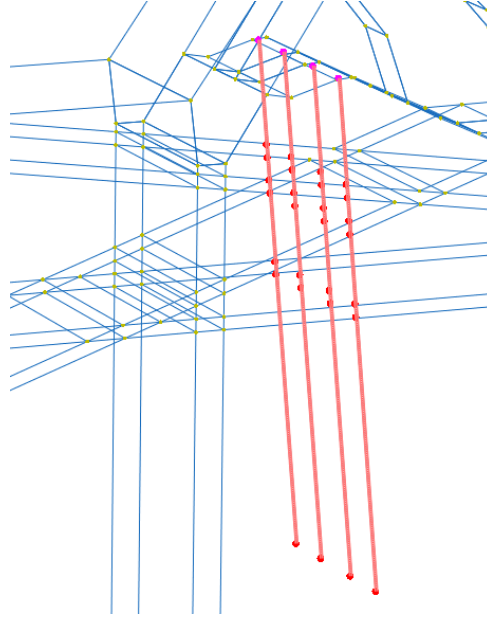


Figure 4.2: Drainage holes side and 3D view

## 4.5 Material properties

For the simulation of the pore water pressure, a linear elastic material behavior has been assumed for the monolith and the underlying rock foundation. A schematic illustration of the material properties for mechanical and pore pressure analyses is presented in Figure 4.3. This figure shows, the required material properties for both the dam and foundation as well as the interface between the foundation and the dam.

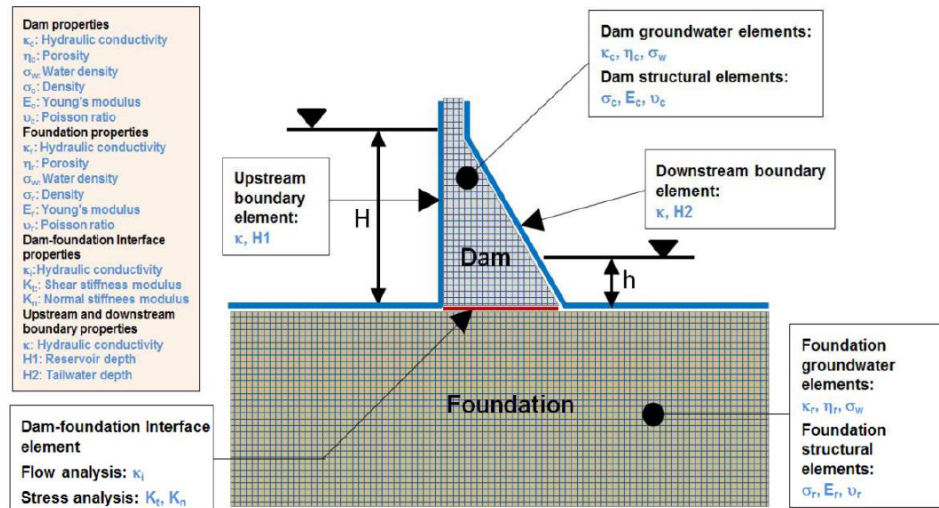


Figure 4.3: Illustration of pore pressure model and required material properties, from (McKay and Lopez, 2013)

The assumed material properties for monolith 42 in the buttress dam Storfinnforsen are summarized in Table 4.1. These material properties given in Table 4.1 are entirely taken from Malm (2021) and were originally based on field measurements performed at the dam.

Table 4.1: Applied material properties of the FEM model from Malm (2021)

	Concrete	Rock	Fractures	Grout curtain	
				Intact	Leached
Density [kg/m <sup>3</sup> ]	2300	2600	2600	2300	2300
Elastic modulus [GPa]	30	20	-	-	-
Poissons ratio	0.20	0.20	-	0.20	0.20
Hydraulic conductivity [m/s]	10 <sup>-11</sup>	10 <sup>-7</sup>	10 <sup>-5</sup>	10 <sup>-8</sup>	10 <sup>-7</sup>
Weight of the fluid [N/m <sup>3</sup> ]	9820	9820	9820	9820	9820
Void ratio	0.5	0.5	0.5	0.5	0.5
Initial saturation	1	1	1	1	1

## 4.6 Mesh discretization

The monolith model consists of about 150k elements with an element length of 0.25 and the element type is chosen as 3D linear hexahedral solid element, denoted as C3D8P in the Abaqus software.

The included rock foundation in this model was divided into two subareas. The part directly connected to the monolith has been defined with a denser mesh and consists of approximately 450k elements in total with a typical length of 0.25 m while the rest of the rock foundation was defined with an element length of 6.00 m. The different mesh sizes in the rock foundation were a necessity in order to obtain accurate numerical results in the areas of interest and at the same time avoid long computational time. The element type used in the rock foundation are 3D linear wedge solid elements, denoted as C3D6P in the Abaqus software.

For different models the exact number of the elements varies. For example, the models with drainage have more elements than those without. A principal illustration of the mesh of one of the models is shown in the Figure 4.4.

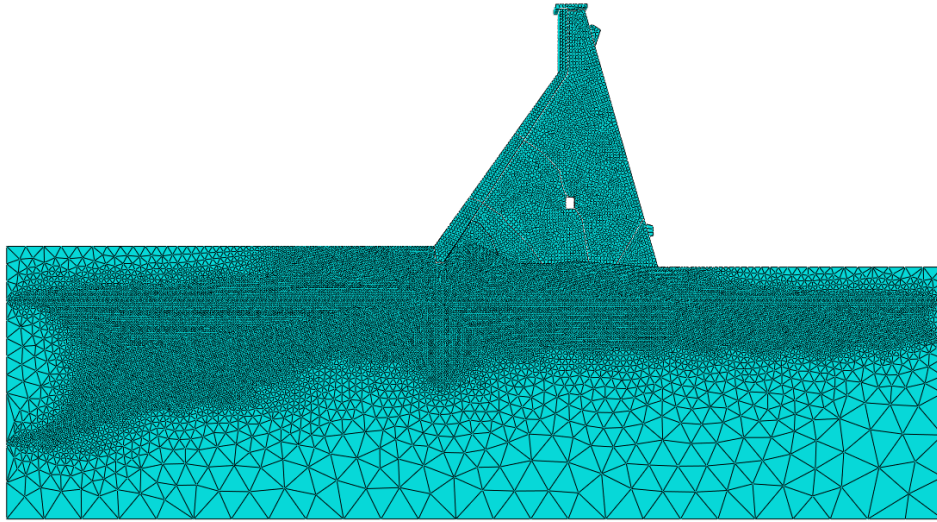


Figure 4.4: Illustration of the final mesh of the dam model with grout curtain, rock fractures and drainage holes

## 4.7 Initial conditions

Both the rock foundation and dam structure are defined with an initial saturation of 1.0 and a void ratio of 0.50 (Malm, 2021). The initial saturation of 1.0 allows to obtain a fully saturated flow in the analysis.

## 4.8 Boundary conditions

In order to simulate the real situation of the hydraulic load conditions, two cases of pore pressure boundary conditions were required for the analyses. The first was related to the normal reservoir level, i.e. the varying pore water pressure applied at the front plate of the dam and on the top of the rock foundation. The second case was related to the fact that no tailwater exists at the downstream side of the monolith, thus zero pressure is applied. An analytical field was created for the varying hydraulic load of the upstream surfaces according to Equation 2.3 in Section 2.2.

The load area of the upstream surfaces are depicted in Figure 4.5.

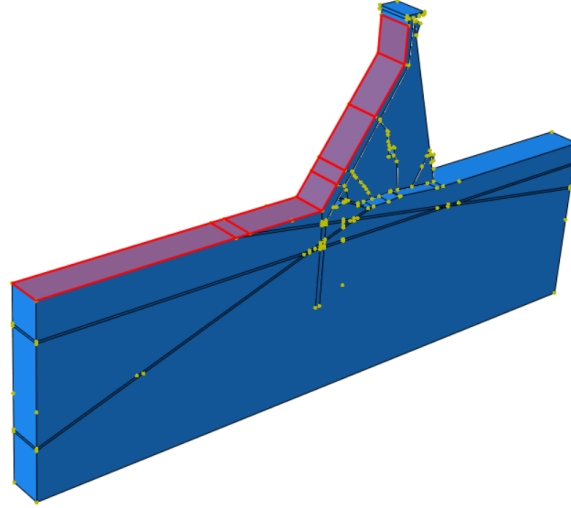


Figure 4.5: Load area of the variable water pressure on the upstream side

Regarding the boundary condition on the downstream side, the pressure load was predefined equal to zero at the areas shown in Figure 4.6.

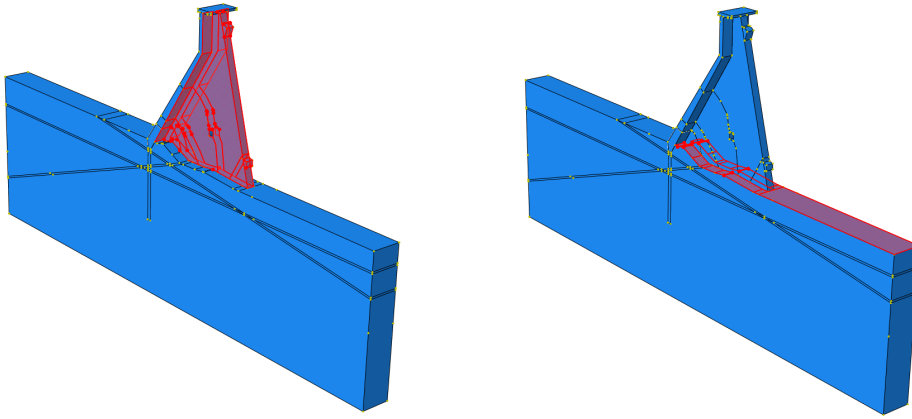


Figure 4.6: Load areas with zero water pressure on the downstream side

Furthermore, mechanical boundary conditions were applied in order to restricted displacements in the X,Y,Z directions and to avoid rigid body movements. Therefore all exterior surfaces of the rock foundation have been restrained except of the top surface of the rock.

## 4.9 Applied loads

The analyses intend to determine the uplift forces, hence mechanical loads were not considered. The only applied load in the numerical model is the gravity load which is applied at the whole model and allows to obtain the total pore water pressure (Malm, 2021). Instead, if the excess pore water pressure was to be obtained, the body force of each load component should be defined and the water density would be subtracked from the rock foundation density (ABAQUS, 2014). The gravity load is automatically calculated by the program based on the volume of each component, the material density, the saturation conditions and the weight of the wetting fluid. A gravitational constant of  $9.82 \text{ m/s}^2$  was specified in the program.



## 4.10 Analysis procedure

All the numerical analyses were performed with a Soil step in the FEM software. The program also automatically defines an initial step where all the mechanical boundary conditions are prescribed. The soil step is based on steady state conditions where the steady state conditions define that sufficient time has passed to ensure that long-term equilibrium distribution is obtained.

Furthermore, although a combined analysis of the pore pressure and mechanical loads is performed, only the pore pressure is evaluated in this study. Therefore, mechanical analysis results such as stresses and displacements are not assessed.

## 4.11 Evaluation of the pore pressure at the position of the sensors

The pore pressure results are extracted from the FE model using unique nodal points in the model. There are no nodes that coincide to the location of the installed pore pressure sensors, thus the nodes closest to sensors is chosen in order to extract the results. The numerical model has different mesh size and different node numbers depending on the inclusion (or not) of the drainage holes. Consequently, for models with drainage the selected node was 13 cm close to the real position of the sensors and for those without drainage it was 19 cm.

Moreover, the measured pore pressure is expressed in meters above sea level (m.a.s.l.) and thus, the pore pressure results from the FE program had to be converted to meter above the sea level. The coordinate system of the Abaqus software does not correspond to real coordinates and a factor of 230.8 had to be added to all the results in order to express the values in m.a.s.l, thus Equation 4.1.

$$h_w = \frac{P_w}{\rho_w \cdot g} + 230.8 \quad (4.1)$$

where,

- |          |   |
|----------|---|
| $h_w$    | is the pore pressure expressed in m.a.s.l, [m]                  |
| $P_w$    | is the resulting water pressure, [Pa]                           |
| $\rho_w$ | is the density of the water, [kg/m <sup>3</sup> ]               |
| $g$      | is the gravitational acceleration constant, [m/s <sup>2</sup> ] |

## 4.12 Investigated models

Multiple models have been created to study the effect of different parameters such as the influence of drainage system, the rock fractures, and the grout curtain. For each model, the pore pressure is extracted at the position of the pore pressure sensors. For all the models, the uplift distribution is also extracted along the horizontal rock fracture and finally, the obtained numerical results are compared with the corresponding measured pore pressure.

### 4.12.1 Models without drainage system

Four different models without drains have been analyzed. These four models include different combinations of the grout curtain and fractures in the foundation. This was a theoretical case in order to determine a global upper limit for the hydraulic head and simulate the clogged drains condition. The determined models are the following:

- **Model 1:** Homogeneous rock foundation without grout curtain
- **Model 2:** Fractured rock foundation without grout curtain
- **Model 3:** Homogeneous rock foundation with grout curtain
- **Model 4:** Fractured rock foundation with grout curtain

### 4.12.2 Influence of the drains

It is difficult to accurately simulate the real condition of the drains. Therefore, some simplified cases were chosen to investigate which should capture the upper and lower limits. These cases were defined with different levels of water fillings as listed below. Each water level condition was then combined with the four combinations given in Section 4.12.1.

The investigation was first started with two extreme conditions. A fully air-filled condition representing an entirely operational drainage system and a fully water-filled condition which represents a condition where the incoming water fills the drains before the water can flow out of the drains due to the goose-neck pipes at the drainage holes. These conditions should give the lower and upper limit of the pore pressure when the drains are in operation. Furthermore, two intermediate water filling levels were also tested to access the conditions in between.

- **Models a:** Fully air-filled drains
- **Models b:** Fully water-filled drains
- **Models c:** Half water-filled drains
- **Models d:** 2/3 water-filled drains

### 4.12.3 Variation of the hydraulic conductivity

Due to the fact that there are uncertainties related to the fracture hydraulic conductivity, a sensitivity analysis was conducted in order to validate and clarify them. Additionally, the sensitivity analysis was also performed to evaluate the effect of fracture hydraulic conductivity values on the pore pressure and the uplift distribution.

The model that was used, was the one that corresponded closer to the measured pore pressure and the field conditions according to the Section 4.12.2.

The hydraulic conductivity values were applied as constant along the length of every fracture and were varying between  $K=10^{-3}$  m/s and  $K=10^{-6}$  m/s. Too high or too small values were excluded as unrealistic scenarios.

### 4.12.4 Alternative models for the hydraulic conductivity

The purpose of this investigation was to examine different approaches regarding the fracture hydraulic conductivity and their influence on the pore pressure distribution. This was also a calibration process to determine which alternative model corresponded closer to the measured pore pressure. Thus, the following investigations were performed for:

- Fractures with tapered aperture
- Different constant hydraulic conductivity in each fracture

**Fractures with tapered aperture** are simulated with a varying hydraulic conductivity along their length. Instead of using a constant hydraulic conductivity in all the fractures, they were simulated as tubes where their hydraulic conductivity could increase or decrease gradually. Due to the fact that the hydraulic conductivity is a product of the aperture size, the tapered tube simulation could be achieved by defining different hydraulic conductivity values along their length.

The values that were applied are the following:

- Low hydraulic conductivity  $\rightarrow K=10^{-6}$  m/s
- Medium hydraulic conductivity  $\rightarrow K=10^{-5}$  m/s
- High hydraulic conductivity  $\rightarrow K=10^{-4}$  m/s

The model that was used, was the one that corresponded closer to the measured pore pressure and the field conditions according to the Section 4.12.2. Two alternative models were determined with tapered aperture size:

- **Model alt.1F** with gradually increasing hydraulic conductivity

- **Model alt.2F** with gradually decreasing hydraulic conductivity

The two alternative hydraulic conductivity conditions could be simplified according to the Figures 4.7 and 4.8.

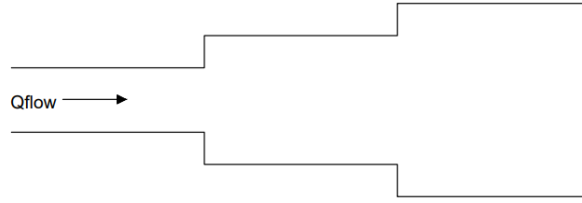


Figure 4.7: Simplified illustration of Alt. 1F fracture condition

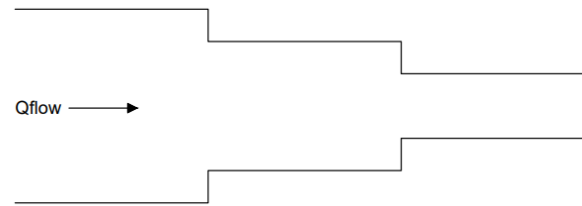


Figure 4.8: Simplified illustration of Alt. 2F fracture condition

**Constant hydraulic conductivity in each fracture** was defined with different constant values in each fracture individually. The applied values were close to the measured ones and varying between  $K=10^{-4}$  m/s and  $K=10^{-6}$  m/s. Two more alternative combinations were created according to Figures 4.9 and 4.10.

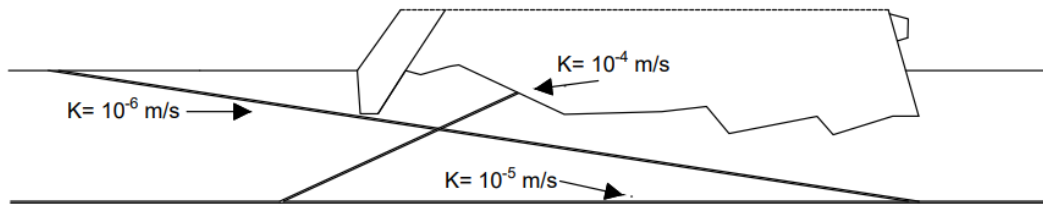


Figure 4.9: Alt. 3F illustration with the applied hydraulic conductivity value in each fracture

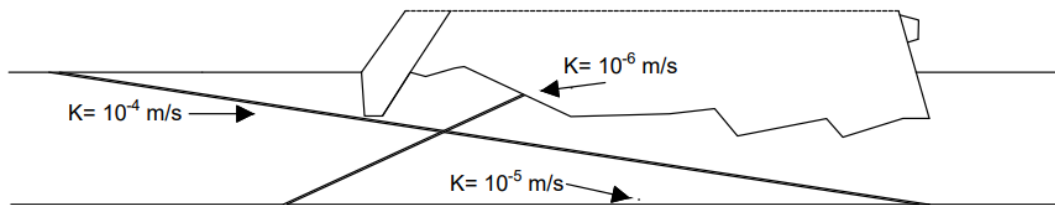


Figure 4.10: Alt. 4F illustration with the applied hydraulic conductivity value in each fracture

The model that was used, was the one that corresponded closer to the measured pore pressure and the field conditions according to the Section 4.12.2. Therefore, two additional alternative models were defined:

- **Model alt.3F** corresponding to the fracture hydraulic conductivity combination in Figure 4.9
- **Model alt.4F** corresponding to the fracture hydraulic conductivity combination in Figure 4.10

#### 4.12.5 Alternative models for the grout curtain

The purpose of this investigation was to determine which grout curtain parameters influence more the pore pressure distribution. The uncertainties related to the grout curtain were focused on the following:

- the deterioration of the grout curtain due to continuous loading and environmental conditions where this effect was simulated by defining a reduced grout curtain hydraulic conductivity or by considering that the fractures bypassed the grout curtain, thus were allowed to surpass it.
- the depth of the grout curtain where a long grout curtain could have a depth of  $L=20.00$  m and a short grout curtain a reduced depth of  $L=6.32$  m.

In order to simulate the models that considered a bypassed grout curtain, a cracked grout curtain is simulated by allowing the rock fractures to extend through the grout curtain as represented in Figure 4.11.

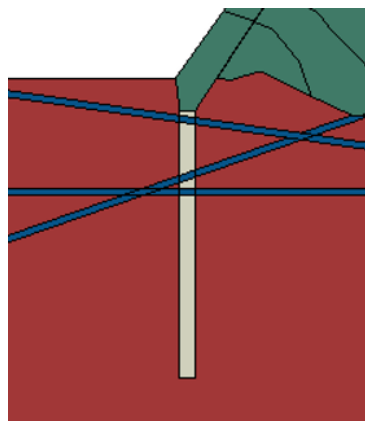


Figure 4.11: Illustration of the bypassed long curtain in the FE model

Furthermore, the models with a short grout curtain were simulated as presented in the following Figure 4.12.

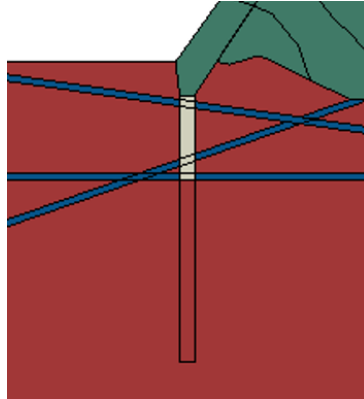


Figure 4.12: Illustration of the short grout curtain in the FE model

The model that was used, was the one that corresponded closer to the measured pore pressure and the field conditions according to the Sections 4.12.2 to 4.12.4. Accordingly, the alternative models that were examined in order to determine the influence of the grout curtain were the following:

- **Model alt.1G** with an intact short grout curtain.
- **Model alt.2G** with a leached long grout curtain where the grout curtain hydraulic conductivity was reduced to  $K = 10^{-7}$  m/s.
- **Model alt.3G** with a bypassed long grout curtain.

# Chapter 5

## Pore pressure analyses

Multiple models with a number of different assumptions and combinations have been investigated including:

- The existence of rock fractures in the foundation
- The effect of grout curtain with a variation of both depth and material properties
- The influence of drains with variation of the water filling levels
- And further investigation related to the rock fracture properties such as hydraulic conductivity and variation of aperture size

The results from the numerical models are compared with the measured values from the pore pressure sensors installed at monolith M42 in Storfinnforsen concrete buttress dam.

### 5.1 Models without drainage

In this section, models that do not include drains are presented. This corresponds to a scenario where drains are clogged or a past state before drains were installed on the dam.

#### 5.1.1 Model 1 - Homogeneous rock foundation

In the first model, a homogeneous rock foundation was considered without any influence from drains or grout curtains. Model 1 corresponds to a case where no precautions have been taken to reduce the pore pressure below the dam. The resulting pore pressure distribution from Model 1 is shown in Figure 5.1.

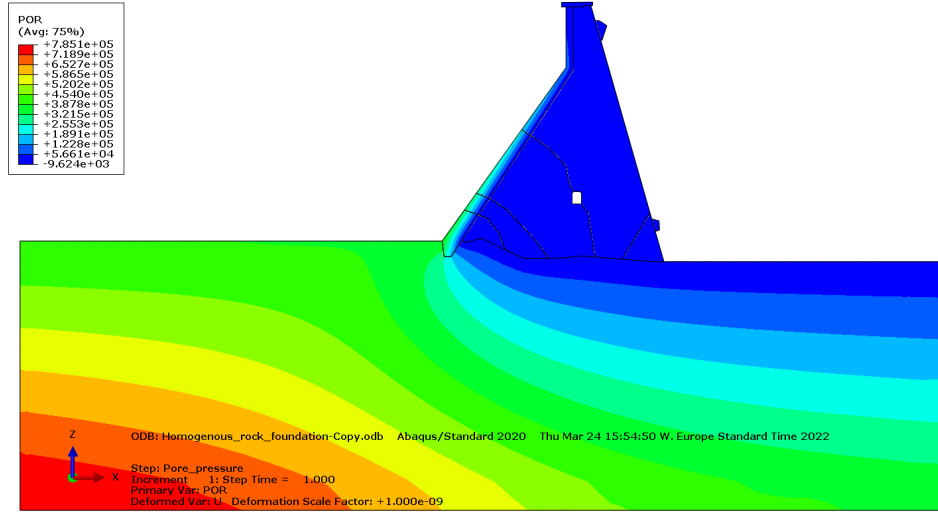


Figure 5.1: Distribution of pore pressure in Model 1 with homogeneous rock but without grout curtain and fractures

### 5.1.2 Model 2 - Influence of rock fractures

In the second model, rock fractures were considered in the foundation beneath the dam. The rock fractures were defined with higher hydraulic conductivity as described in Section 4.5, which resulted to a higher pore pressure underneath the dam. The distribution of the resulting pore pressure can be seen in Figure 5.2.

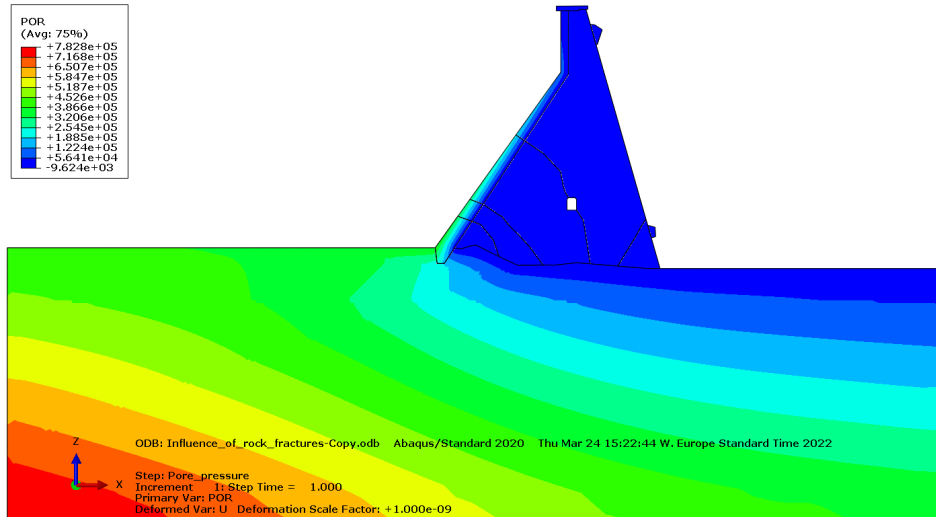


Figure 5.2: Distribution of pore pressure in Model 2 with rock fractures and no grout curtain

### 5.1.3 Model 3 - Influence of grout curtain

In the third model, the rock foundation was considered to be homogeneous with a grout curtain but no drains. The distribution of the pore pressure from Model 3 is presented in Figure 5.3. The grout curtain, as shown in the figure, reduces the pore pressure underneath the dam.



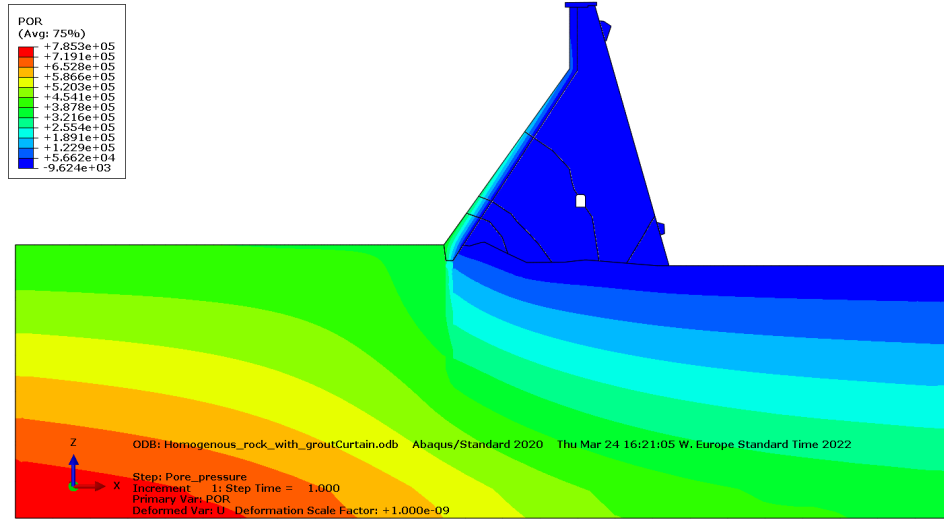


Figure 5.3: Distribution of pore pressure in Model 3 with homogeneous rock and grout curtain

#### 5.1.4 Model 4 - Combination of grout curtain and rock fractures

In the fourth model, a fractured rock foundation and grout curtain is considered. The grout curtain is considered as fully functional and intact, which prevents water transportation through the rock fractures. Distribution of the pore pressure from Model 4 is illustrated in Figure 5.4. As shown in the figure legend, this case shows quite significant decrease in the pore pressure below the dam compared to the other cases.

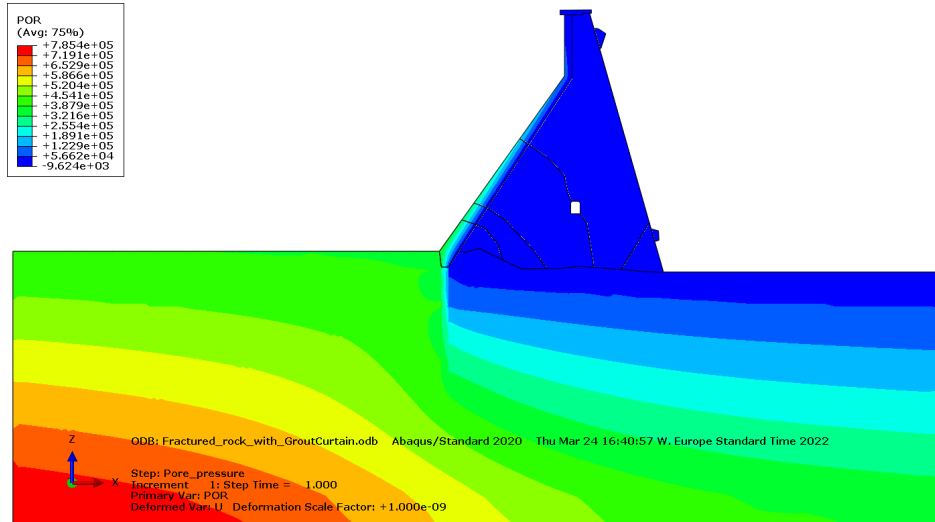


Figure 5.4: Distribution of pore pressure in Model 4 with rock fractures and grout curtain

The grout curtain intersects the rock fractures which results in an increased pore pressure on the upstream side of the dam and decreased pore pressure on the downstream side of the dam. The fractures distribute the pore pressure and when the grout curtain intersect this distribution, it results that the pore pressure on each side averages out. This has a huge impact on the pore pressure at the location of the pore pressure sensors. This effect can be clearly seen in the contour plots in Model 4 compared with Model 3 (without rock fracture in the foundation).

## 5.2 Influence of the drains

The influence and functionality of the drains has been evaluated in this section. Different boundary conditions regarding the different stages of possible water filling states have been investigated in order to capture the effect of the drain in different stages of water filling. The intention is to capture the limiting pore pressure values in comparison with the measured pore pressure provided that there is an existing drainage.

- **Condition a** – Drains are considered to be empty filled with air
- **Condition b** – Drains are considered to be fully filled with water
- **Condition c** – Drains are considered to be half filled with water
- **Condition d** – Drains are considered to be 2/3 filled with water

The pressure distribution along the length of the drains for each condition is represented in Figure 5.5.

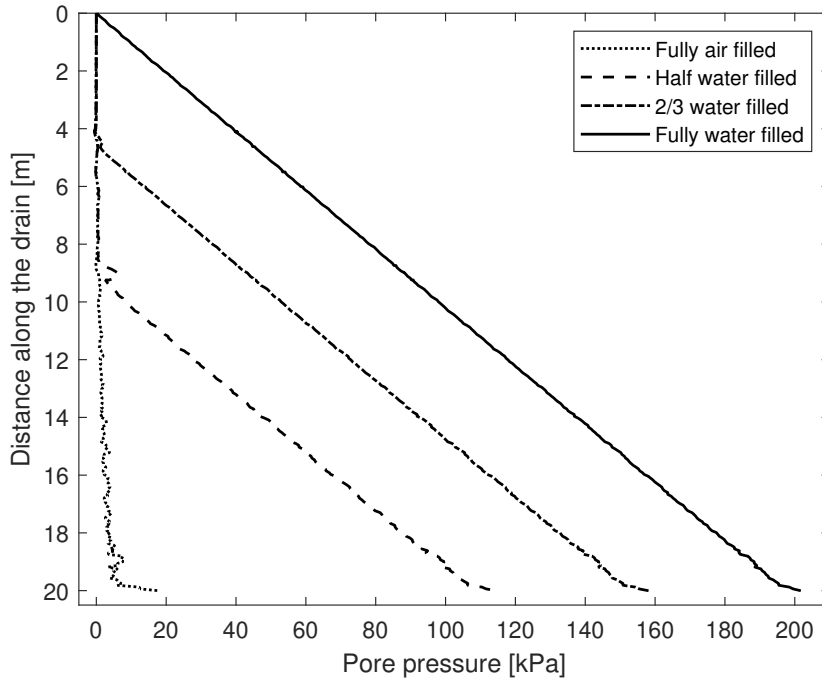


Figure 5.5: Pore pressure distribution along the length of the drains for each condition

### 5.2.1 Drainage system fully filled with air

This condition corresponds to a fully functional drainage system where the water is continuously pumped out of the drains. Drains were defined with zero pore pressure which greatly decreases the pore pressure distribution below the dam. Illustration of this decrease can be observed in the contour plots in Figure 5.6 until Figure 5.9.

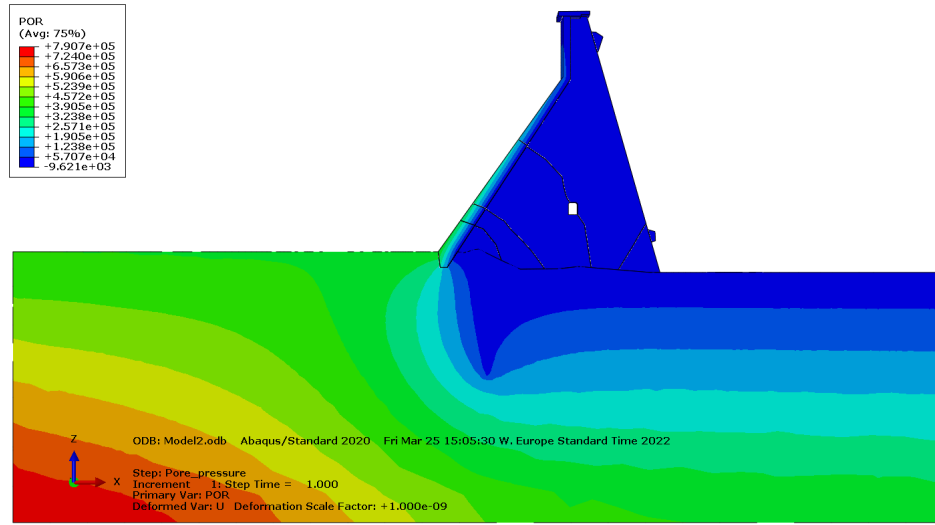


Figure 5.6: Distribution of pore pressure in Model 1a with homogeneous rock, fully operational drains but without grout curtain

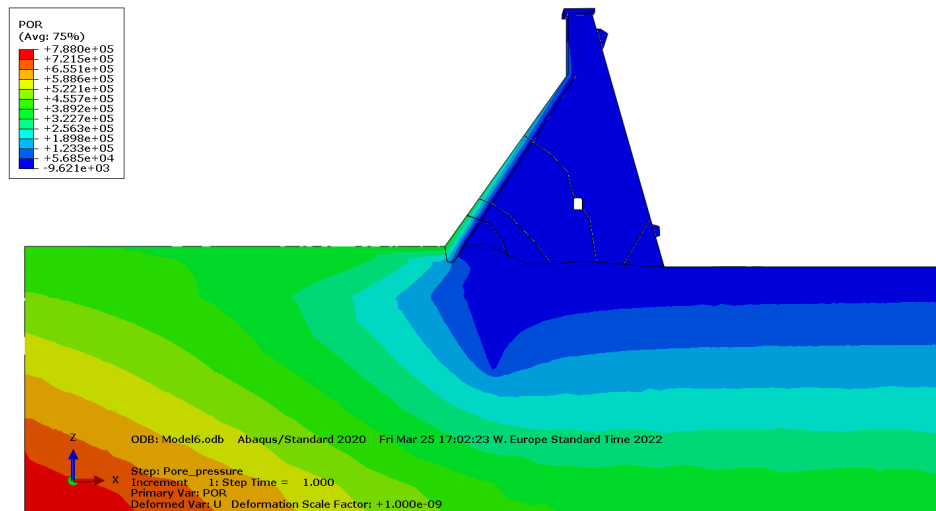


Figure 5.7: Distribution of pore pressure in Model 2a with fractured rock, fully operational drains but without grout curtain

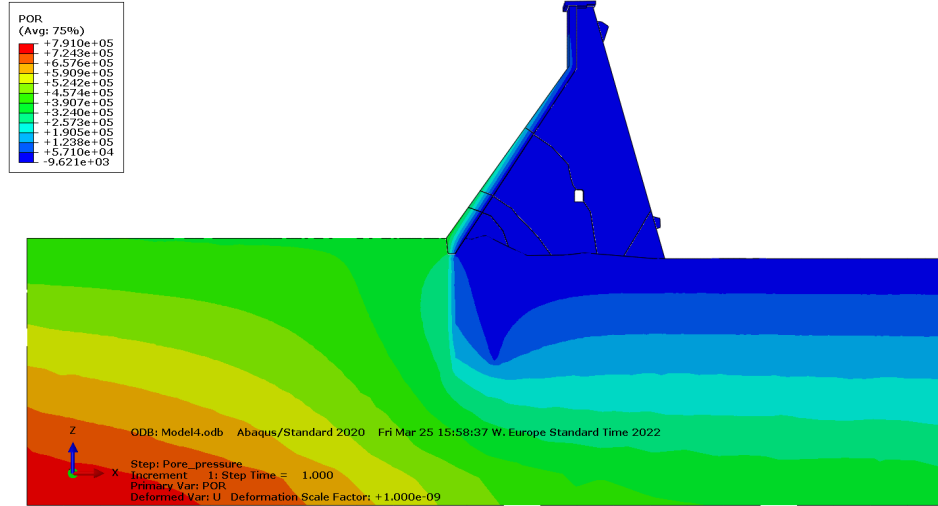


Figure 5.8: Distribution of pore pressure in Model 3a with homogeneous, fully operational drains and grout curtain

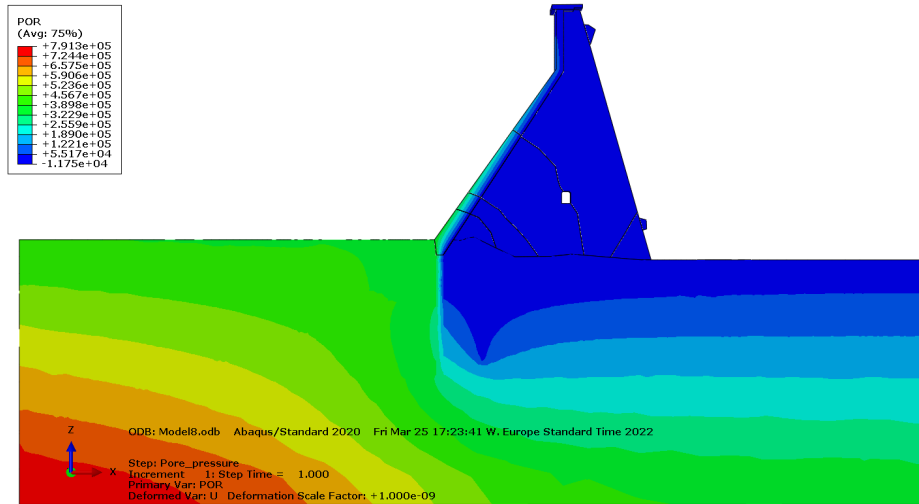


Figure 5.9: Distribution of pore pressure in Model 4a with fractured rock, fully operational drains and grout curtain

## 5.2.2 Drainage fully filled with water

In this section, the drains are assumed to be fully water filled and the intention is to assume a conservative scenario where the water flows out of goose necks. As a general rule, approaching water can fill the drains until overabundance water is vanished because of the gooseneck pipes at the openings of the drainage holes. Results from analyzed cases is presented in Figure 5.10 to Figure 5.13

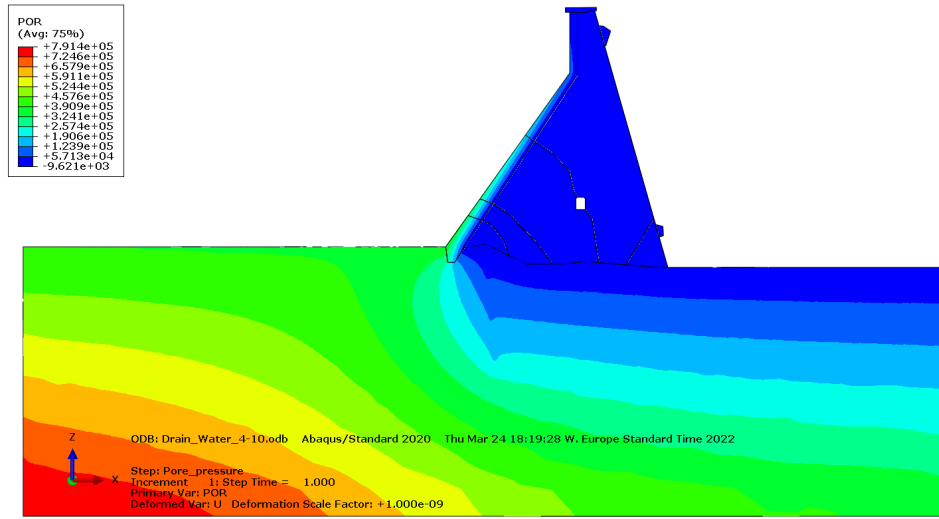


Figure 5.10: Distribution of pore pressure in Model 1b with homogeneous rock, drains but no grout curtain

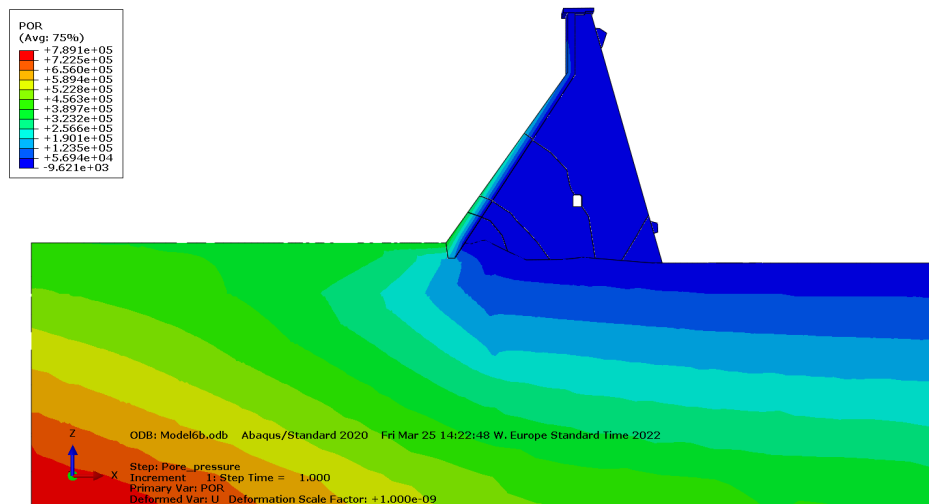


Figure 5.11: Distribution of pore pressure in Model 2b with fractured rock, drains but without grout curtain

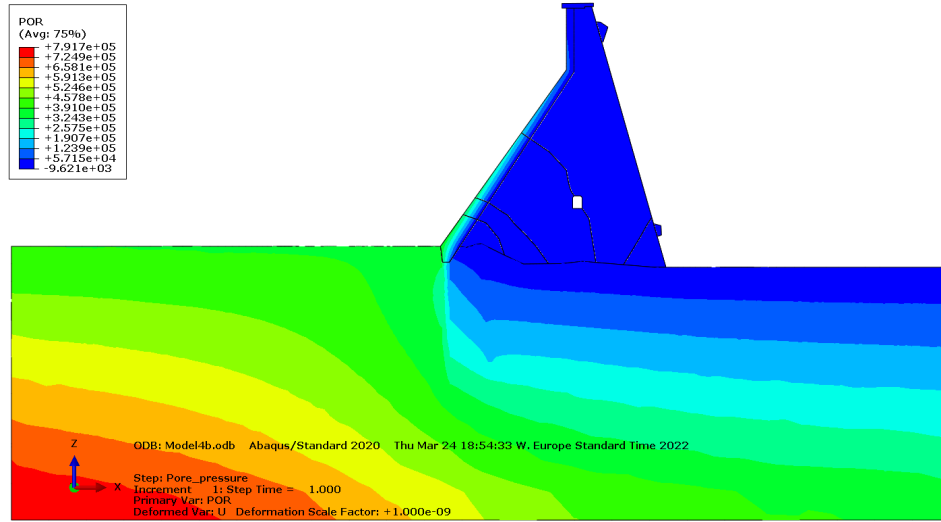


Figure 5.12: Distribution of pore pressure in Model 3b with homogeneous rock, drains and with grout curtain

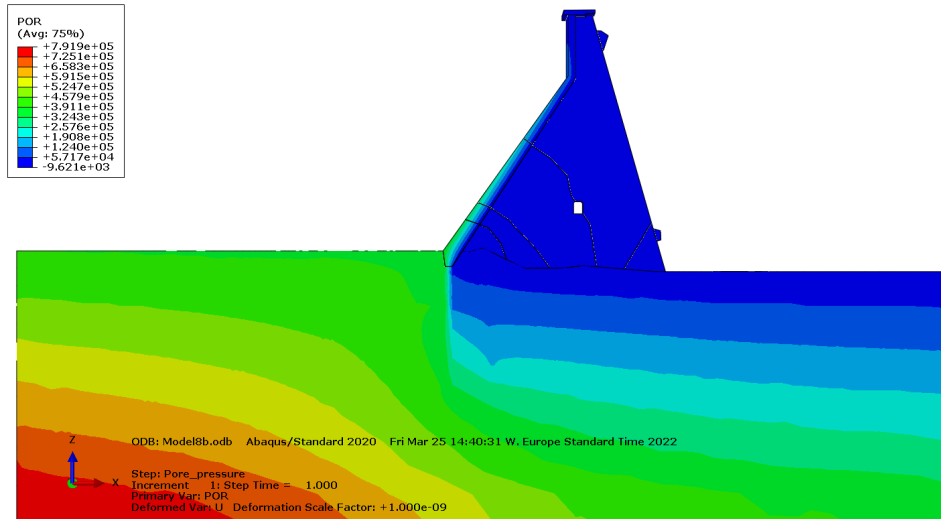


Figure 5.13: Distribution of pore pressure in Model 4b with fractured rock, drains and grout curtain

### 5.2.3 Additional filling conditions

In order to investigate further different possible states regarding the water level inside the drains and the influence of these states in the uplift pressure distribution below the dam, two more water filling conditions have been studied.

- **Condition c** – Drains are considered to be half filled with water
- **Condition d** – Drains are considered to be 2/3 filled with water

The resulting contour plots of the numerical analysis regarding these two model categories have been summarized in Appendix A.

### 5.3 Result summary of the investigated cases

Results from the previous described models are summarized in this section. The obtained numerical pore pressure at the location of the pore pressure sensors is compared with the field measured value which is equal to  $h_w = 235.1$  m. Additionally, the uplift pressure along the horizontal joints shown in Figure 5.19 for all the models is presented in this section in order to better understand the uplift pressure distribution.

#### 5.3.1 Comparison of pore pressure results

The evaluated numerical pore pressure at the position of the pore pressure sensor is displayed for the models without drainage system in Figure 5.14. In Figure 5.14, the measured pore pressure from the field sensors is included in order to compare it with the numerically obtained ones.

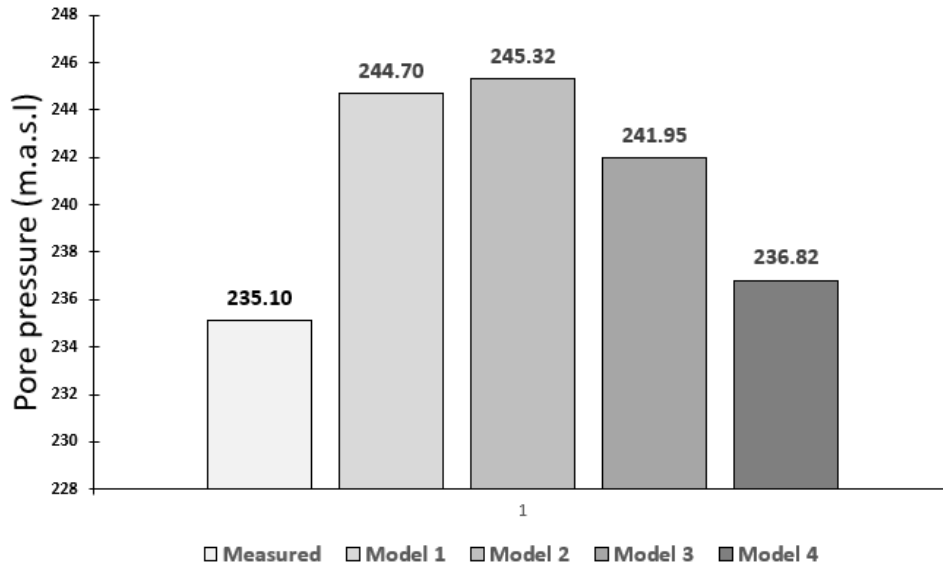


Figure 5.14: Pore pressure results at the location of the pore pressure sensors for the models without drains

Based on the results in Figure 5.14, Model 4 seems to have the closest pore pressure to the measured value. The pore pressure at the position of the pore pressure sensors is 1.72 m higher than the measured value. All the other cases overestimate the pore pressure water head significantly. Another noticed aspect is the influence of the grout curtain. By comparing Models 1 and Model 3, it can be understood that the grout curtain has a rather small effect on the hydraulic water head at the position of the pore pressure sensors when the rock foundation is considered intact. On the other hand by comparing the Models 2 and 4, the difference becomes much larger when the rock foundation is considered to be fractured.

All the models without drainage system, overestimate the pore pressure substantially, except Model 4 which include rock fractures and grout curtain). Therefore, it is a reasonable conclusion to assume that there is a drainage system in operation. Otherwise it would

be difficult to justify the difference between the numerical results and field measurement. For this reason, the drains were included and modelled also with different assumptions regarding the level of water fillings in the drainage holes.

Firstly, the drains were assumed to be empty, thus filled with air because the drains are fully operational. This analysis was deliberately performed in order to underestimate the pore pressure and obtain a lower limit of the pore pressure. The pore pressure results at the position of the pore pressure sensors are summarized in Figure 5.15. These models are combined in the same manner as previously but denoted with an a at the end.

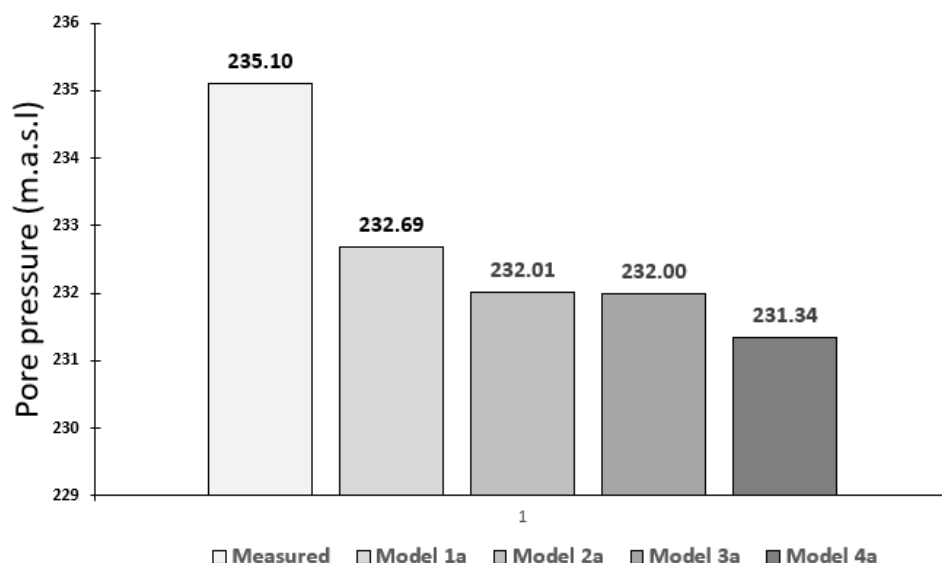


Figure 5.15: Pore pressure results at the location of the pore pressure sensors for the models with empty drains

Based on the results presented in Figure 5.15, it can be concluded that all the models that include empty drains (e.i. drains filled with air) underestimate the pore pressure as expected. The pore pressure in these models are underestimated approximately 3 to 4 m in hydraulic water head for all the models. In addition, it can be observed in the Figure that the effect of the grout curtain is rather small when the drain is in operation regardless of whether the rock foundation is intact or fractured, see Model 3a and Model 4a.

In reality, it is more accurate that the drains have at least some water filling. Therefore, additional analyses were conducted for the same models as before, but in this time the drains are fully filled with water instead. These models are denoted with b at the end. Figure 5.16 summarizes all the pore pressure results from Models b, that include water filled drains. These analyses were performed in order establish an upper limit of the pore pressure when the drains are in operation.



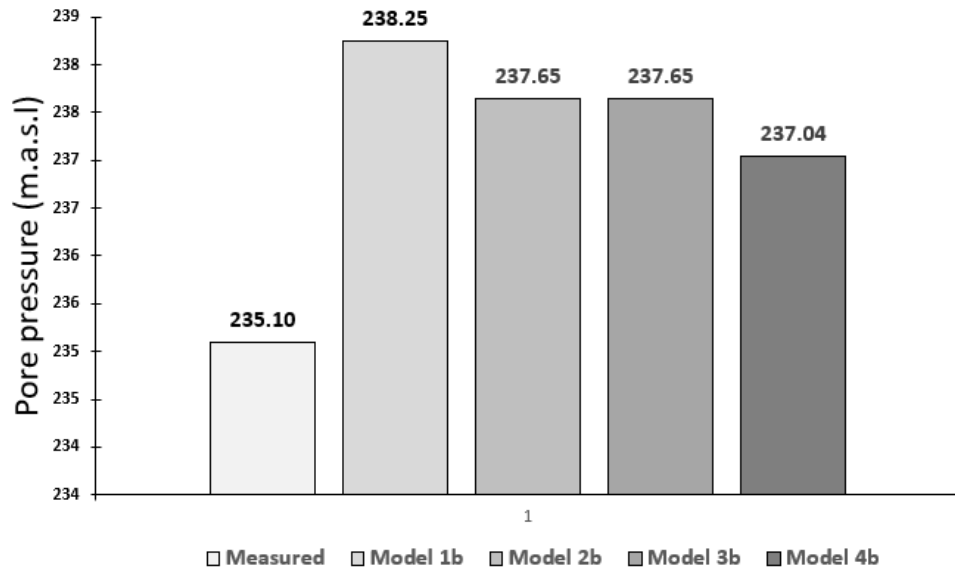


Figure 5.16: Pore pressure results at the location of the pore pressure sensors for models with water filled drains

Based on the results presented in Figure 5.16, it can be observed that all the analyses from these Models b overestimate the pore pressure at the location of the pore pressure sensors. These models overestimate the pore pressure approximately 1.94 to 3.15 m in hydraulic head which is not as large as in the cases without existing drainage system.

After the two previously extreme cases, it was reasonable to investigate models that are in between these two cases. Therefore, a third alternative was developed where the pore pressure is defined so only half of the drains are filled with water. These Models combined in the same manner as the previously cases and denoted with the letter c at the end.

The results from Models b are summarized in Figure 5.17. Obtained results show similar results as the models where the drains were assumed to be empty (e.i drains filled with air). The results underestimated with approximately 2.00 to 3.70 m pore pressure water head.

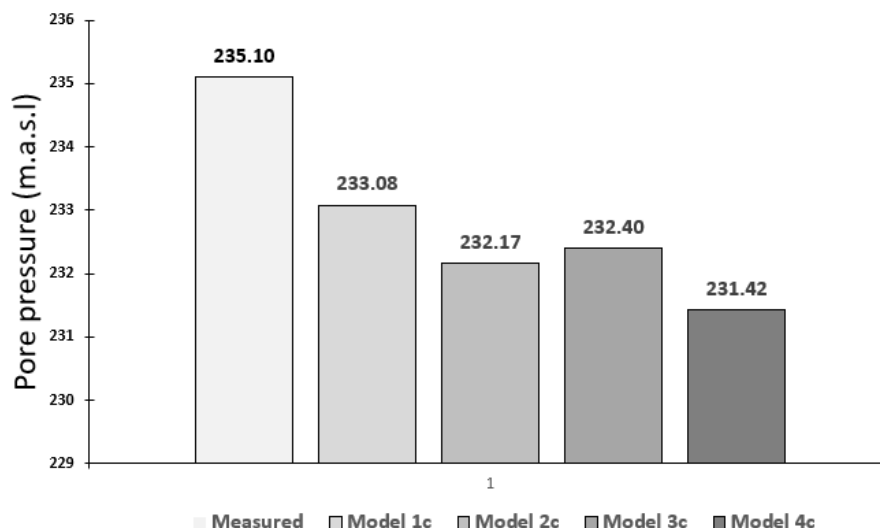


Figure 5.17: Pore pressure results at the location of the pore pressure sensors for models with half water filled drains

Lastly, another alternative with a 2/3 water filled drains were analyzed. Results from these models are presented in Figure 5.18. As observed in the Figure 5.18, obtained results are also similar to the models where the drains were assumed to be empty, but result are slightly closer to field measurements.

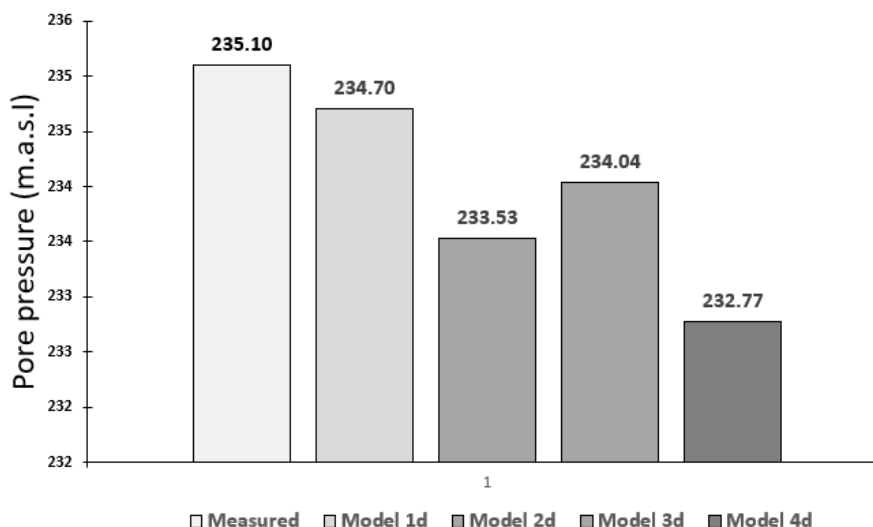


Figure 5.18: Pore pressure results at the location of the pore pressure sensors for models with 2/3 water filled drains

### 5.3.2 Uplift pressure distribution

In order to study how the safety factor more accurately, it is important to determine a more realistic pore pressure distribution, to further determine the corresponding uplift pressure that may occur in the rock fractures. Regarding field measurements, all the pore pressure sensors are installed approximately 4 m from the downstream side of the front-plate at a depth of around 6 m. regarding the field measurements three points are accessible for analyzing the pore pressure

1. Pore pressure at upstream side of the dam related to the full hydrostatic level of the reservoir
2. Pore pressure at downstream side of the dam related to the tail water (which, in this case is zero)
3. Pore pressure at the location of the pore pressure sensors (i.e. 4 m downstream side of the front plate at depth of around 6 m)

From the numerical models, the pore pressure can be evaluated at any arbitrary location in the rock foundation. In an attempt to evaluate the pore pressure distributions, the pore pressure is plotted along the horizontal fracture for the different models, see Figure 5.19. This fracture is located at 8.3 m below the surface at the upstream side of the dam and 5.41 at the downstream side.

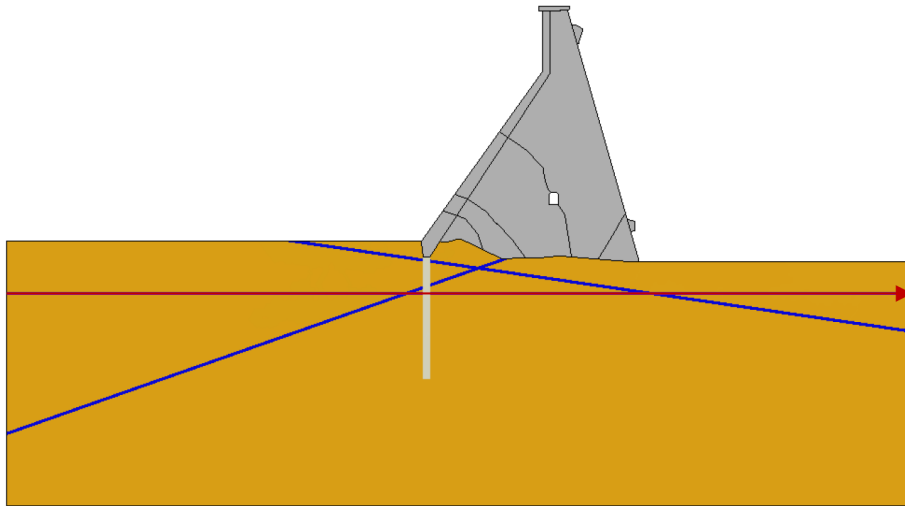


Figure 5.19: Illustration of the path used to plot the pore pressure distribution (Malm, 2021)

For all the models without drainage system, the variation in the pore pressure along the horizontal rock fracture is plotted in Figure 5.20 together with a vertical line representing the position of the grout curtain. In the plot, the effect of the rock fracture in the foundation can be observed by comparing Model 1 with Model 2. As mentioned previously, Model 2 with rock fracture averages the pore pressure along the whole length of the rock foundation. This results in lower pore pressure on the upstream side of the grout curtain and higher pore pressure on the downstream side. Furthermore, it can be observed in the graph that the grout curtain has a greater influence if the rock foundation is assumed to be fractured. This can be observed by comparing Model 3 and Model 4.

As mentioned previously, Model 2 averages the pore pressure along the length of the rock foundation due to the rock fractures existence. This results in lower pore pressure on the upstream side of the grout curtain and higher pore pressure on the downstream side. Furthermore, it can be observed in the graph that the grout curtain has a greater influence if the rock foundation is assumed to be fractured. This can be observed by comparing Model 3 and Model 4.

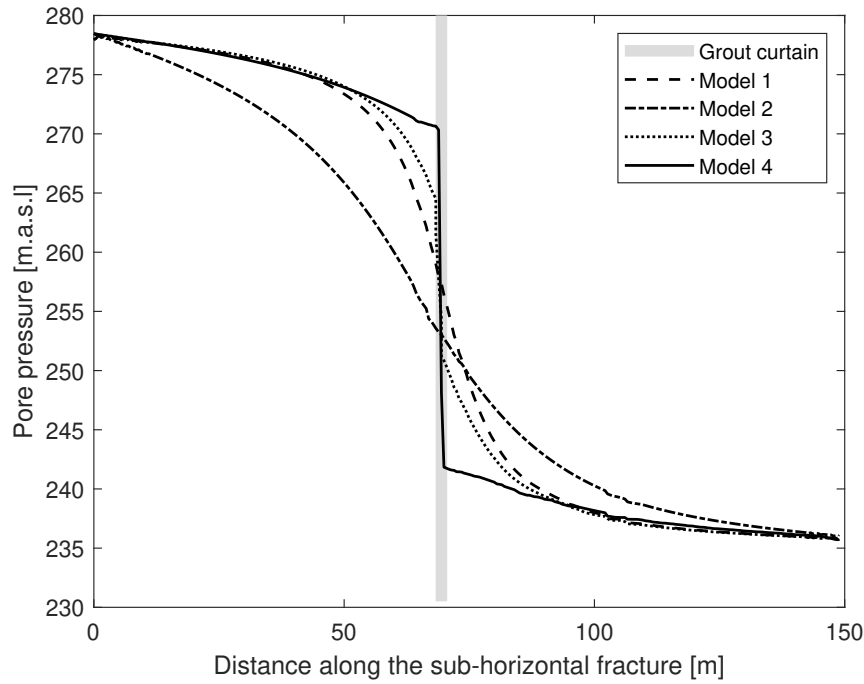


Figure 5.20: Pore pressure distribution along the horizontal rock fracture for the models without drains

Based on these results, it is possible to evaluate the efficiency of the grout curtain. The pore pressure reduction over the grout curtain is calculated with Equation 5.1 for Model 4 which includes rock fracture at the foundation and intact grout curtain.

$$Reduction_{fractured} = \frac{P_{US} - P_{DS}}{P_{Max} - P_{Min}} = \frac{270,78 - 241,14}{278,49 - 236,06} \approx 69\% \quad (5.1)$$

This means that the pore pressure is only 32% at the downstream side of the grout curtain compared to the pore pressure at the upstream side of the grout curtain. This results larger reduction than the pore pressure reduction that is defined in RIDAS, where a reduction 50% can be assumed.

It should be noted that the results above is based on a model with fractured rock foundation. For a model with intact rock foundation, this reduction is much smaller, see Equation 5.2 to observe the reduction Model 3.

$$Reduction_{intactrock} = \frac{P_{US} - P_{DS}}{P_{Max} - P_{Min}} = \frac{264,56 - 251,20}{278,49 - 236,06} \approx 31\% \quad (5.2)$$

This means that the pore pressure is 69% directly downstream side of the grout curtain compared to its upstream side. This shows that the grout curtain has larger effect if the rock foundation is fractured than the intact foundation. Notice, that the reduction proposed in RIDAS seems to be almost at the middle of the two reductions evaluated from these models.

In the following evaluations, the influence of drainage is introduced on the dam. The pore pressure distribution along the horizontal rock fracture is plotted in Figure 5.21, for all the models with empty drains (i.e. drains are filled with air). The distribution of pore pressure is shown in Figure 5.22, for the models with fully water filled drains.

By comparing Figures 5.21 and 5.22, it can be observed that water pressure in the drains has great effect on the pore pressure at the location of the drains. The models with empty drains, result in very low pore pressure at the location of the drains. The models with the water filled drains have pore pressure distribution similar to the model without any drains which were presented earlier.

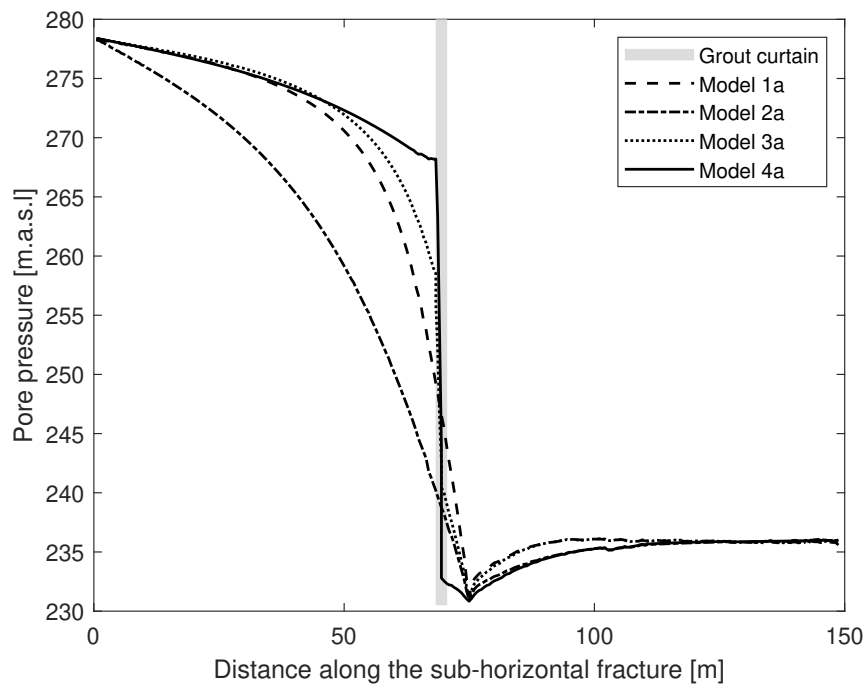


Figure 5.21: Pore pressure distribution along the horizontal rock fracture for the models with air-filled drains

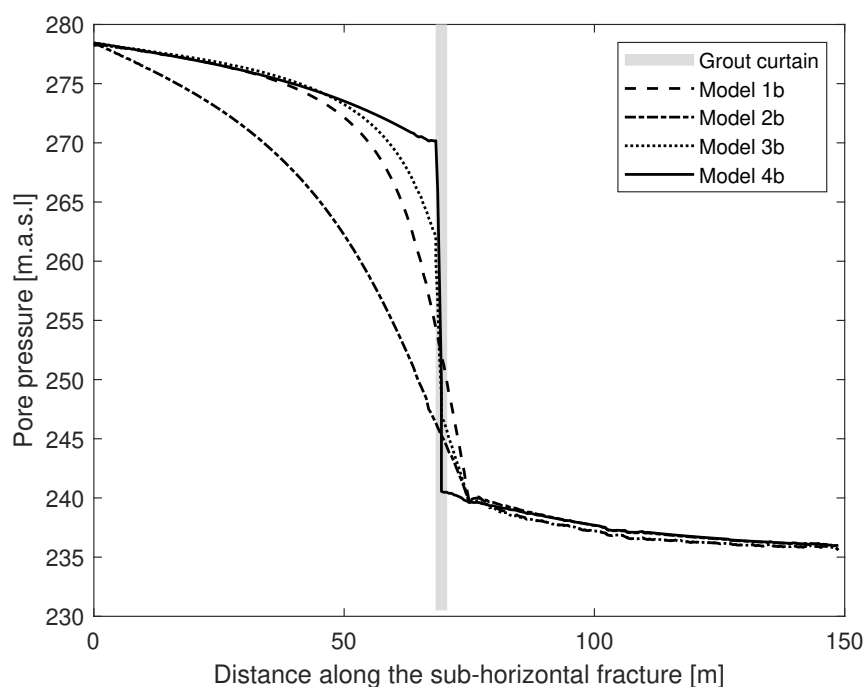


Figure 5.22: Pore pressure distribution along the horizontal rock fracture for the models with water-filled drains

Analyses were also performed for two intermediate cases. Figure 5.23, shows the pore pressure distribution for a case where the drains are half-filled with water while Figure 5.24, shows the pore pressure distribution for the last case where the drains was defined to be 2/3 filled with water. These cases show both similar results as the case with the empty drains.

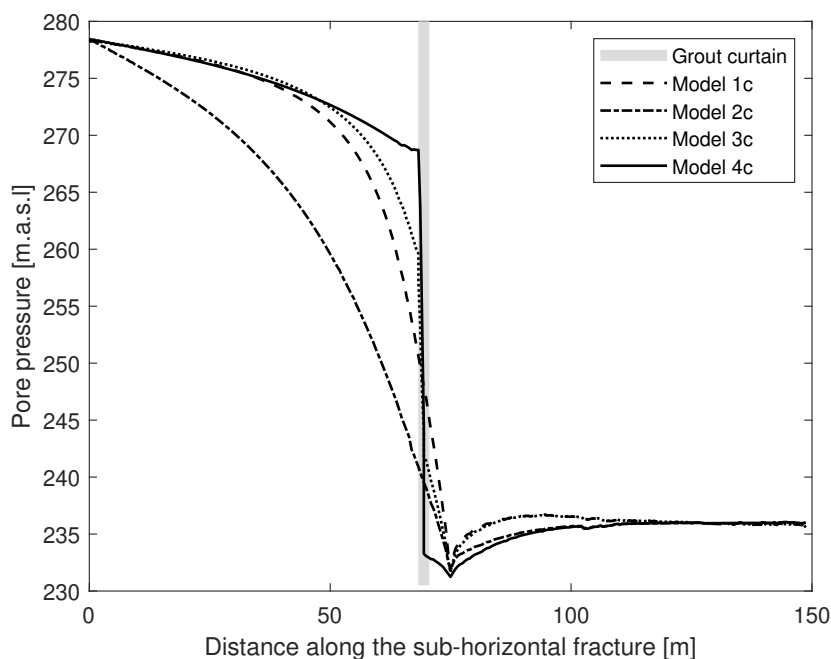


Figure 5.23: Pore pressure distribution along the horizontal rock fracture for the models with half water-filled drains

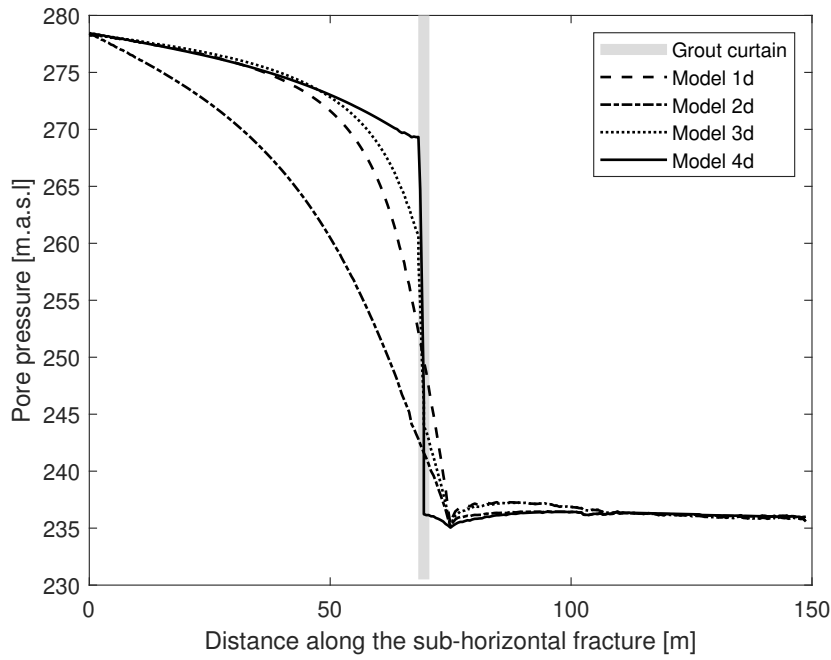


Figure 5.24: Pore pressure distribution along the horizontal rock fracture for the models with 2/3 water-filled drains

### 5.3.3 Comparison of analytical and numerical results

In this section, a relative comparison between numerical results and analytical curves given in RIDAS have been performed. The numerical uplift pressure is extracted in the rock fracture underneath the dam at the position of the grout curtain to the dam toe. All the figures in this section, have a lowest x-value (69.4 m) corresponding to the position of the grout curtain and largest x-value (105.6 m) which is the position of the downstream toe.

Figure 5.25, shows a linear curve from downstream water level to upstream water level which corresponds to the expected uplift pressure when there is no grout curtain or drains. The Figure 5.25, also shows the two corresponding numerical models without drains and grout curtain. Both models give significantly lower uplift pressure than the analytical curves. The maximum uplift pressure of these models is only about 50% to 60% of the expected analytical uplift pressure.

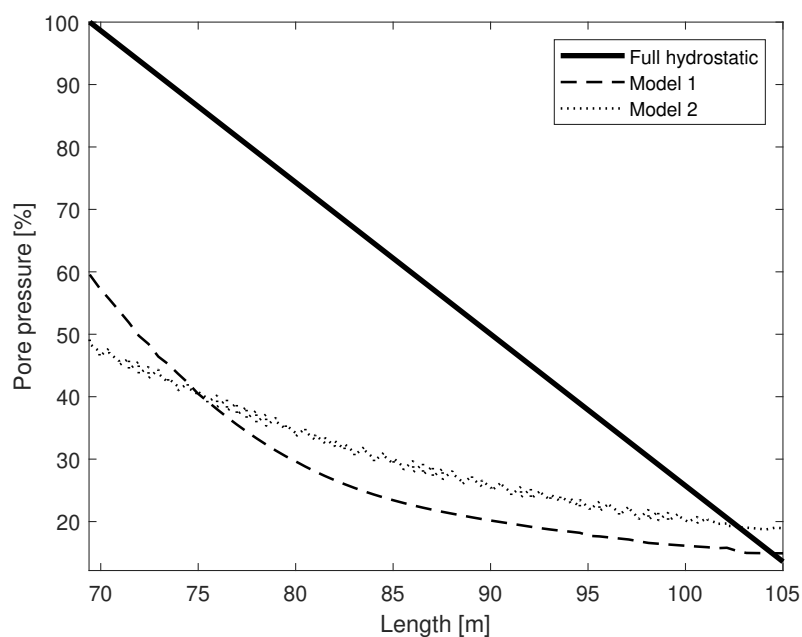


Figure 5.25: Evaluated uplift pressure below the dam for models without grout curtain which should be compared to the full hydrostatic uplift pressure

Figure 5.26, show a linear reduction from 50% upstream water level to the downstream water level which corresponds to expected uplift pressure when there is a grout curtain in operation but no drains. This Figure, also include the two corresponding numerical models (i.e. models with active grout curtain but no drains). These models also give lower uplift pressure than the expected analytical uplift pressure.

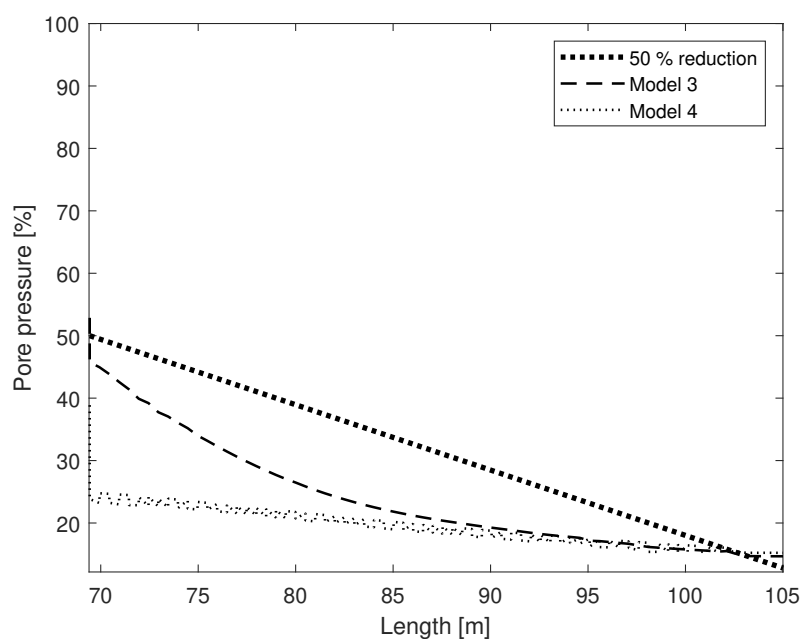


Figure 5.26: Evaluated uplift pressure below the dam for models with grout curtain which should be compared to 50% reduction



Lastly, Figure 5.27 includes the two previously linear reductions and another linear reduction from 30% upstream water level to downstream water level which represents the expected uplift pressure when there is a grout curtain and drains in operation. This figure, also include all the models for the two limiting drainage conditions. Namely, the models with empty (e.i. air filled) drains and models with fully water filled drains. The models with the drains also give lower uplift pressure than the expected analytical uplift pressure, compared with the 30% reduction curve.

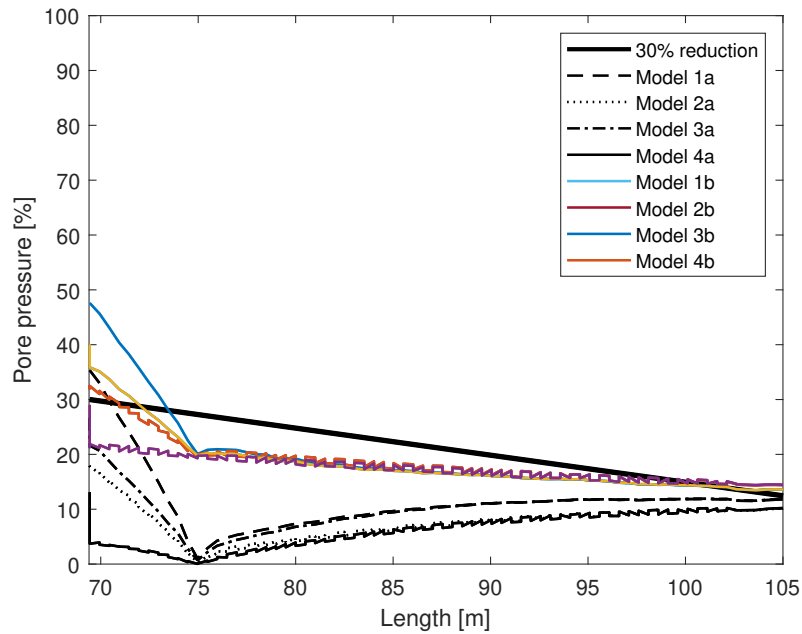


Figure 5.27: Evaluated uplift pressure for models that include drainage which, should be compared to the 30% reduction

### 5.3.4 Model choice for further research

According to the results in Section 5.3, showed that the models that have the best agreement with the field measurements at the sensors were:

- Model 1d with only homogeneous rock and drainage showed the best agreement with measured values. In this model, the pore pressure was underestimated by only 0.40 m.
- Model 4 with fractured rock and intact grout curtain but no drainage showed also good agreement with measured values. In this model, the pore pressure was overestimated by 1.72 m.
- Model 4b with fractured rock, intact grout curtain and fully water filled drains, showed also a good agreement with measured value. Model 4b overestimates the pore pressure by 1.94 m.
- Model 4d which included fractured rock, intact grout curtain and 2/3 water filled drains. Model 4d underestimate the pore pressure by 2.33 m.

As mentioned above, there are four models that have good agreement with the field measurements results and the deviation varied between 0.4 and 2.4 m. The model that was chosen for further research was decided to be the one that corresponded better not only to the resulting hydraulic head at the location of the pore pressure sensors but also to the field conditions. For example, a model that did not include grout curtain or the drains, is not a realistic one because there is evidence that both of these components are installed in the structure. The same statement stands also for the fractures. Consequently, the models 4b and 4d were the ones that were corresponding better to all these considerations. On the other hand, model 4b represented an upper limit case where the drains are fully water filled which does not correspond to a realistic condition of the dam. Therefore, Model 4d is chosen to for further calibration.

It should be also mentioned that the further investigations was not only performed for calibration purposes but also to understand the real condition of some parameters.

## 5.4 Variation of the hydraulic conductivity

This investigation was performed in order to further calibrate the FE model of the monolith 42 and clarify the uncertainties regarding the hydraulic conductivity field measurements. Model 4d was used because it gave the closest hydraulic head at sensors while it also resembled the most realistic conditions related to the current state of the monolith according to the results in Section 5.3.3 and 5.3.4.

The resulting pore pressure distribution of the selected values are illustrated in Figures 5.28 and 5.29. The selected cases are the ones closer to the measured hydraulic conductivity  $K = 10^{-5}$  m/s.

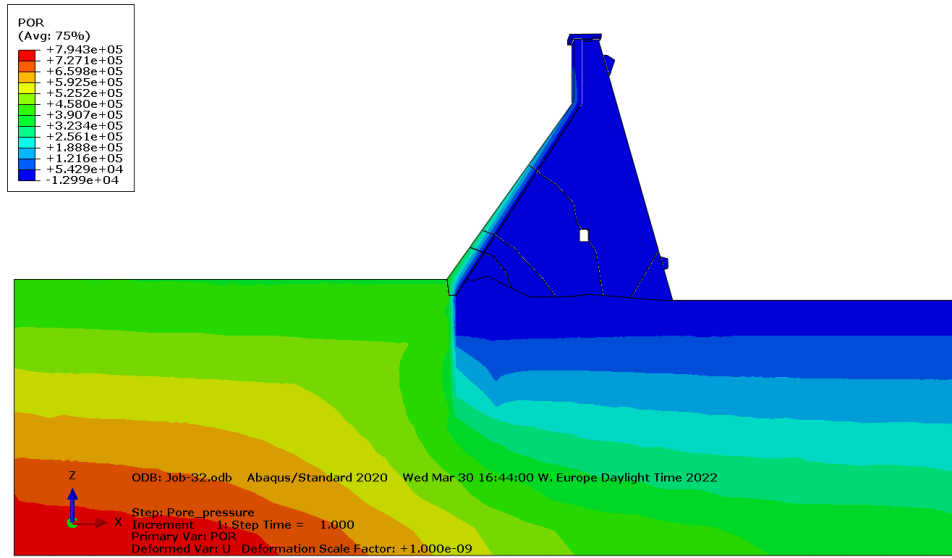


Figure 5.28: Pore pressure distribution of Model 4d with uniform hydraulic conductivity  $K = 10^{-4}$  m/s

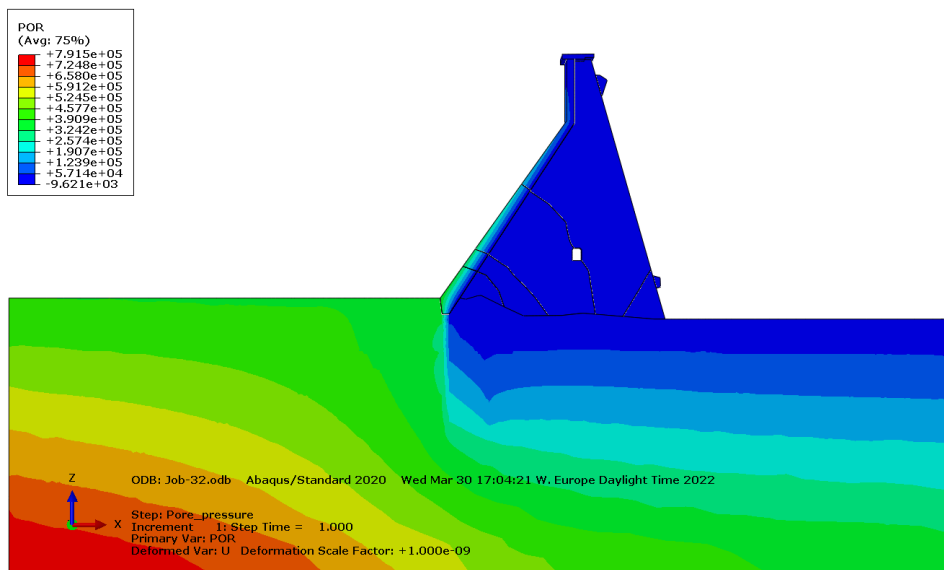


Figure 5.29: Pore pressure distribution of Model 4d with uniform hydraulic conductivity  $K = 10^{-6}$  m/s

Furthermore, the pore pressure distribution along the sub-horizontal fracture for each case is presented in Figure 5.30.

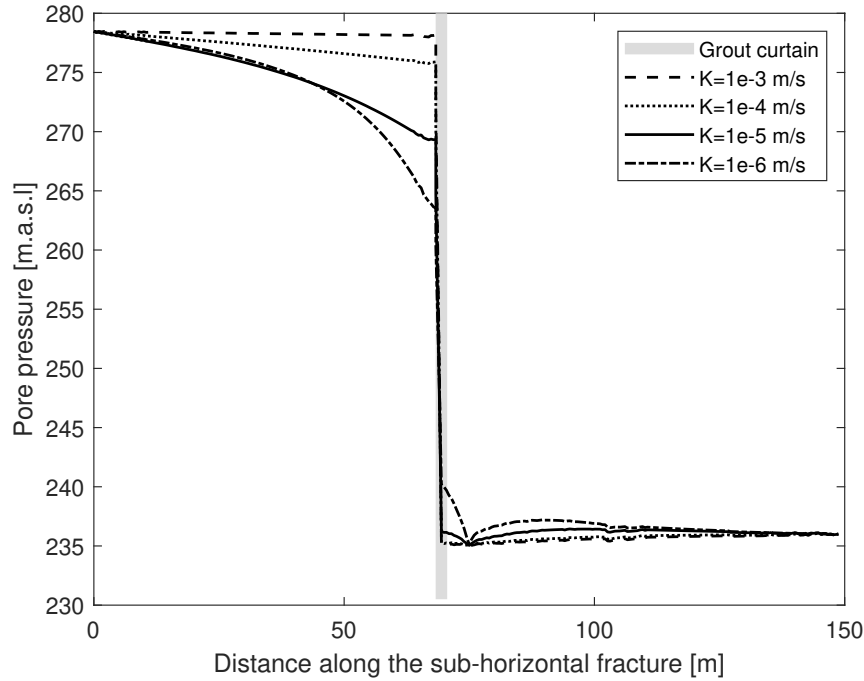


Figure 5.30: Pore pressure distribution along the sub-horizontal fracture for different hydraulic conductivity values

Finally, the resulting pore pressure for the different fracture hydraulic conductivity values at the piezometer sensor are presented and compared in Figure 5.31.

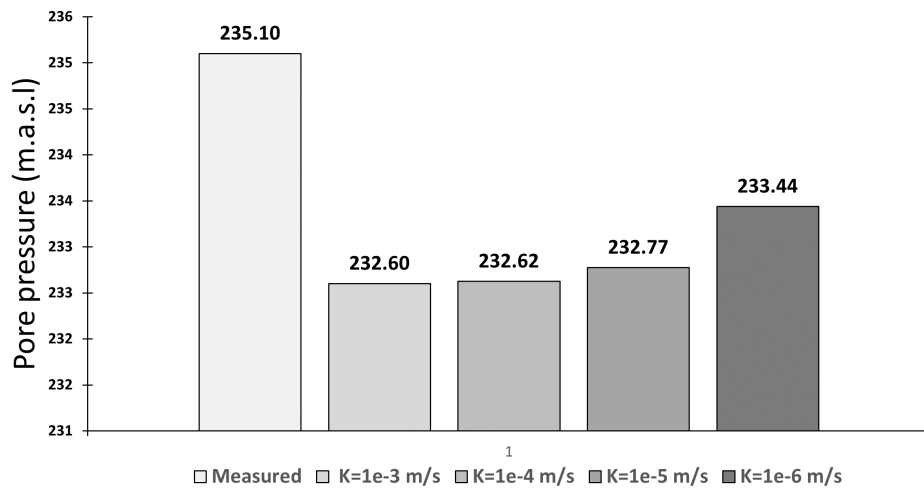


Figure 5.31: Resulting pore pressures at location of the sensors

According to the Figure 5.31 the model that provided the closest measured pore pressure was the Model 4d with  $K=10^{-6}$  m/s which gave  $h_w=233.4$  m. This can be also noticed in Figure 5.30 where the particular hydraulic conductivity value gave the highest uplift pressure area below the dam foundation. Furthermore, it can be observed that the increase in the measured pore pressure happens abruptly while it has almost a constant behaviour

for high hydraulic conductivity values. This indicates that the hydraulic conductivity has a nonlinear behaviour. Finally, it is observed that low hydraulic conductivity values result in lower uplift pressure distribution on the upstream side of the dam and higher on the downstream side according to Figures 5.28 to 5.30.

## 5.5 Alternative models for the hydraulic conductivity

### 5.5.1 Fractures with tapered aperture

Apart from the previous investigation with an uniform fracture hydraulic conductivity at all fractures, fractures with a varying hydraulic conductivity along their length were also investigated as explained in Section 4.12.4. For this purpose Model 4d was used which corresponded closer to the field pore pressure measurements and conditions.

Accordingly, the tapered tube simulation in the FE model is illustrated in the following Figures 5.32 and 5.33. The low hydraulic conductivity is denoted with blue, the medium with gray and the high with beige colour.

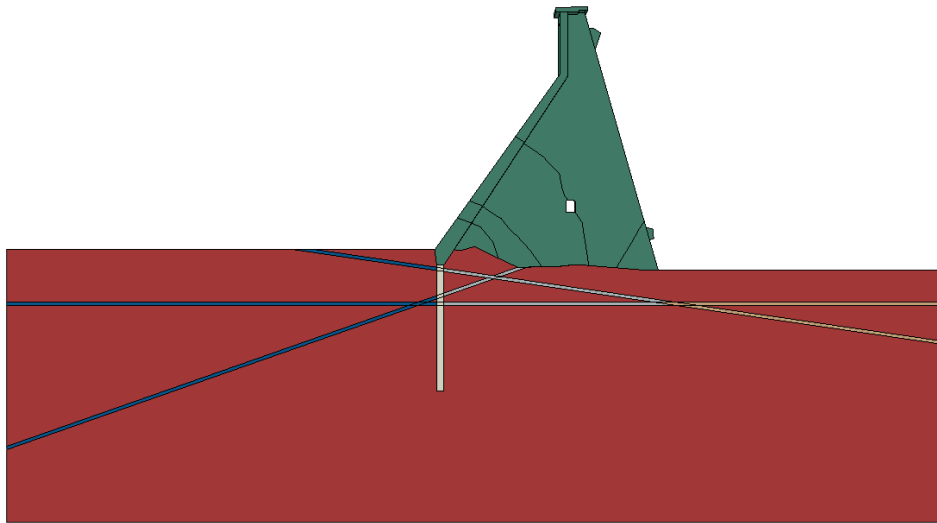


Figure 5.32: Illustration of the Model 4d alt.1F with gradually increasing hydraulic conductivity

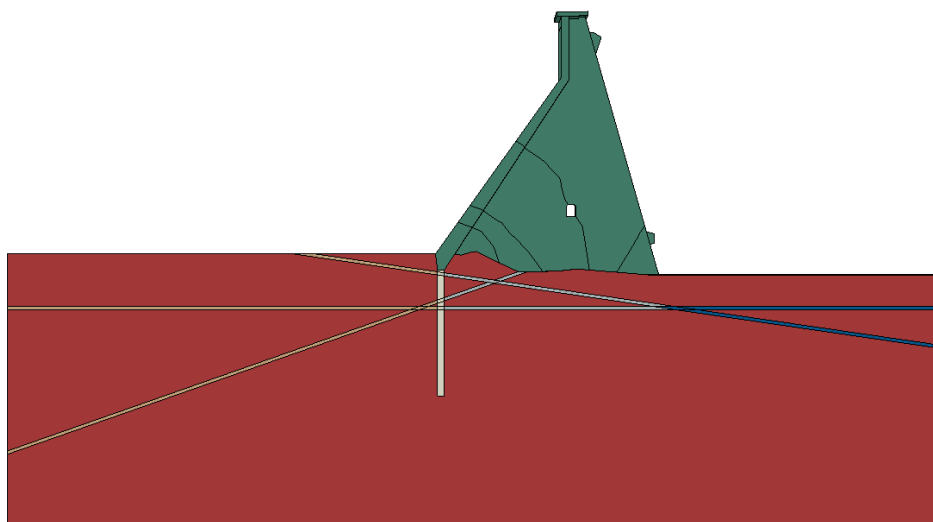


Figure 5.33: Illustration of the Model 4d alt.2F with gradually decreasing hydraulic conductivity

The resulting pore pressure distribution along the sub-horizontal fracture for each case is presented in the following Figure 5.34.

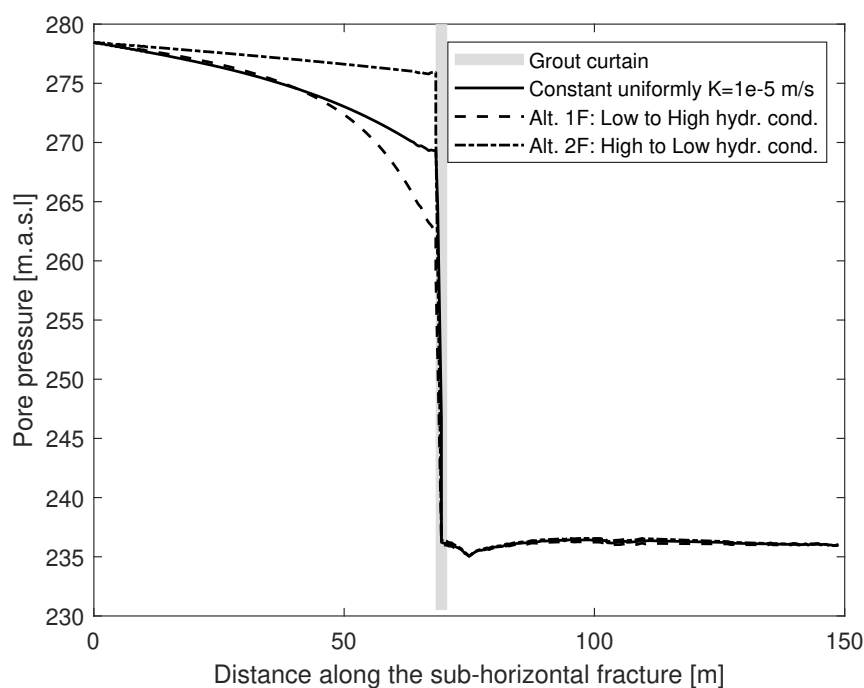


Figure 5.34: Pore pressure distribution of tapered fracture models

Finally, the resulting pore pressure at location of the piezometer sensor for each case are presented in the Figure 5.35. These results are compared with the previous case Model 4d that had a constant and uniform hydraulic conductivity  $K=10^{-5}$  m/s at all fractures.

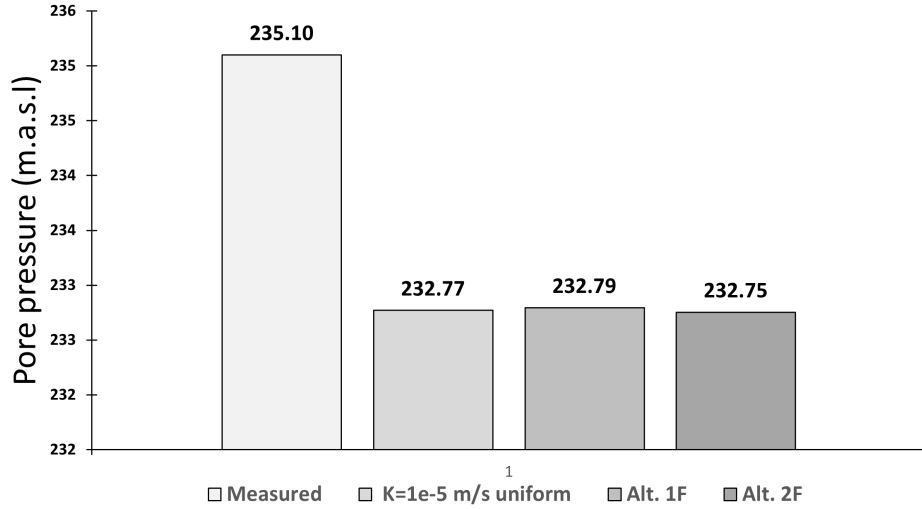


Figure 5.35: Resulting pore pressures at location of the pore pressure sensor

It is observed in Figure 5.34 that on the downstream side of the dam, both Models have almost the same uplift distribution where Model alt.2F developed a little higher. This is also verified from the pore pressure sensor measurements where the measured pore pressure has a very small difference equal to 0.018%. On the other hand, the Model alt.1F developed lower pressure on the upstream side compared to Model alt.2F. Regarding the pore pressures at the sensors, the tapered aperture simulations almost gave similar results to model with a uniform constant value. In this sense, both approaches have the same behaviour.

### 5.5.2 Constant hydraulic conductivity in each fracture

Another approach regarding the fracture hydraulic conductivity was to input different constant values in each fracture. Accordingly, two more alternative combinations were examined that are presented in the following Figures 5.36 and 5.37. Model 4d is used as previously in Section 5.5.1. The low hydraulic conductivity is denoted with blue, the medium with gray and the high with beige colour.

According to Section 4.12.4 the applied hydraulic conductivity values are the following:

- Low hydraulic conductivity  $\rightarrow K = 10^{-6}$  m/s
- Medium hydraulic conductivity  $\rightarrow K = 10^{-5}$  m/s
- High hydraulic conductivity  $\rightarrow K = 10^{-4}$  m/s

The low hydraulic conductivity is denoted with blue, the medium with gray and the high with beige colour in Figures 5.36 and 5.37.

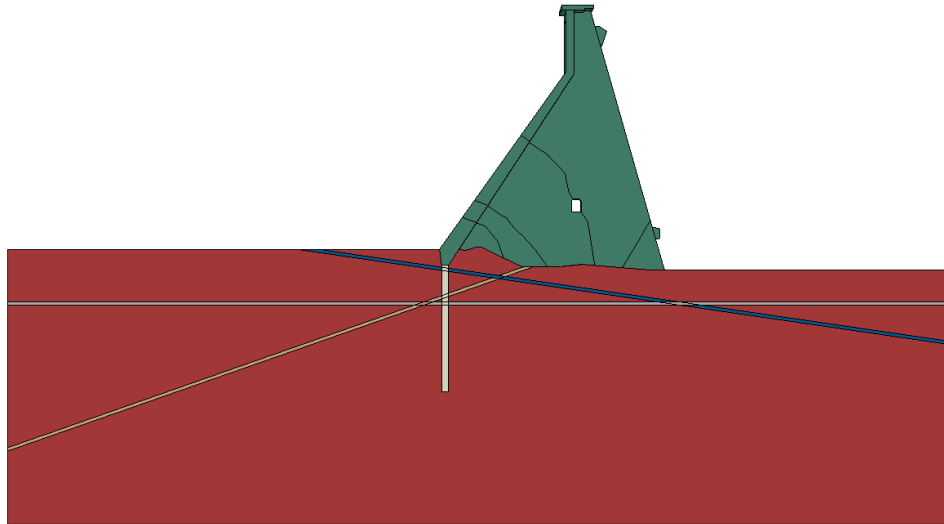


Figure 5.36: Illustration of the Model 4d alt.3F with the corresponding hydraulic conductivity value in each fracture

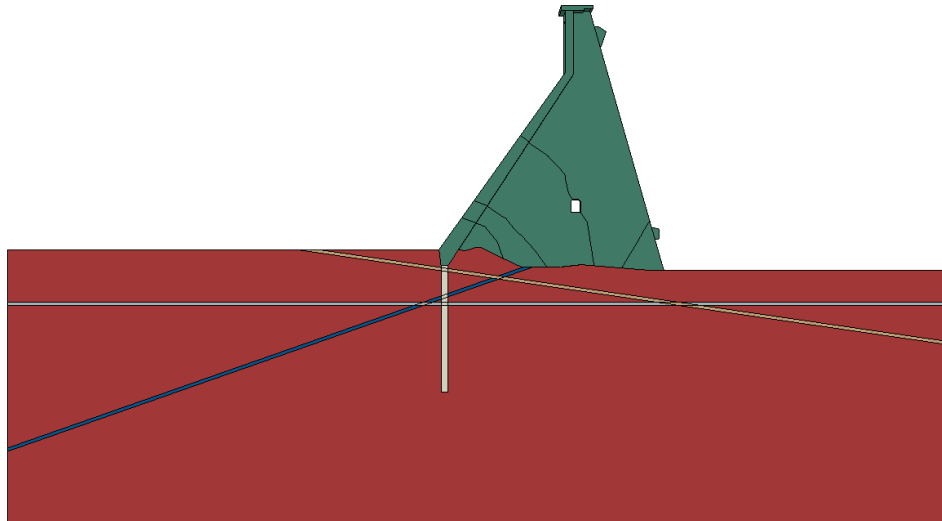


Figure 5.37: Illustration of the Model 4d alt.4F with the corresponding hydraulic conductivity value in each fracture

The resulting pore pressure distribution along the sub-horizontal fracture for each alternative model is presented in Figure 5.38.



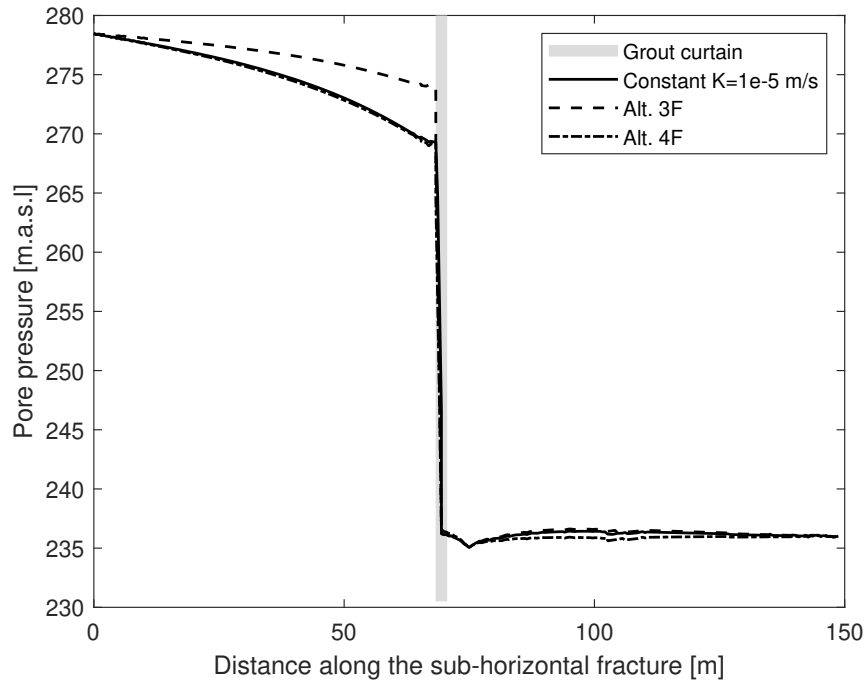


Figure 5.38: Pore pressure distribution of Models alt.3F and alt.4F

Finally, the resulting pore pressure at the piezometer sensor for each hydraulic conductivity combination case are presented in the Figure 5.39 and they are compared with the Model 4d with a constant hydraulic conductivity  $K=10^{-5}$  m/s at all fractures.

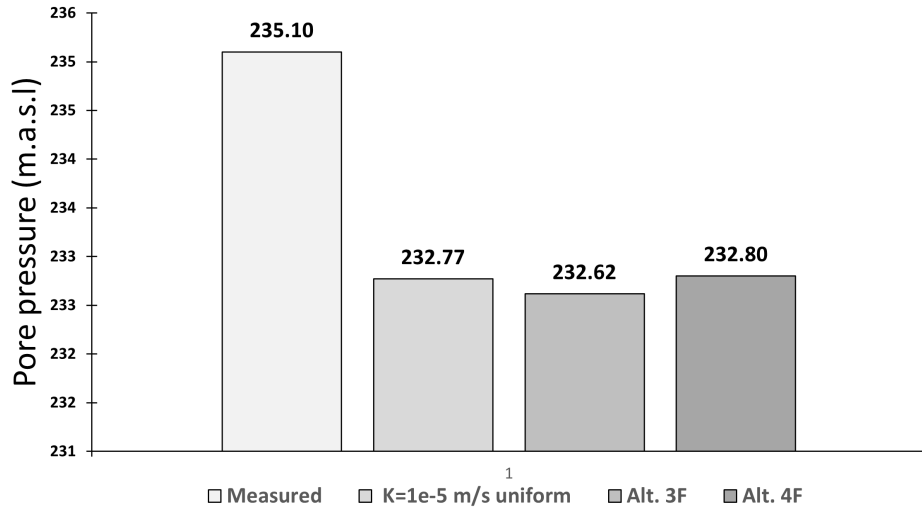


Figure 5.39: Resulting pore pressures at location of the pore pressure sensor

It can be observed that Model 4d alt.3F resulted to higher uplift distribution below the dam area, although Model 4d alt.4F produced slightly higher pore pressure at the sensors. The difference between the Model 4d with a constant uniform hydraulic conductivity value for all the fractures is very small. It could be also noticed that there is very small difference with the tapered aperture simulations presented in Section 5.51. Overall, all alternative models have almost the same measured pore pressure with constant value approach, thus a constant hydraulic conductivity in all fractures describes sufficiently the dam state.

## 5.6 Alternative models for the grout curtain

The investigation was performed by using the Model 4d with a constant hydraulic conductivity equal to  $K = 10^{-6}$  m/s applied uniformly to all fractures. This model was chosen due to the fact that it produced a hydraulic head closer to the measured one, according to the previous chapter paragraph 5.3 results. According to Section 4.12.5, the alternative models are defined in Table 5.1.

Table 5.1: Investigated models for the grout curtain

Model 4d	Characteristics
Alt.1G	intact short grout curtain
Alt.2G	leached long grout curtain hydraulic conductivity $K = 10^{-7}$ m/s
Alt.3G	bypassed long grout curtain

The resulting pore pressure distribution along the sub-horizontal fracture for each grout curtain case is presented in Figure 5.40.

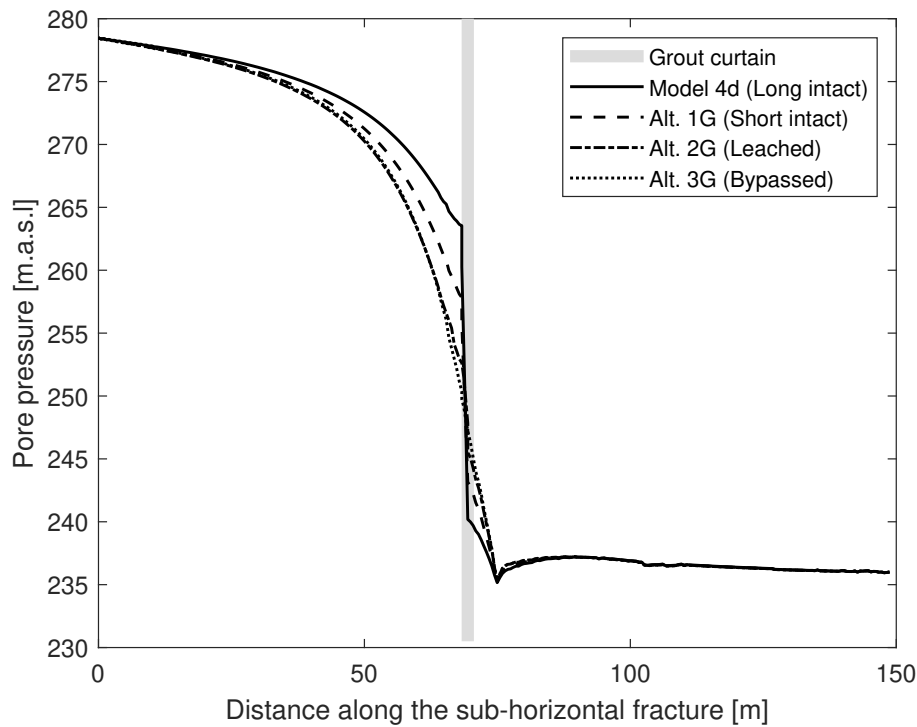


Figure 5.40: Pore pressure distribution for the different grout curtain cases

Finally, the resulting hydraulic heads at the piezometer sensors for each grout curtain alternative are presented in Figure 5.41 and they were compared with the measured one.

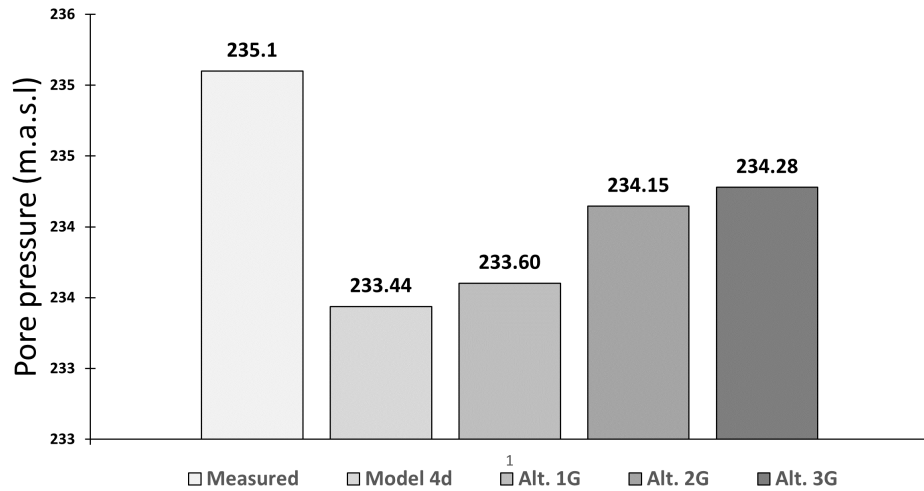


Figure 5.41: Pore pressure results at the sensors for the different grout curtain cases

According to Figure 5.40, most of the models had similar pore pressure distribution at the downstream side, except the Model 4d which had quite smaller. On the other hand, model 4d had the highest pore pressure distribution at the upstream side.

By comparing the measured pore pressure of models 4d and alt.1G in Figure 5.41, it is noticed that they have a very small difference of 0.16 m, therefore the grout curtain depth is not affecting much the uplift pressure.

Lastly, by comparing models 4d and alt.3G with bypassed grout curtain, it is noticed an increase of 0.84m. In this sense, a deteriorated grout curtain increases substantially the uplift pressure. Due to the fact that probably a long curtain was installed during the construction of the dam and because it could be deteriorated after so many years of use, Model 4d alt.3G could potentially resemble the real state of the monolith.



# Chapter 6

## Sliding stability analysis

The safety factors for sliding in the fracture planes were determined for the failure cases A and B that were mentioned in Sections 3.5.1 to 3.5.2. Furthermore, safety factors were calculated according to RIDAS guideline suggestions for three different states as presented in Section 3.5.3. In order to calculate the safety factors, all the applied loads were calculated analytically except the uplift forces which were extracted from the FE analysis for every selected model. The selected models that were used to calculate the safety factors were the following that are defined in Table 6.1.

Table 6.1: Models used for sliding stability analysis calculations

Model	Cause
4d alt.3G	combines both realistic field conditions and a satisfactory hydraulic head close to the measured one
4a	resembles the lower limit condition for the current state of the monolith with fully air-filled drains
4b	resembles the upper limit condition for the current state of the monolith with fully water-filled drains

Furthermore, the three different states that were used to calculate safety factors according to RIDAS guideline are defined in Table 6.2.

Table 6.2: Condition states according RIDAS guideline

State	Cause
1	Full hydrostatic, the drains and the grout curtain are not included
2	Drain reduction is included
3	Drain and grout curtain reduction is included

## 6.1 Wedge passive forces

Firstly, the uplift force at the passive wedge was the same for each failure case but different for each model. This happened due to the fact that for each failure scenario, the formed wedge had the same formed shape. The uplift forces were extracted directly from the pore pressure analysis performed at Abaqus and were also determined analytically. The resulting uplift distribution is presented in Figure 6.1.

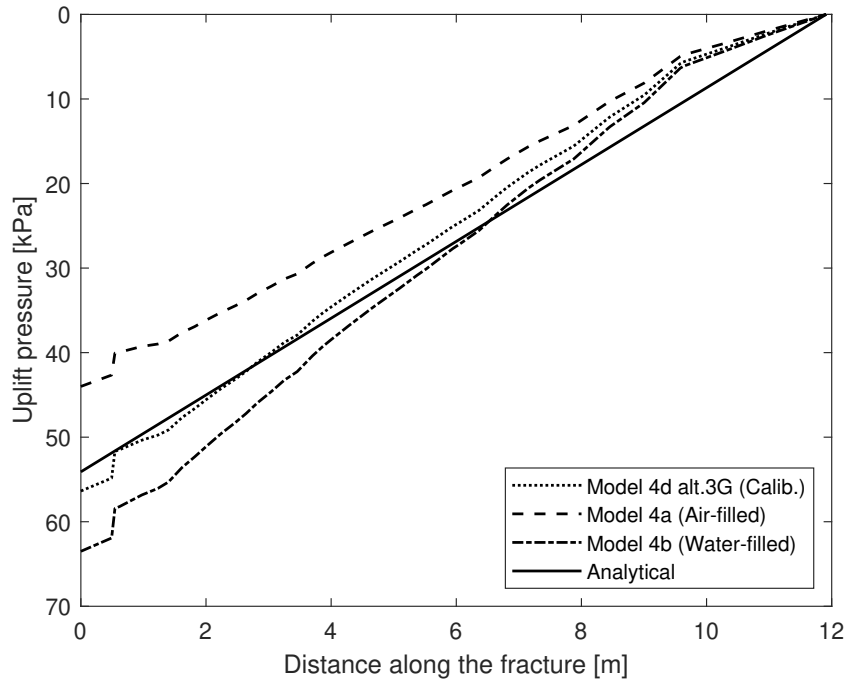


Figure 6.1: Uplift wedge distribution of each model and analytically determined

The wedge inclination is calculated by Equation 2.17 and is equal to  $\theta=27^\circ$  while fracture friction angle is  $\phi=36^\circ$  according to Section 3.4. The resulting wedge passive forces are calculated by Equation 2.16 and are presented in Table 6.3.

Table 6.3: Resulting wedge passive forces

Model	Uplift force, $U_{wp}$ [MN]	$P_{pass}$ , [MN]
4d alt.3G	2.44	6.94
4a	1.96	7.86
4b	2.72	6.40
Analytical	2.58	6.65

According to Table 6.3, high uplift forces result in low the passive force because the uplift forces reduce the wedge rock load. The analytical passive force was very close to the numerical passive forces, thus it is not conservative. This is also verified in Figure 6.1 where the analytical pore pressure distribution almost aligns with the numerical ones.

## 6.2 Safety factors

The schematic illustration of the applied loads for every case are presented in Figures 3.10 and 3.11 in Sections 3.5.1 and 3.5.2.

In Case A is examined the scenario where the extended inclined fracture is assumed crushed due to high uplift forces. Accordingly, higher hydrostatic horizontal loads and reduced rock monolith load are assumed that could lead to even worse case scenario. In Case B is examined a horizontal fracture sliding plane. In this scenario are created the highest hydrostatic horizontal loads but also the highest rock monolith load compared to the other case. The uplift forces were extracted directly from every pore pressure analysis that was performed for each model according to Figures 6.2 and 6.3.

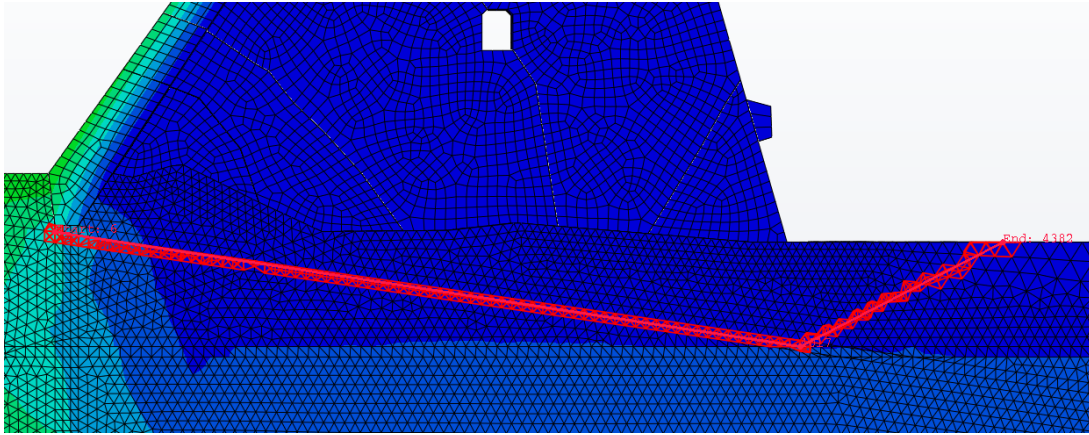


Figure 6.2: Illustration of the applied path in Abaqus regarding Case A

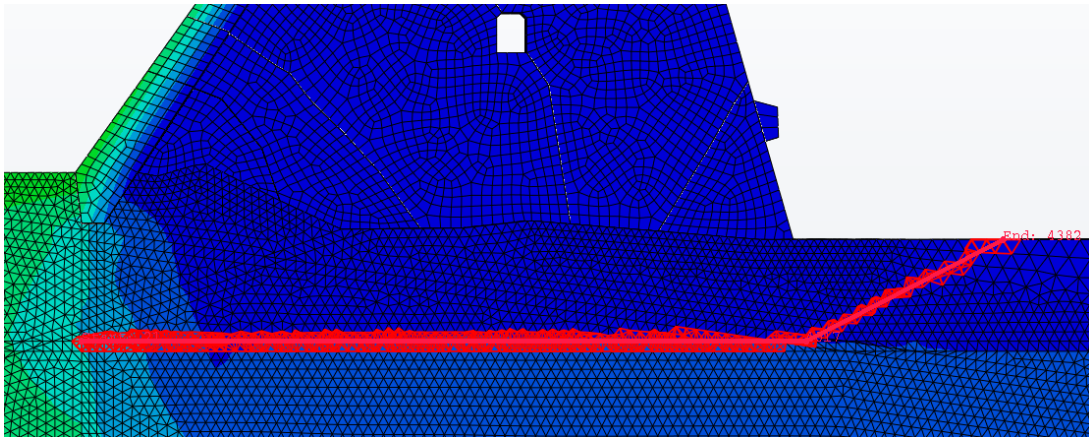


Figure 6.3: Illustration of the applied path in Abaqus regarding Case B

Moreover, the resulting numerical uplift pore pressure distributions for every model and the resulting uplift distributions according to the guideline different states from section 3.5.3 are presented in the following figures.

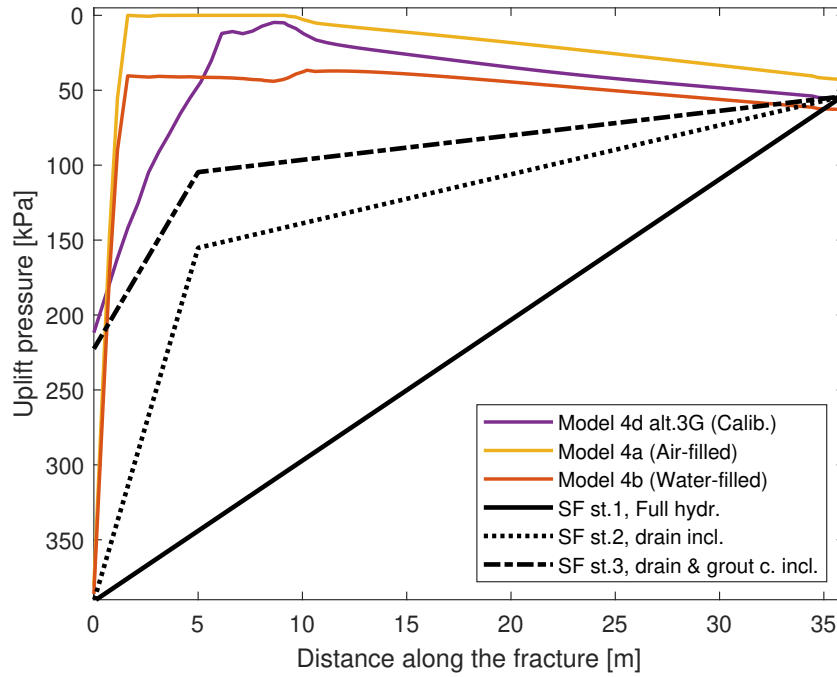


Figure 6.4: Uplift pressure distribution of failure Case A

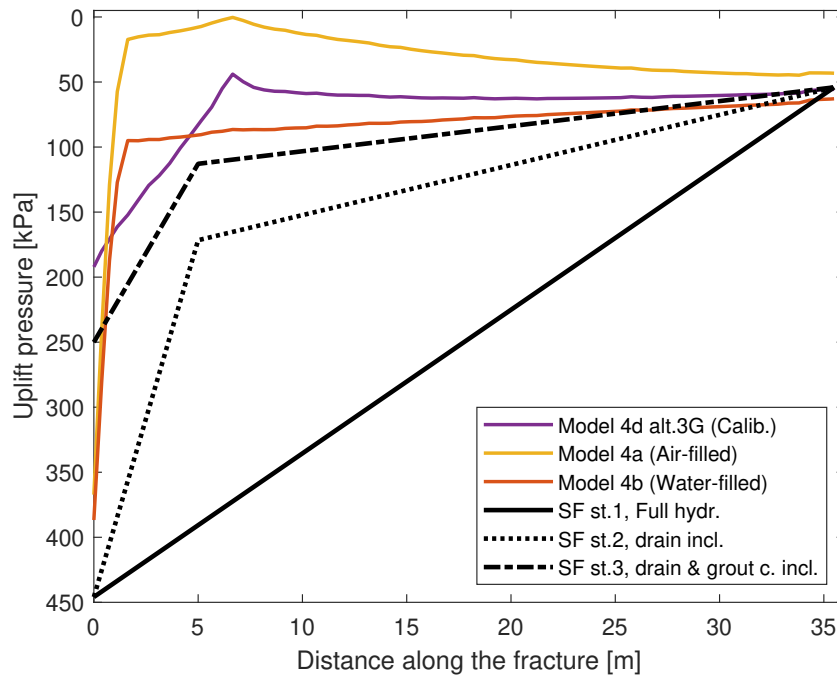


Figure 6.5: Uplift pressure distribution of failure Case B



Finally, In order to calculate the safety factors, force equilibrium was applied in both vertical and horizontal forces and the Equations 2.18 and 2.19. The resulting safety factors for each failure case are presented in Figure 6.6.

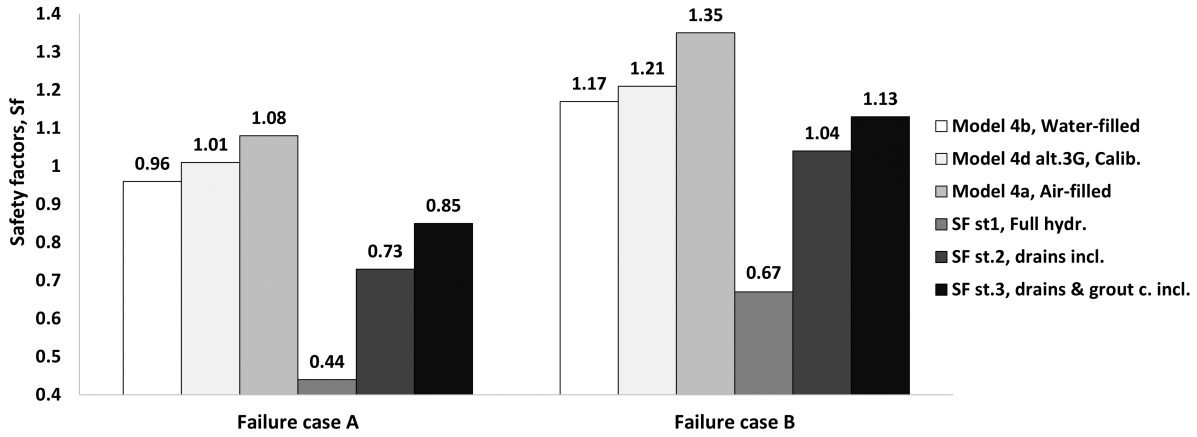


Figure 6.6: Resulting safety factors of the numerical models and according to the guidelines for each sliding failure case

According to Figure 6.6, the Model 4b which simulates fully water-filled drains gave the lowest safety factors while the Model 4a which simulates fully active drains gave the highest safety factors in all failure cases. These results indicate the importance of the proper functioning of the drainage system because it is the factor that mostly influences the distribution of the uplift forces, thus the safety of the dam. This is also verified in Figures 6.4 and 6.5 where the resulting uplift pressure distribution of Model 4a was lower than Model 4b.

By comparing the guideline and the numerical safety factors in Figure 6.6, it can be understood that the guidelines produce lower safety factors compared to the numerically derived ones. This happens because the guideline suggested uplift distributions are higher compared to the numerically extracted ones according to Figures 6.4 and 6.5. The guidelines are more conservative compared to the possible conditions of the dam, even if the worst scenario is considered in the numerical simulations. Due to the fact that the guidelines assume that the uplift distributions develop linearly, the resulting uplift forces are much higher compared to a nonlinear distribution which corresponds to the real behaviour.

On the other hand, it can be also noticed that guideline State 3 which includes both the influence of the drains and the grout curtain, gave closer values to the numerical ones which indicates that by including the grout curtain the guideline safety factors are more realistic. In fact State 3 describes better the real uplift pressure distribution of the numerical models.

Lastly, Case A provided lower safety factors than Case B, hence the inclined sliding failure plane is more critical than the horizontal. A possible explanation is that the horizontal fracture provides larger rock area consequently higher rock monolith load than the inclined fracture which increases significantly the resulting downforce.

### 6.3 Effect of deep fractures

This investigation was conducted by choosing the sliding failure plane of case B which produced the lowest safety factors and the analysis was performed by using the Model 4d alt.3G which is the most calibrated and corresponds better to the site conditions and measurements. As mentioned in Section 3.6, purpose was to see how the fracture depth influences the sliding stability safety factor.

The sliding plane A positioned in consecutive deeper locations in the rock foundation with an interval of 2 m. The fracture and the wedge uplift forces were extracted numerically for each position. The resulting safety factors for each examined depth are presented in Table 6.4.

Table 6.4: Resulting safety factors for every examined depth

Depth [m]	Hydr. load, $F_{hor}$ [MN]	Uplift, $U_p$ [MN]	$P_{Rock}$ [MN]	$P_{pass}$ [MN]	$S_f$
0.21	61.16	13.09	24.22	6.94	1.000
2.21	67.70	18.43	39.12	11.95	1.039
4.21	74.44	24.01	45.60	19.30	1.042
6.21	81.50	29.90	68.66	28.18	1.187
8.21	88.90	35.32	83.43	38.80	1.299
10.21	96.60	42.52	98.20	51.65	1.438
12.21	104.61	49.96	112.95	62.95	1.540
14.21	112.95	56.43	127.71	82.93	1.901

The calculated safety factors are also presented graphically in the following Figure 6.7.

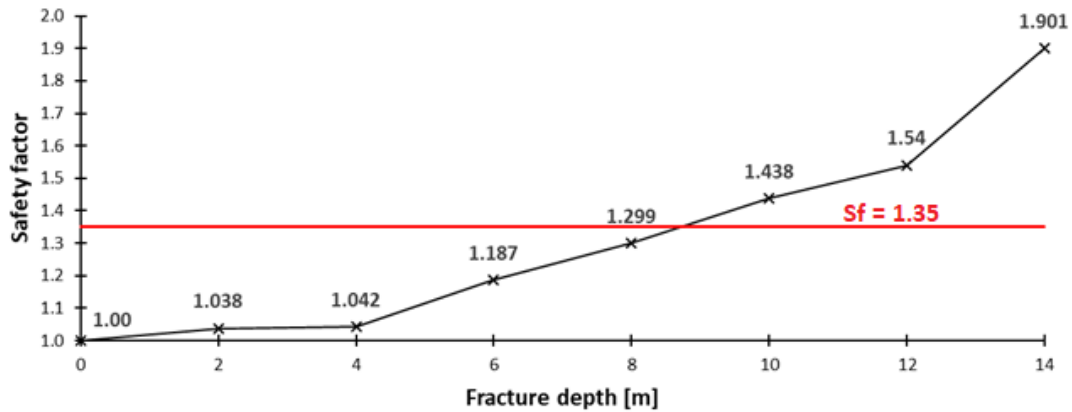


Figure 6.7: Resulting safety factors for each fracture depth

According to Figure 6.7, the safety factors are developing nonlinearly with different inclinations and three different zones can be identified. These zones are categorized in the following Table 6.5.

Table 6.5: Safety zones related to the fracture depth

Safety zone	Avg. depth, [m]	SF
Low	0.00 - 4.30	1.00 - 1.05
Moderate	4.30 - 12.30	1.05 - 1.54
High	12.30 - 14.30	1.54 - 1.90

The first zone has a very small inclination with almost constant behaviour, thus the safety factors increase slowly. It can be described as low safety zone because their safety factors range from 1.00 to 1.05 and all the fractures at this depth should be considered in stability analyses.

Moreover, the second zone has a higher inclination which means that the safety factors increase faster per depth and has an almost linear behaviour. This zone can be described as moderate safety zone because the safety factors range between 1.05 and 1.54 and after a certain depth the structure has enough stability, hence fewer fractures should be analyzed in stability analysis.

Finally, the third zone has higher inclination compared to the second zone and the safety factors increase even faster per depth. It is a high safety zone due to the fact that for all the fracture depths the safety factors are above the recommended  $S_f=1.35$ . These fractures could be ignored and no further analysis is required.

Overall, fractures with an average depth between 0.00 - 10.00 m should be investigated and included in a stability analysis but after 14.00 m they could be neglected. This can be explained from Table 6.4 where after the depth of 10.00 m, the uplift forces are not enough to destabilize the resistant forces of the rock monolith and the passive wedge support.

## 6.4 Friction angle effect

The friction angle  $\phi$  is mostly related to the shape and size of the grains that are exposed on the fracture surface (Bondarchuk, 2012). Another important parameter is the roughness and the asperities of the joint surface which affect significantly the shear strength of the fracture (Bondarchuk, 2012).

The effect of the friction angle was examined by inputting different values that were varying between  $30^\circ$  -  $50^\circ$  and the corresponding safety factors were extracted. For this analysis was chosen the Model 4d alt.3G (most calibrated) and failure sliding plane case B was examined. The resulting safety factors for each friction angle value are presented in the following Figure 6.8.

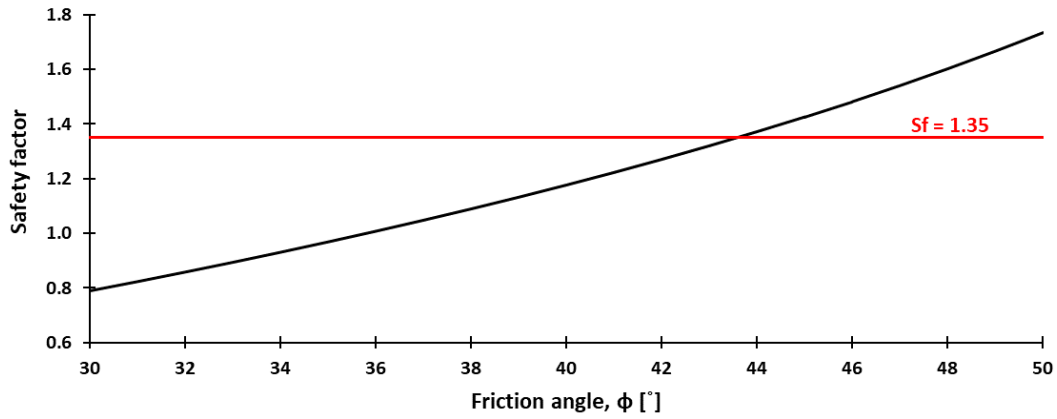


Figure 6.8: Resulting safety factors for each friction angle value

It can be observed that close to the value  $\phi=44^\circ$ , the safety factor becomes sufficient, thus close to the recommended  $S_f=1.35$ . Moreover, both parameters change almost with same rate, although the change rate is definitely nonlinear.

Overall, the fracture friction angle parameter is important and greatly affects the safety factor. By increasing the friction angle the stability of the fracture plane increases while low values result to more flat surfaces, thus the fracture plane slides easier and decrease the stability.

# Chapter 7

## Discussion

For this project, multiple analyses have been carried out to investigate the pore pressure and evaluate its magnitude and distribution in the rock foundation underneath monolith M42 at Storfinnforsen buttress dam. In these analyses, a range of factors have been investigated to capture all the combinations that could represent the real condition of the dam. The considered factors include e.g. the influence of rock fractures in the foundation, different joint properties and assumptions, the influence of grout curtain with different depth and modeling techniques and presence of drainage with different water fillings.

The RQ1 regarding the influence of drains, grout curtain and rock fracture is answered in Section 7.1. The RQ2 regarding the comparison between the numerical and the guideline safety factors is answered in Section 7.2 while the RQ3 regarding fracture depth influences the safety factor is answered in Section 7.3. The RQ4 related to the friction angle effect on the safety factors is discussed in Section 7.4.

### 7.1 Numerical models

#### 7.1.1 Influence of drains

The analyses without drains (i.e. Model 1 to Model 4, where the drains are assumed to be clogged), overestimate the pore pressure significantly compared to the field measurements except model 4 which includes fractured rock foundation and intact grout curtain. In this model, the grout curtain stops the flow of the pore pressure in the rock fractures. This create high pore pressure at upstream side of the grout curtain, and lower the pore pressure underneath the dam where the pore pressure sensors are installed and therefore has this specific model showed the lowered pore pressure at the location of the pore pressure sensors. This indicates that there are functional drains in operation otherwise, it would be difficult to obtain as low pore pressure as the measured values.

The analyses that included the effect of drains, gave significantly lower pore pressure than the cases without drains. This shows that the drains have a great influence on the pore pressure underneath the dam. As described earlier, it was difficult to simulate the real condition of the drains and therefore some simplified cases have been investigated which would at least capture the lower and upper boundary of the pore pressure when the drains are in operation. The lower limit of the pore pressure were represented by the empty drains ( i.e. air filled drains) while the upper limit were represented by the water filled drains. In the end, the model with 2/3 water filled drains showed best agreement with the measure pore pressure

- a) When drains are in operation, assuming empty drains underestimate the pore pressure while assuming fully water filled drains overestimate the pore pressure.
- b) The models with the half-filled drains or 2/3-filled drains also slightly underestimate the pore pressure. Nevertheless, this considered to be the to the real conditions of the dam, especially the model with the 2/3-filled drains.

### 7.1.2 Influence of rock fractures

For the first investigated parameter, the sensitivity analysis showed according to the Figure 5.30, that a low value decrease the uplift pressures at the upstream side while it increases them in the downstream side. According to the Figure 5.31 the lowest hydraulic conductivity  $K = 10^{-6}$  m/s gave the highest measured pore pressure which was also the to the field measurements. This result indicate that the initially assumed conductivity of  $K = 10^{-5}$  m/s could be an overestimation. The fractures might have less aperture size along their extension or they might be filled with rock material in some areas that decreases their hydraulic conductivity.

Furthermore, the scenarios of fractures with varying hydraulic conductivity along their length and fractures with different hydraulic conductivity were examined and compared with the scenario of a constant uniformly hydraulic conductivity in all fractures. The results according to Figures 5.35 and 5.39 showed that all the alternative models have similar measured pore pressure compared to an applied constant uniformly hydraulic conductivity, thus the real behavior of the fractures could be simulated satisfactorily with a constant value without variations and all the fractures probably have the same hydraulic conductivity.

### 7.1.3 Influence of grout curtain

The influence of intact grout curtain varies if the effect of drains are included or not. In the analyses when the drains are considered to be clogged, the grout curtain reduces the pore pressure significantly in the case where the rock foundation is fractured. This reduction is emphasized in Figure 7.1, see the first group (without drains). The grout curtain gives, in this case, a pore pressure reduction of about 8.5 m in hydraulic head.

In the analyses that include the effect of drains, the influence of grout curtain is almost none existent, regardless if the drains are empty or water filled. This can be also observed in Figure 7.1. This means that as long as the drains are in operation, the presence of grout curtain does not change the pore pressure underneath the dam and thus, does not contribute much to the dam safety.

If homogeneous rock foundation is considered, the influence of grout curtain is small regardless if the effect of drains are included or not.

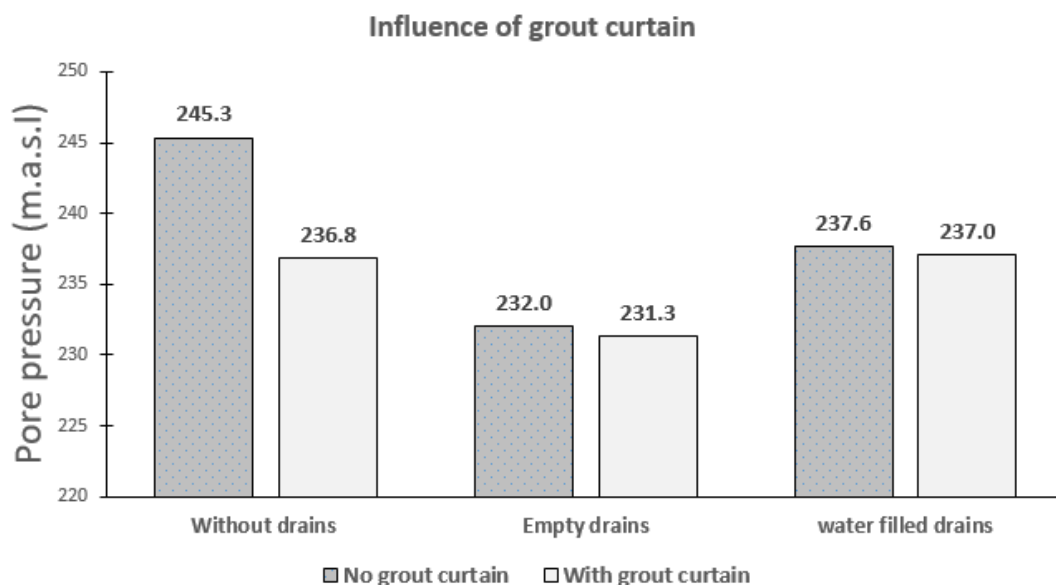


Figure 7.1: Influence of intact grout curtain in models that include rock fractures

Moreover, to capture the condition of the grout curtain a further investigation regarding different parameters of the grout curtain such as variation of the grout curtain depth and its properties were performed. These analyses have showed that variation of the grout curtain depth does not influence the pore pressure at the location of the pore pressure sensors.

Finally, a deteriorated grout curtain could have an important impact both to the pore pressure distribution and the magnitude of the uplift force. According to Figure 5.41, Model 4d alt.3G with bypassed grout curtain produced the closest pore pressure to the field measurements. In this sense, this model could potentially resemble better the state of the dam. This would mean that the grout curtain is leached and fractures bypass it.

Another aspect to consider is that the grout curtain have good effect when it intersect the rock fractures underneath the dam. However, this effect diminishes if the rock fractures bypass the grout curtain or if the grout curtain does not reach the location of rock fractures.

## 7.2 Safety factors

According to Chapter 6, sliding stability analysis was performed for two failure sliding cases A and B which are are represented in the Figures 3.10 and 3.11. Moreover, three

models were used to extract the uplift pressure distribution in each fracture plane and calculate the safety factors. Furthermore, RIDAS guideline was used to define three different states regarding the uplift distributions which are described in Section 3.5.3.

The numerically extracted uplift pressures have a nonlinear distribution while the guidelines assume a linear uplift distribution. The assumption of the linear uplift distribution resulted to higher uplift forces than the nonlinear distribution, thus the guideline safety factors were lower compared to the numerically calculated ones. But this is the main purpose of the guidelines, to be always on the safe side because there are always many uncertainties especially for the definition of the rock parameters. Furthermore, the calculated safety factors for both approaches were lower than the  $S_f=1.35$  but this is also a result of significant conservatism. For example, it is assumed that the fracture sliding planes extend along the whole width of the monolith while there is no substantial evidence for this assumption.

Moreover, it should be noted that by including the grout curtain 50% reduction of the uplift pressure, the resulting pore pressure distribution described better the numerical uplift distributions. According to Figures 6.4 and 6.5, this 50% reduction is a safe assumption because the uplift pressure distribution of Model 4d alt.3G with bypassed grout curtain is below the guideline suggested distribution with both drains and grout curtain included (State 3). In this sense a deteriorated grout curtain distribution can be predicted by using the guidelines.

Finally, the failure case A produced the lowest factors, because this sliding plane had a very small angle which resulted to very small rock monolith area which could not provide enough downforce to resist the uplift forces.

## 7.3 Deep fractures

In this investigation it was examined the depth parameter related to the safety factors. According to Figure 6.7 the critical depth positions are for fractures located at a depth less than 4.30 m and should be included in the sliding stability analysis. On the other hand, fractures below 12.00 m could be neglected because due to high depth the resulting rock monolith and the wedge support volume are large enough to resist the developed uplift forces. It should be also noted that the resulting uplift forces after 12.00 m start to stabilize and increase with a slower pace compared to the resisting loads.

## 7.4 Friction angle

This investigation showed that the friction angle related to the safety factors develop nonlinearly and by increasing the friction angle, the safety factors also increase with a smaller pace. Although the laboratory value is considered as valid, it resembles only a few extracted points compared to the total rock foundation area. It could be an underestimation and in certain areas of the rock mass the friction angle values could be higher



than the recommended one. The real rock surface is highly irregular which means that the sliding resistance is higher in reality than in the calculations.



# Chapter 8

## Conclusions and further research

### 8.1 Conclusions

Based on the findings in this thesis, it can be concluded that:

- The presence of functional drainage system is crucial for the safety of the dam. Therefore, it is important to prevent clogging of the drains in order to avoid high pore pressure underneath the dam.
- It is important to have an intact functional grout curtain in operation in order to further decrease the uplift pressure underneath the dam, although this reduction would be rather small compared to the effect from drains that are in operation.
- A leached grout curtain had increased the pore pressure at the sensors substantially, thus its current condition should be examined further.
- Smaller fracture hydraulic conductivity values than the measured one tend to increase the uplift forces and better corresponded to the measured pore pressure.
- Tapered fractures corresponded poorly to the field measurements. A constant uniformly fracture aperture is more realistic approach.
- Fractures below a depth of approximately 12.00 m have high sliding safety factors and they are not critical for stability of the dam.
- High friction angles increase the stability of the dam.

## 8.2 Further research

The numerical pore pressure analyses presented in this thesis are based on a case study performed at monolith M42 in Storfinnforsen concrete buttress dam. Same pore pressure analyses could be performed on other monoliths in Storfinnforsen or the neighbouring buttress dam Ramsele. It could be also used for other types of dams and other types of rock fractures. Other aspects that could be further investigated could be the rock parameters such as the persistence of the fractures, thus to analyze models with different fracture length or fractures with different inclinations. Lastly, the current status of the grout curtain could be examined more.

# Bibliography

ABAQUS (2014), *Documentation Version 6.14*, Dassault systems.

Alcalá Perales, D. (2016), Spatial variation in uplift pressure and correlation with rock mass conditions under two buttress dams: A case study of ramsele and storfinnforsen dams, Master's thesis, KTH.

Bernstone, C., Westberg, M. and Jeppsson, J. (2009), 'Structural assessment of a concrete dam based on uplift pressure monitoring', *Journal of geotechnical and geoenvironmental engineering* **135**(1), 133–142.

Bondarchuk, A. (2012), Rock mass behavior under hydropower embankment dams with focus on fracture erosion and rock mass stability, PhD thesis, Luleå Technical University.

Broberg, L., Malm, R. and Enzell, J. (2020), Instrumentation of storfinnforsen and ramsele concrete buttress dam -use of fea to assess the expected response, Technical report, Sweco Energuide AB,.

Ebeling, R. M., Foster, L., Jones, H. W., Taylor, R. and Bumworth, J. (2000), Evaluation and comparison of stability analysis and uplift criteria for concrete gravity dams by three federal agencies, Technical report, Army Engineer Waterways experiment station Vicksburg MS Engineer Research and development center.

Ebeling, R. M. and Pace, M. E. (1996*a*), 'Uplift pressures resulting from flow along tapered rock joints', *USA Army Corps of Engineers REMR Bulletin* **13**(1).

Ebeling, R. M. and Pace, M. E. (1996*b*), 'Variation in uplift pressures with changes in loadings along a single rock joint below a gravity dam', *USA Army Corps of Engineers REMR Bulletin* **13**(1).

EPRI (1992), Uplift pressures, shear strengths and tensile strengths for stability analysis of concrete gravity dams, Technical Report TR-100345-V1.

Falcão de Queiroz, D. (2018), An alarm system for pore pressure measurements in the foundation of concrete dams: a case study of storfinnforsen buttress dam, Master's thesis, KTH.

FERC (1997), Engineering guidelines for the evaluation of hydropower projects: Chapter x - other dams, Technical report, Federal Energy Regulatory Commission.

Grenoble, B. and Amadei, B. (1990), Evaluation of uplift pressure for concrete gravity dams founded on jointed rock: Analytical results, Technical report, U.S. Committee on Large Dams, Denver.

- Isander, A., Nilsson, C. and Malm, R. (2013), Evaluation and structural rehabilitation of storfinnforsen concrete buttress dam, in ‘CFBR Modernisation des barrages, Chambéry’.
- ISRM, I. (1978), ‘Suggested methods for the quantitative description of discontinuities in rock masses’, *Int J Rock Mech Min Sci Geomech Abstr* **15**(6), 319–368.
- Johansson, F. (2005), Stability analysis of large structures founded on rock: an introductory study, PhD thesis, KTH.
- Johansson, F. and Broberg, L. (2017), Assessment of potential sliding planes in the rock foundation for the monoliths included in the first stage of instrumentation at storfinnforsen and ramsele, Technical report, Sweco Energuide AB.
- Lindfors, U. (1996), Experimental study of the mechanics of rock joints, PhD thesis, Luleå Technical University.
- Malm, R. (2021), Pore pressure analyses of sff m42, Technical report, Sweco Energuide AB.
- Markou, N. and Papanastasiou, P. (2018), ‘Petroleum geomechanics modelling in the eastern mediterranean basin: analysis and application of fault stress mechanics’, *Oil & Gas Science and Technology–Revue d’IFP Energies nouvelles, EDP sciences* **73**, 57.
- McKay, M. and Lopez, F. (2013), Practical methodology for inclusion of uplift and pore pressures in analysis of concrete dams, in ‘Proceedings of the ANCOLD 2013 Annual Conference’.
- Murphy, W. L., Ebeling, R. M. and Anderson, J. M. (2002), Assessment of geology as it pertains to modeling uplift in jointed rock: a basis for inclusion of uncertainty in flow models, Technical report, Engineer Research and development center Vicksburg MS Geotechnical structures lab, USA.
- Nelson, D. M. Sundberg, R. S. D. (1973), ‘Soil mechanics note no. 5: Flow net construction and use’, *Soil Conservation Service, United States Department of Agriculture, Washington, DC*.
- Nilsson, I. and Sandström, L. (2020), Behavior prediction of concrete dams, Master’s thesis, KTH.
- RIDAS (2020), *Kraftföretagens riktlinjer för dammsäkerhet, Energiföretagen Sverige*.
- Royet, P. and Peyras, L. (2013), French guidelines for structural safety of gravity dams in a semi-probabilistic format, in ‘9th ICOLD European Club Symposium’, pp. 8–p.
- Ruggeri, G. (2004), Sliding safety of existing gravity dams-final report, Technical report, ICOLD European Working Group.
- Spross, J., Johansson, F. and Larsson, S. (2014), ‘On the use of pore pressure measurements in safety reassessments of concrete dams founded on rock’, *Georisk: Assessment and Management of Risk for Engineered Systems and Geohazards* **8**(2), 117–128.
- Svensen, D. (2016), Numerical analyses of concrete buttress dams to design dam monitoring, Master’s thesis, KTH.

- USACE (1995), Gravity dam design, Technical Report 1110-2-2200, USA Army Corps of Engineers.
- Westberg, M. (2007), Reliability-based evaluation of concrete dams, PhD thesis, Lund University.
- Woessner, W. W. and Poeter, P. E. (2020), ‘Hydrogeologic properties of earth materials and principles of groundwater flow’, *The Groundwater Project, Guelph, Ontario, Canada* .
- Zang, L. (2006), *Engineering Properties of Rock*, Elsevier, New York.





# Appendix A

## Contour plots

### A.1 Models c - Half water filled drains

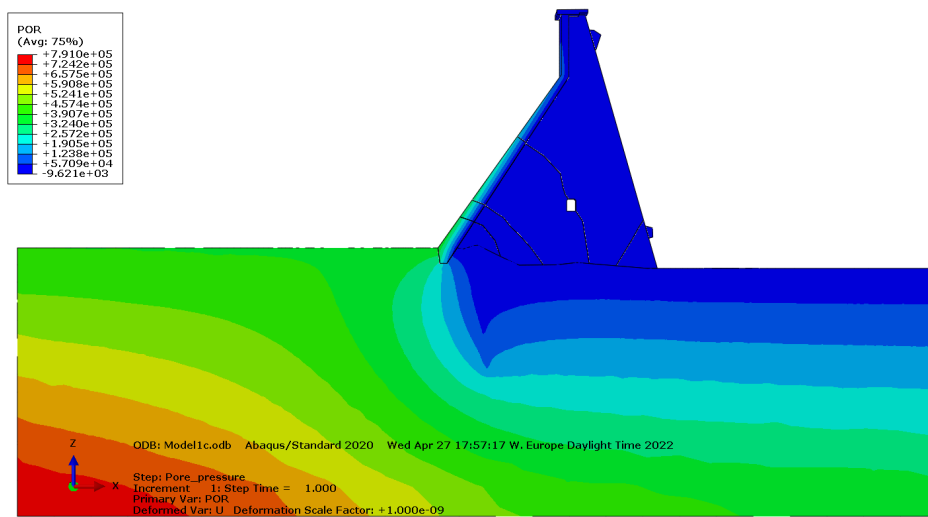


Figure A.1: Distribution of pore pressure in Model 1c with homogeneous rock, drains but no grout curtain

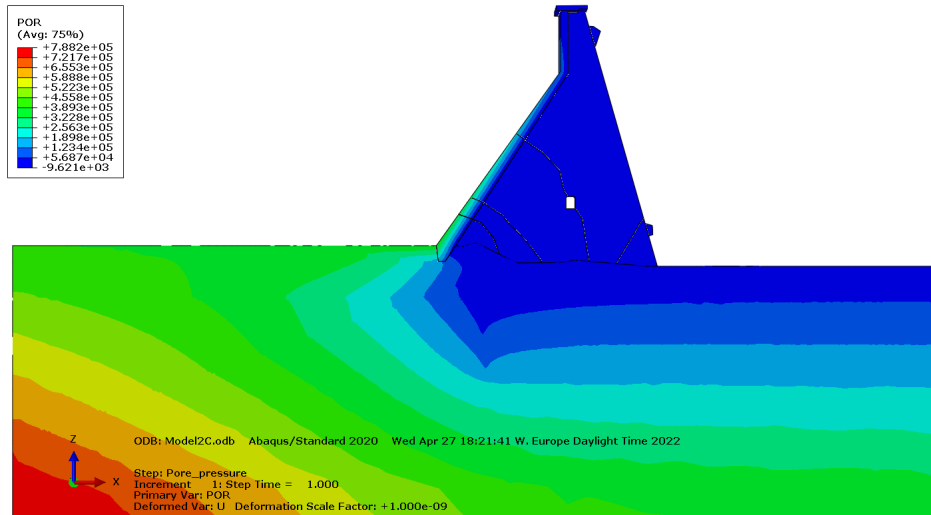


Figure A.2: Distribution of pore pressure in Model 2c with fractured rock, drains but without grout curtain

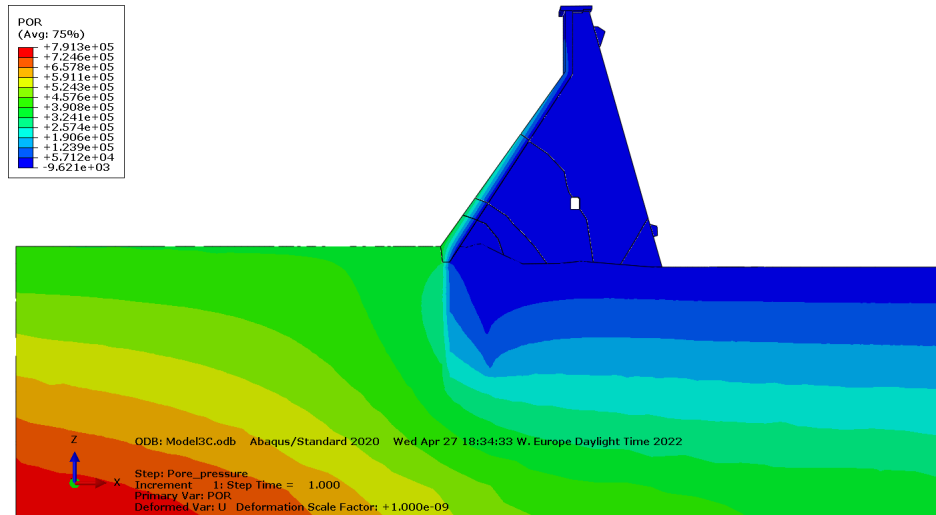


Figure A.3: Distribution of pore pressure in Model 3c with homogeneous rock, drains and with grout curtain

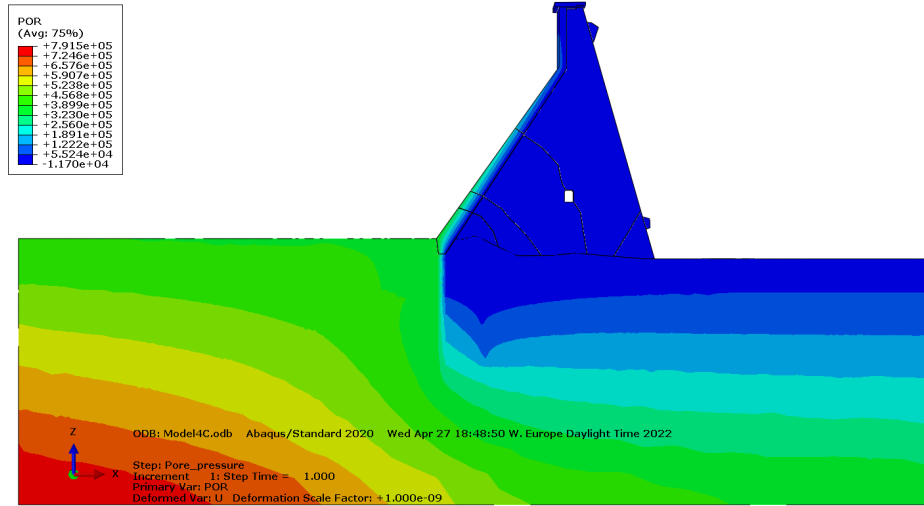


Figure A.4: Distribution of pore pressure in Model 4c with fractured rock, drains and grout curtain

## A.2 Models d - 2/3 water filled drains

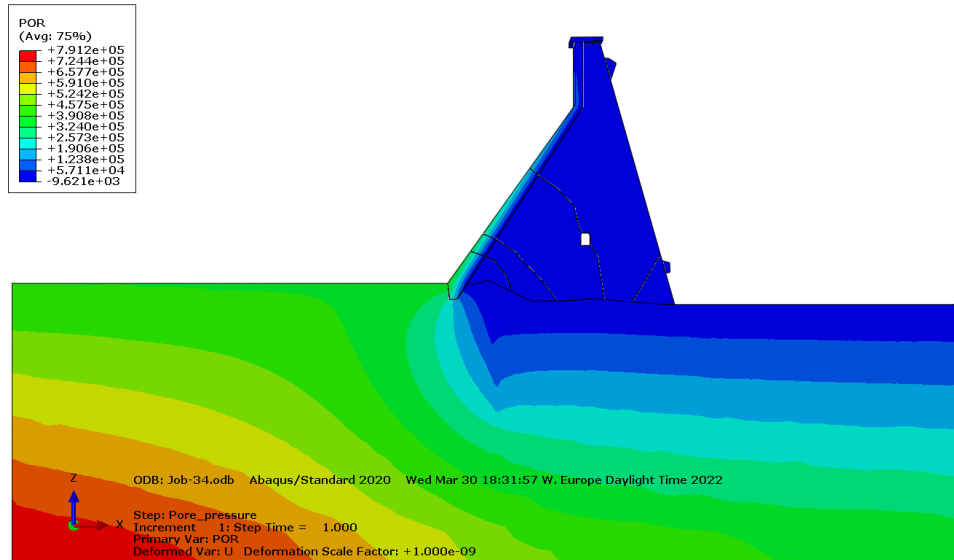


Figure A.5: Distribution of pore pressure in Model 1d with homogeneous rock, drains but no grout curtain

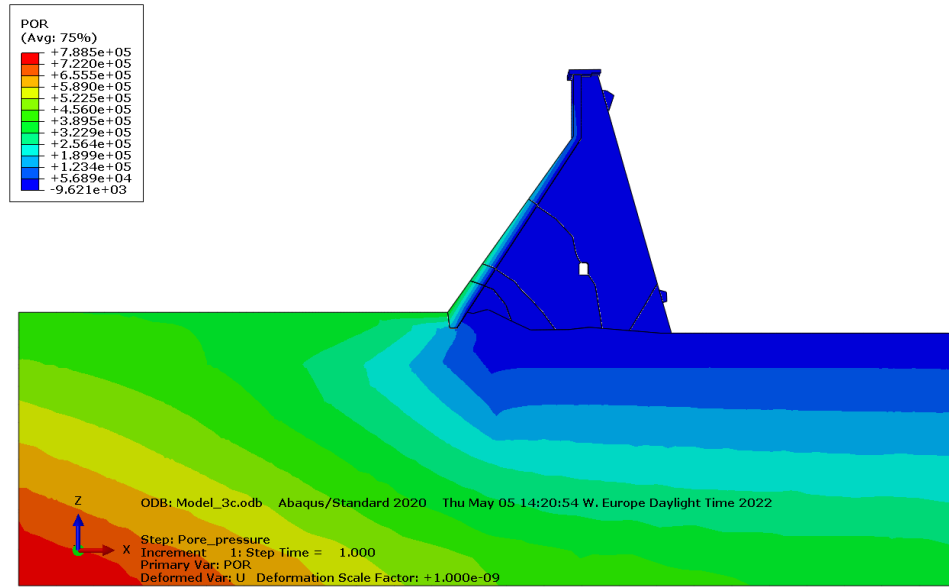


Figure A.6: Distribution of pore pressure in Model 2d with fractured rock, drains but without grout curtain

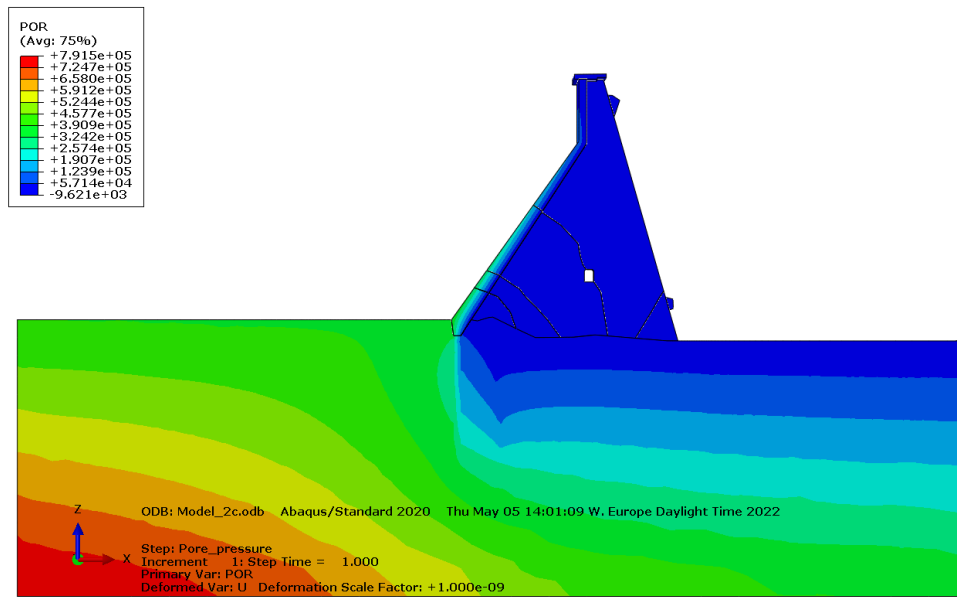


Figure A.7: Distribution of pore pressure in Model 3d with homogeneous rock, drains and with grout curtain

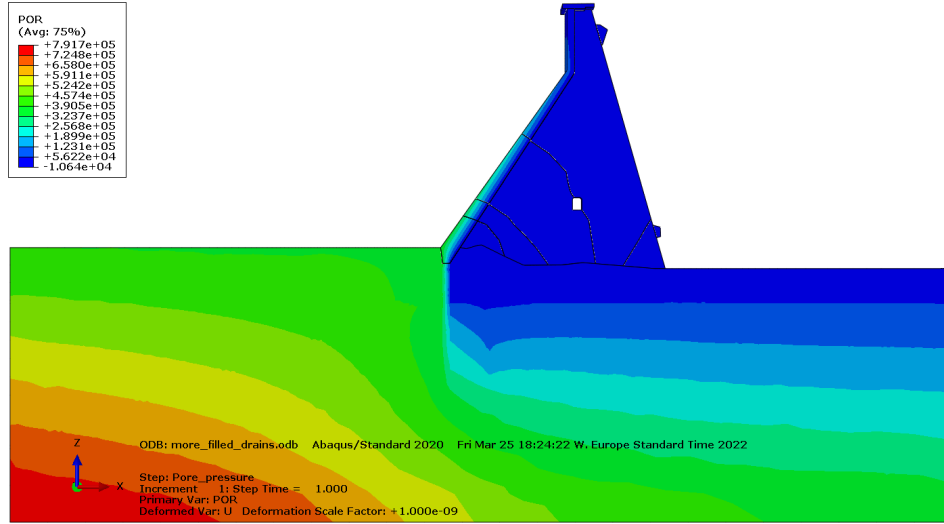


Figure A.8: Distribution of pore pressure in Model 4d with fractured rock, drains and grout curtain

### A.3 Alternative models for the grout curtain

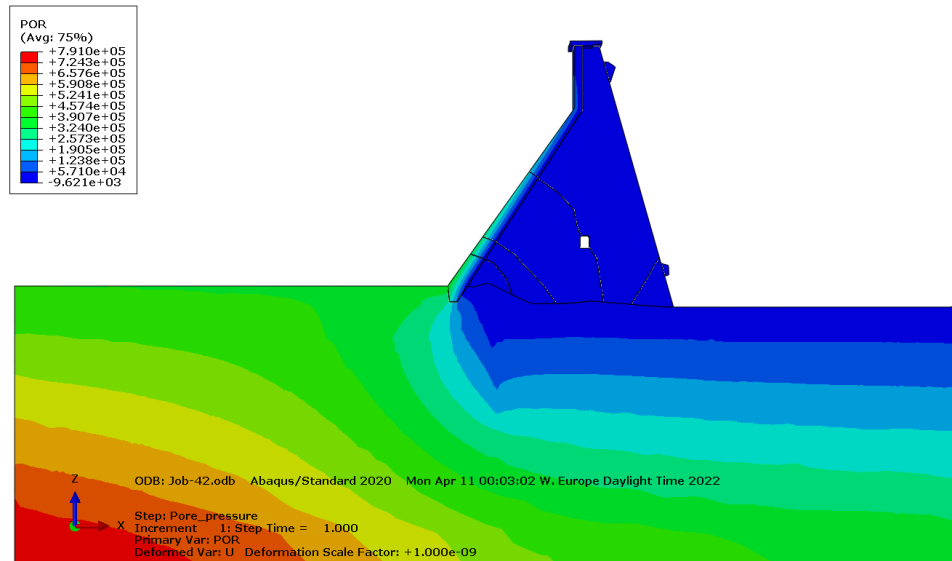


Figure A.9: Distribution of pore pressure in Model 4d Alt.1G with leached long grout curtain

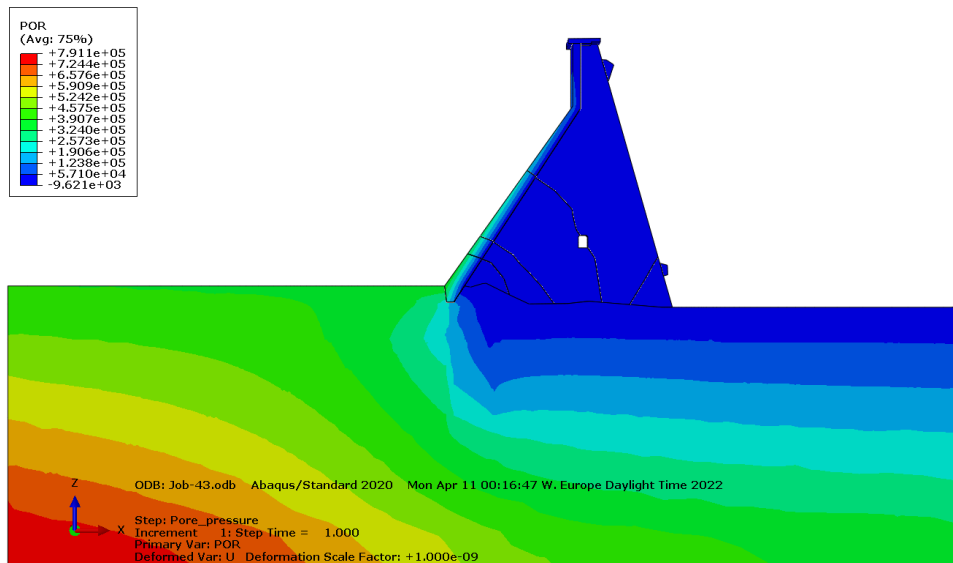


Figure A.10: Distribution of pore pressure in Model 4d Alt.2G with bypassed long grout curtain

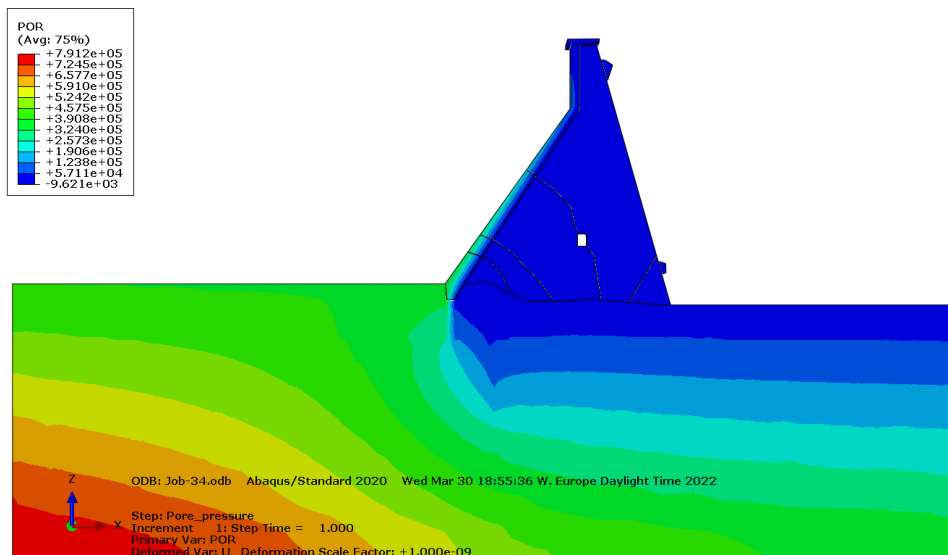


Figure A.11: Distribution of pore pressure in Model 4d Alt.3G with intact short grout curtain

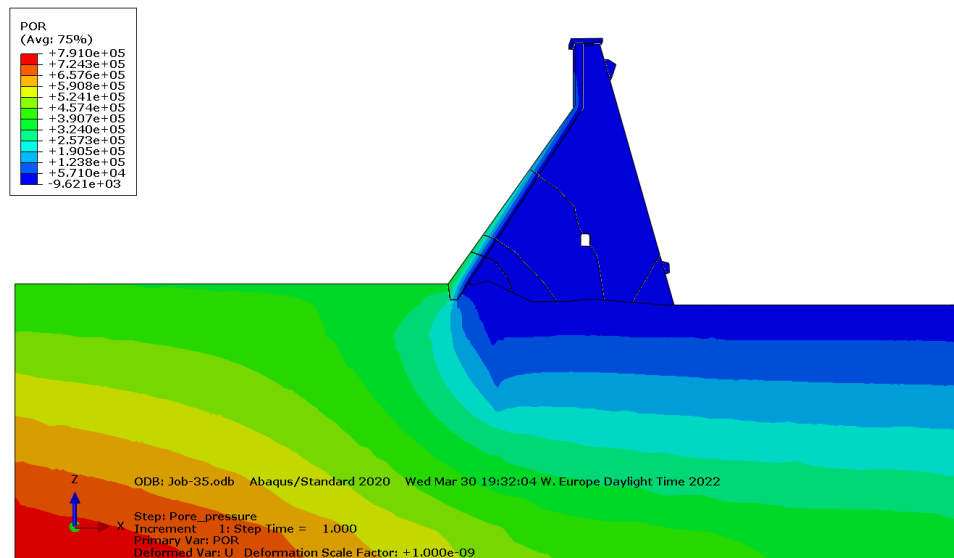


Figure A.12: Distribution of pore pressure in Model 4d Alt.4G with leached short grout curtain

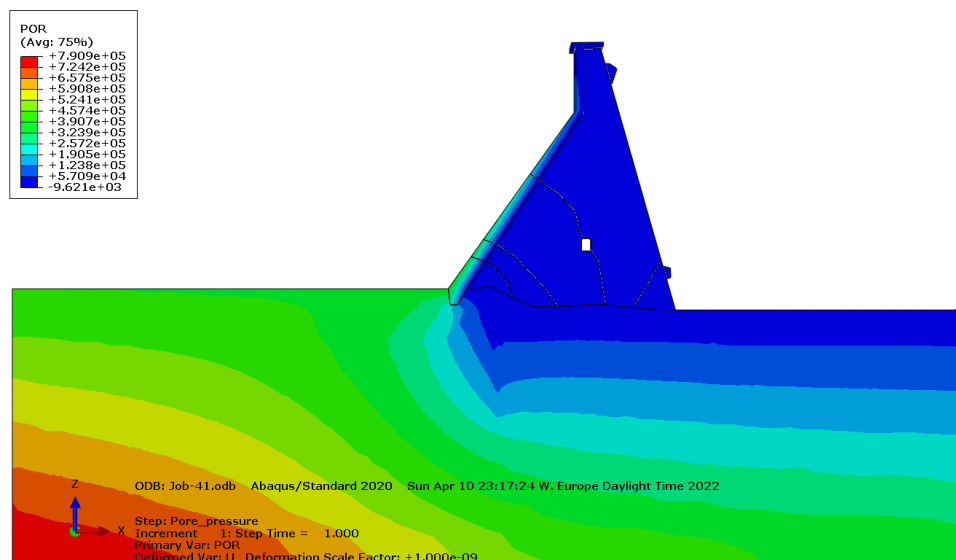


Figure A.13: Distribution of pore pressure in Model 4d Alt.5G with bypassed short grout curtain







TRITA – ABE-MBT-22404  
ISBN: 978-91-8040-306-1